TWO JET PRODUCTION AT CDF

Table of contents

INTRODUCTION

INTRODUCTION

WHY THIS WORK AND WHAT MY CONTRIBUTION WAS

CDF (Collider Detector at Fermilab) is a full-coverage magnetic detector studying $p\bar{p}$ collisions at the $\sqrt{s}$ =1.8 TeV Tevatron Collider. The experiment has collected a handful of demonstration events towards the end 1985, and had its first significant run in spring 1987. Most of this run was operated with a "*buffet trigger*", one stream of which was an inclusive large-E_t trigger. Large E_t (E_t >50 GeV) events at the Tevatron show an increasingly dominant component with two or more hard jets. This thesis consists in an analysis of these jet events. The invariant cross-secton as a function of jet pair mass (M_{jj}) is derived.

An early analisys of the 26 nb^{-1} taken with high E_t trigger had given a hint of a bump in the dijet mass spectrum at a mass value of about 330 GeV. As reported in an internal *CDF* note (CDF-655 April 15th, 1988), the outcome of a rush study of those events was the following: "although we cannot conclude that these features are not fluctuations, we feel that the present data compel us to examine these distributions with the higher statistics that will be available in the next run (1988 run) and that we must put a high priority in obtaining a better understanding of the jet energy resolution".

For these reasons, when I joined *CDF* in April 1988 and while waiting for the much longer run starting October of that year it was decided that for my thesis I would focus my efforts on the study of jet energy and momentum resolution searching for possible corrections to improve them. After the start of the new run later, I was also supposed to look at the new jet data, and regularly produce and update the invariant mass distributions that had raised so much interest in 1987.

The 1987 jet sample was made available for physics analysis after passing a number of calorimeter cleanups and filters intended to eliminate fake jets and reject spurious events. The events were also processed to compute energy release in calorimeter towers. For this thesis, more accurate cleanups were applied to the data, and the processing was extended in order to make more information in each event readily available. The basic calorimetry information was extended to include tracking and missing E_t. Crack chambers and strip chambers banks, which can be used to indicate areas where the calorimeter response is not linear were added.

Next, more offline filtering was applied. Events or runs with known problems were rejected. Tracking information was a must, and all the runs in which for any reason that information was not available were rejected. The aim was to increase the reliability of the sample at the cost of a reduced statistics.

Some compromises had later to be accepted. The strip chamber information has not been used because of disk space limitations. The missing E_t banks were also not used, for the same reason and because of the still incomplete knowledge of the resolution in this variable in high E_t triggers. A very good understanding had been achieved on resolution in missing E_t in minimun bias and large E_t electron events, but it was found to depend on the type of process. In a later stage of the analysis, after having fully exploited tracking, the main handle for our corrections, these informations shall be studied again.

On our jet sample we started careful resolution studies with the purpose of using tracking in order to find a correction to the jet energy measurement and reduce its error. Towards this goal, an important milestone was finding a parameter to monitor the resolution improvement brought in by each correction. A possible [candidate] resolution monitor that was first considered was the decay of the intermediate vector bosons giving two jets in the central calorimeter. The $UA2$ experiment at $CERN$ has shown that these decays produce a detectable eccess of events in the 60-100 GeV range of the two jet invariant mass spectrum. With corrections improving the resolution enough that bump should show up also in our data, and its observed width would be a figure of merit of the corrections. However the statistics collected in 1987 was not enough to detect the signal. Also, the W mass-region was biased by the trigger thresholds in a number of runs taken at the highest luminosities. Finally, in the forthcoming 1988 run at even higher luminosity we expected that most of the $W \rightarrow jj$ events would not be accepted by the jet trigger. We therefore had to give up on this front, and much work was devoted to tune a jet P_t-balancing technique as a sensor of accurate jet energy determination which plays an important role in the present work. Tracking is the instrument for the correction of jet 4-vectors, and the P_t balance of the hard collision products turns out to be an efficient way of testing the effect of the corrections and measuring the jet energy/momentum resolution.

Within the time scale of my thesis (about one year), my primary contribution has been to optimize the sample selection criteria, to tune the corrections, and to analyze the 1987 data in order to get the cross section as a function of dijet mass. During this work, it became clear that the various quality cuts which were being applied were reducing the statistics so much that there was little hope to study the region at $M_{jj} \geq 300$ GeV seriously. The cross section as a function of jet-pair mass was derived as a parameter of interest in its own because of the comparison with QCD and in order to complete the job to all details and be ready for future application with much more statistics. Correcting the jet energy scale to correspond to the hard scattering final state partons, working out the efficiencies of geometrical and analysis cuts, and determining the effect of energy resolution smearing on the underlying jet-E_t distributions are delicate enough jobs. This work was done in collaboration with the *CDF* jet analysis group, and is descrided in the second and conclusive part of this thesis.

The analysis methods developed and tuned in the 1987 data sample shall find an extensive application to new data as soon as they will be available in the proper cleaned-up version. It is only on the basis of a much larger statistics that we can study accurately the dijet mass spectrum above 300 GeV.

1 Theoretical frame

1.1 The Standard Model

The *"Standard Model"* is the theoretical model that is generally adopted to interpret present experimental data on particle interactions at small distances. Despite its tremendous success in the electroweak sector and its excellent performance in the hadron sector, it is not believed to be the ultimate theory. This is so in particular because some of its building blocks have not yet been discovered (the *Higgs*-boson or its equivalent), and more because it still contains to many parameters (e.g. fermion masses).

The fundamental particles of this theory are spin 1/2 fermions (and the corresponding antifermions) divided in two groups, the *quarks* and the *leptons*. Within each of the two groups the fermions are organized in isospin doublets (fig. [1]). The Top quark has not been observed yet, but there is a general confidence that it should exist and be - given the existing experimental limits - very massive.

$$\textbf{Quarks} \quad \begin{pmatrix} u \\ d \end{pmatrix} \begin{pmatrix} s \\ c \end{pmatrix} \begin{pmatrix} b \\ t? \end{pmatrix} \qquad \textbf{Leptons} \quad \begin{pmatrix} e \\ \nu_e \end{pmatrix} \begin{pmatrix} \mu \\ \nu_\mu \end{pmatrix} \begin{pmatrix} \tau \\ \nu_\tau \end{pmatrix}$$

Figure 1: Quark and Lepton families.

The fundamental interactions that are relevant in high energy collisions are :

1) Strong Interaction, mediated by eight massless spin 1 gluons

2) Electromagnetic Interaction, mediated by one massless spin 1 photon

3) Weak Interaction, mediated by massive spin 1 bosons ($W^{\pm}$,Z^0)

Leptons have only weak and electromagnetic interactions, quarks share all of them.

The electromagnetic interaction is described by Quantum Electrodynamics (QED), which is based on a $U(1)$ symmetry. The conserved charge related to the symmetry is the electric charge.

One of the gratest successes of the standard model is the unification of the electromagnetic and weak interactions. The "*Electroweak*" model is based on a non-abelian, spontaneously broken symmetry $SU(2)$ x $U(1)$. The conserved charges associated with the $SU(2)$ and $U(1)$ symmetries are, respectivally, the Weak Isospin T and the Hypercharge Y. As a consequence of the electroweak unification Q, Y, T of quarks and leptons are related quantum numbers : $Q = T + Y/2$. The spontaneous breaking of the symmetry is the reason why the eigenstates of the electroweak interaction hamiltonian are massive vector bosons. Three of them form a weak isospin triplet while the remaning one is a weak isospin singlet.

The two neutral, physically observed states, Z^0 and γ, are the eigenstates of the electroweak hamiltonian after the symmetry breaking. They are a mixture of the two neutral vector fields, B^0 and W^0, as determined by the weak mixing angle θ_w :

$$\begin{pmatrix} Z^0 \\ \gamma \end{pmatrix} = \begin{pmatrix} \cos\theta_w & \sin\theta_w \\ -\sin\theta_w & \cos\theta_w \end{pmatrix} \begin{pmatrix} W^0 \\ B^0 \end{pmatrix}. \tag{1.1}$$

The masses of the weak bosons can be expressed in terms of θ_w in the following way:

$$M^2_{W^\pm} = \frac{\pi\alpha}{2G^2}\frac{1}{\sin^2\theta_w} \tag{1.2}$$

$$M^2_{Z^0} = \frac{2\pi\alpha}{G^2}\frac{1}{\sin^2 2\theta_w}. \tag{1.3}$$

In analogy to QED, *Quantum Chromodynamics* (QCD) has been developed to describe strong interactions of quarks and gluons. QCD is based on a non-abelian exact $SU(3)$ symmetry, which is part of the enlarged $SU(3)$ x $SU(2)$ x $U(1)$ symmetry group of the Standard Model. The conseved charge associated with this exact symmetry is called *Colour*. Each one of the existing types ("*flavours*") of quarks may have three different colour states. The strong interaction conserves the quarks flavours, while weak interactions do not. This translates into the fact that the quark mass eigenstates are not the same as the weak eigenstates. The mixing between them is described by the $Kobayashi - Maskawa$ matrix in such a way that only the charged component of the weak current may induce flavour-changing reactions between quarks.

Quarks cannot be observed as free particles: it is assumed that because of the increase of the strong interaction potential with the relative distance between coloured states, quarks assemble among themselves to form the hadrons, which are colour singlet bound states. Only this colourless states can hit the the experimentalist's detectors; quarks are confined inside hadrons by the colour interactions carried by the gluons.

Quarks and gluons, considered as hadron constituents, are usually called partons.To a first order at small distancies, the coupling constant of strong interaction, α_{strong}, can be expressed as a function of the relative distance, or equivalently of Q^2, the momentum transferred between colour states:

$$\alpha_s(Q^2) = \frac{12\pi}{(33 - 2n_f)\log(\frac{Q^2}{\Lambda^2})}, \tag{1.4}$$

where n_f is the number of existing flavours and Λ is a constant determining the scale of the strong interaction. The value of Λ is not predicted by QCD; it is a free parameter to be derived from the experiment. We should expect it to be of the order of a typical hadronic mass. A value of Λ in the range 100-300 MeV gives a satisfactory agreement with a wide range of data. Λ=200 MeV corresponds to a distance between quarks of about 1 fm. When we are probing quarks at short distances, i.e. at very large Q^2($Q^2 \gg \Lambda^2$), $\alpha_s \rightarrow 0$. Instead, when quarks are far apart, $Q^2 \ll \Lambda^2$, we believe that the strong interaction potential energy would grow to infinity. Thus we can think of Λ as marking the boundary between a world of quasi-free quarks and gluons and the world of pions, protons and so on.

These two opposite behaviours, at very high and at low relative parton energies, are known respectivally as "*asymptotic freedom*" and "*quark confinement*". At the energies of the Fermilab $p\bar{p}$ collider, in many reactions the momentum transfer between partons can be high enough to allow considering them as free particles and their interactions as point-like.

When leaving the interaction region, the struck colored partons must recombine among themselves and with the non interacting "*spectator*" partons to form colorless hadrons. This has to happen with probability one, because of colour confinement. However, given the size of the proton (or equivalently, the value of Λ) this process can take place at a much longer time scale than the quick punch the partons receive in the hard collision. This means that in the hard collision quarks and gluons interact as if they were free, enabling the cross section of the $2 \rightarrow 2$ elementary process to be calculated in perturbative QCD. The subsequent confining interaction does not affect the basic kinematics and topology of the final state partons as determined in the hard collision. However, the fragmentation process of partons into hadrons may induce deviations from the basic topology of the elementary 2 → 2 process . This will be discussed in the following chapters.

The result of color interactions in the final state is to make the outcoming partons "*fragment*" into colorless particles clustered around the direction of the parent parton. Because of their caracteristic form these bunches of hadrons are called *Jets*. The fragmentation process can be described in terms of the longitudinal and transverse momentum variables relative to the jet axis. One normally uses

$$z = \frac{P_{long}}{P_{parton}} \tag{1.5}$$

where P_{long} is the component of the jet prong momentum in the direction of the parton momentum. A fragmentation function $D(z)$ expresses the probability distribution of that variable over a large range. For high momentum partons z approximately represents the momentum fraction taken up by the hadron in the fragmentation process. The average of z may be different for quarks and gluons and may depend on quark masses. Correspondingly, the jet prong multiplicity may be different for different quark masses. Although there are theoretical prejudices on this expectations, there is no conclusive available data to prove a much of it at the present time.

The inclusive M_{jj} mass distribution is predicted by QCD to be a smooth exponential-like function with long tails. There are a number of hypothetical processes, however, that can deform this cross section by adding to the pure QCD component. In particular, if quarks and partons were composite particles at a scale of transverse momentum Λ_c, an excess of rate would develop in the distribution at $M_{jj} \geq \Lambda_c$ (ref [4]).

1.2 Physics at $P\bar{P}$ Colliders

In the Standard Model protons and antiprotons are composite particles, made of three quarks and three antiquarks and the accompanying gluons, as well as of virtual ("*sea*") quarks-antiquarks pairs. This compositness can be parametrized in terms of the momentum fraction x carried by the constituents which is distribuited according to some probability function. These "*Structure Functions*" have been measured in Deep Inelastic Scattering experiments, but little information is available on their behaviour at low x values which is very important for jets at the 100 GeV scale. In addition, at the much larger CDF energies they are expected in QCD to have suffered a very significant Q^2-evolution.

Let's consider the case of charged lepton scattering off a proton target (i.e. $e+p \rightarrow e+X$). The naive description of the collision between the high energy lepton and a parton inside the proton as the interaction of two Dirac free particles, predicts structure functions which depend only on x and not on Q^2, that is the mass of the exchanged virtual photon. Since x is dimensionless, there is no relevant scale of mass or length in the process and the scattering is said to satisfy the so-called "*Scale Invariance*" (Bjorken scaling, ref [7]).

Deep Inelastic lepton scattering data were found to be consistent with the hypothesys of a virtual photon-point fermion scattering but showed the scaling hypotesis to hold only on a limited range of Q^2. Variations of the structure functions could be observed, at fixed x, with increasing Q^2. Moreover, the total fraction of momentum carried by the fermions was measured to be less than the proton momentum, which meant that they are not the only constituents carrying a share of the proton momentum.

Missing proton and scaling invariance violation momentum can be explained in QCD. The fermion constituents, the quarks, are bound to form the nucleon by the exchange of electrically neutral spin 1 particles, the gluons. The gluons themselves are partons and can carry a share of nucleon momentum. However, since they are neutral the momentum fraction carried by them remains undetected by the photon probe in the scattering of charged leptons. On the other hand, scaling violation arises in QCD because of the radiation of gluons in the parton initial state, which grows with Q^2 and red-shifts the parton momentum distribution.

In summary we can group partons in a proton into three separate cathegories: gluons, "valence" quarks and "sea" quarks. The valence quarks are the ones that determine the quantum numbers of physical p and $\bar{p}$. More in general the quantum numbers of all known hadron states can be explained in terms of different combinations of component quarks that for this reason are called valence quarks. This hadron spettroscopy can be done without invoking QCD as long as hadrons are not made to interact, including therefore interactions like DIS. This is called the *Static Quark Model* of hadrons and was developed before QCD. Sea quarks, instead, can be pictured as being radiated by the valence quarks, through gluon splitting, as shown in fig. [2].

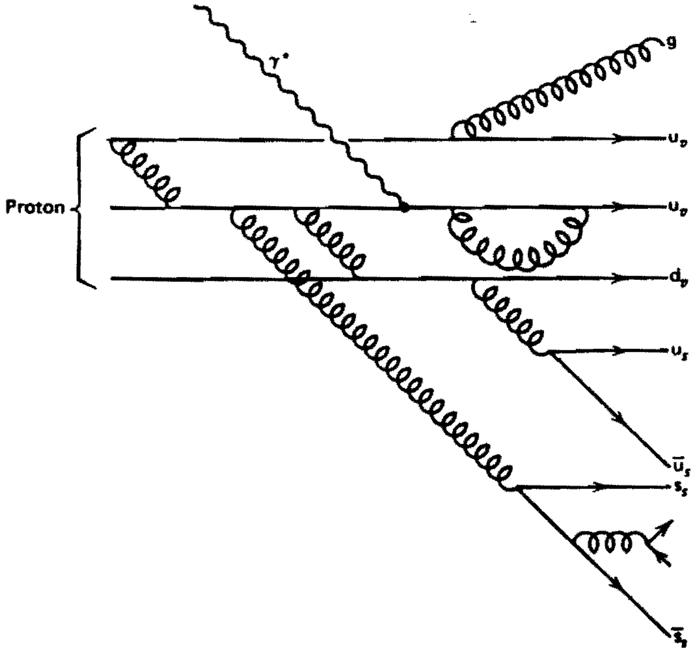

Figure 2: A proton made up of valence quarks, gluons and slow debris consisting of (sea) quark-antiquark pairs.

Accordingly with the above picture, we describe the proton (the antiproton) as a three-valence quarks u_v u_v d_v ($\bar{u}_v\bar{u}_v\bar{d}_v$) accompained by many $q\bar{q}$ sea-pairs (u_s $\bar{u}_s$, d_s $\bar{d}_s$, c_s $\bar{c}_s$ ...) and gluons. In *DIS* experiments, structure functions have been measured for valence and sea quarks. For the valence q flavours (u_v and d_v) the two functions could be measured separately, as shown in fig. [3]. At low x values sea quarks dominate the scattering over valence quarks.

In *DIS* the gluon structure function cannot be directly measured, but rather by subtracting the quark contribution to the proton momentum, the fractional momentum carried by the gluons can be evaluated. Fig. [4] shows that this fraction amounts to about 0.5 and decreases with Q^2 consistently with *QCD* predictions.

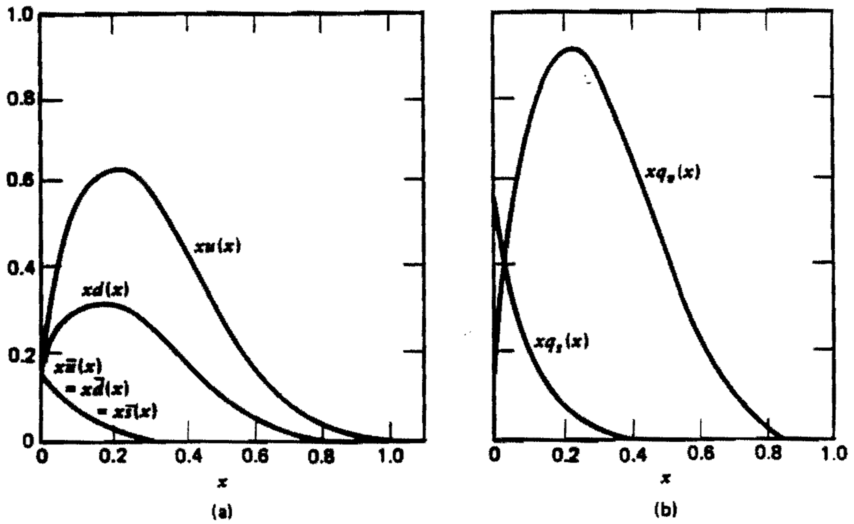

Figure 3: (a)The structure functions of u and d quarks extracted from an analysis of deep inelastic scattering data. (b)The total valence and sea quark contributions to the structure function of the proton.

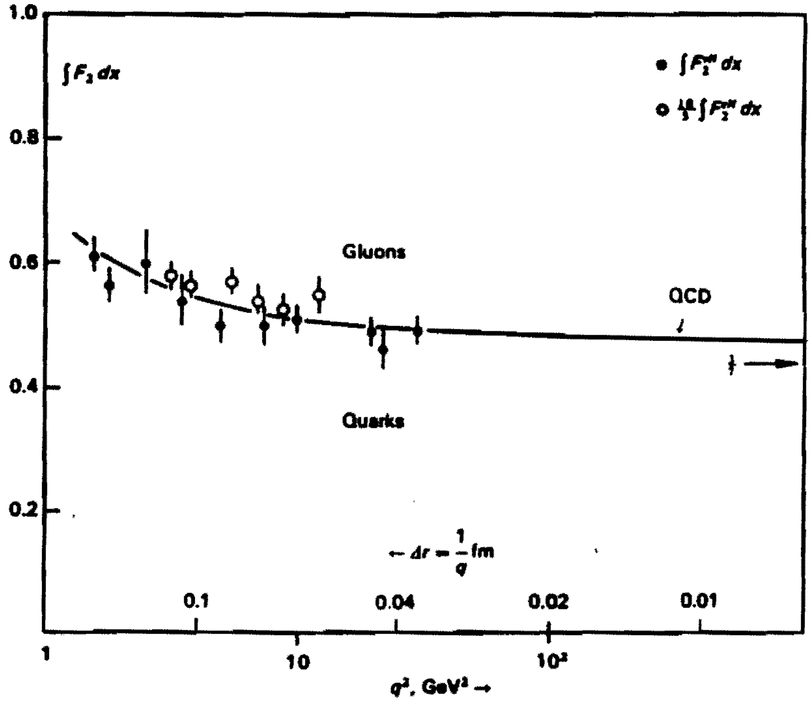

Figure 4: The integral of 1 - $F_2(x, q^2)$ from $x = 0$ to $x = 1$ is a measure of the total momentum fraction carried by the gluons.

Because of the high center of mass energy available at CDF ($E_{cms} = 1.8$ TeV), very low values of x can be probed with hard (large Q^2) interactions. At this energy all fundamental interactions give detectable effects:

- *Weak* : because of the high value of E_{cms} the q and $\bar{q}$ weak coupling to a Z^0 or $W^{\pm}$ gives rise to a detectable W/Z production rate(fig. [5]). The W production cross section is $\simeq$18 nb.

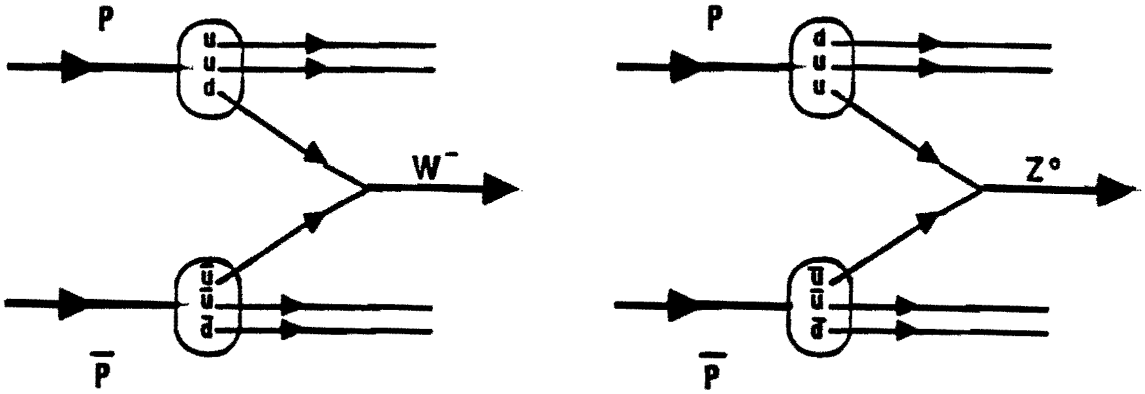

Figure 5: Production of Intermediate Vector Bosons in $p\bar{p}$ collisions.

- *Electromagnetic* : a q and $\bar{q}$ can also annihilate into a virtual photon giving two charged leptons. This process is called "$Drell - Yan$" (fig. [6]), fron the Authors who pointed out this interaction first (ref [5]).

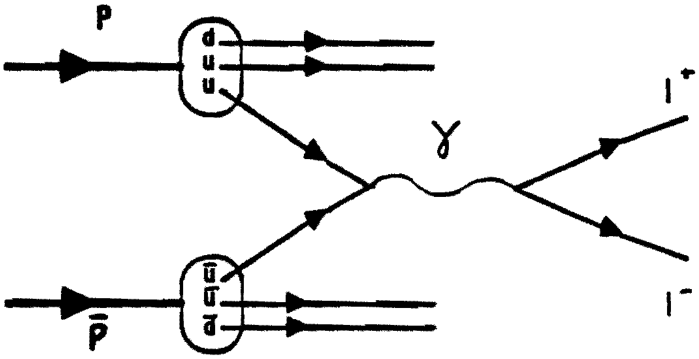

Figure 6: $q\bar{q}$ electromagnetic interaction a' la Drell-Yan.

- *Strong* : these have the highest rate even at large Q^2 and involve all p and $\bar{p}$ contituents q, $\bar{q}$ and gluons.

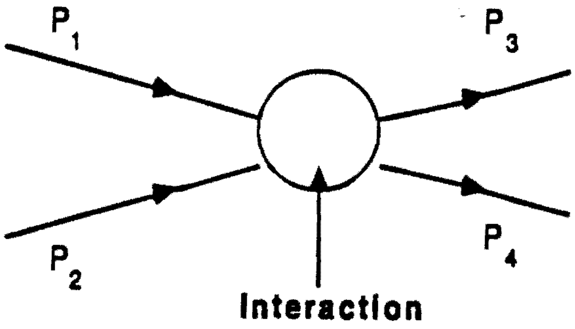

Figure 7: The 4-momenta of the incoming and outgoing partons

The hard 2 → 2 elementary processes in $p\bar{p}$ collisions (see fig. [7]) can be described in terms of the three invariant (Mandelstam) variables :

$$\hat{s} = (p_1 + p_2)^2 \tag{1.6}$$

$$\hat{t} = (p_1 - p_3)^2 \tag{1.7}$$

$$\hat{u} = (p_1 - p_4)^2 \tag{1.8}$$

where p_i (i=1,..4) are the momenta of the incoming and outgoing partons, $\sqrt{\hat{s}}$ is the parton CME, $\hat{t}$ and $\hat{u}$ are the square of the 4-momentum transferred from the initial parton 1 to the final partons 3 and 4. A fairly accurate parametrization of the differential cross section is

$$\frac{d\sigma}{d\hat{t}} = \frac{\alpha_s^2 Q^2 |M|^2}{\hat{s}^2} \tag{1.9}$$

where $|M|$ is the matrix element between inital and final states. Between quarks and gluons there are several possible first order in α_s reactions which are listed in Table 1. The last column of the Table contains the cross section at 90° scattering angle in the CMS. Notice that the cross sections involving gluons are in general larger than those involving only quarks, gg being largest. If gluons and quarks had the same momentum distribution inside the nucleons, gluon interactions would be the dominating QCD process. Gluon structure functions, however, fall to zero for high values of x much more steeply than quark structure functions do. For this reason gluon interactions are predominant at low x values, while at high x values quark interactions become the dominating QCD process.

Elementary process	Matrix element $\|M\|^2$	Value at q^*=90°
$\bar{q}q \to \bar{q}q$	$\frac{4}{9}\left[\frac{t^2+u^2}{s^2}+\frac{s^2+u^2}{t^2}-\frac{2u^2}{3st}\right]$	2.57
$\bar{q}q \to gg$	$\frac{8}{3}(t^2+u^2)\left[\frac{1}{t^2}-\frac{4}{9su}\right]$	1.04
$\bar{q}q \to \bar{Q}Q$	$\frac{4}{9}\ \frac{t^2+u^2}{s^2}$	0.22
$gg \to \bar{q}q$	$\frac{4}{9}(t^2+u^2)\left[\frac{1}{t^2}-\frac{4}{9su}\right]$	0.16
$gq \to gq$	$(s^2+u^2)\left[\frac{1}{t^2}-\frac{4}{9su}\right]$	6.12
$gg \to gg$	$\frac{9}{2}\left[3-\frac{tu}{s^2}-\frac{st}{u^2}-\frac{us}{t^2}\right]$	30.4

Table 1: Matrix element expressed in terms of the Mandelstam variables. q^* is the center of mass scattering angle.

The momentum fractions of the colliding partons x_1,x_2 are related to the *CMS* energy $\sqrt{s}$ and the parton *CMS* energy $\sqrt{\hat{s}}$ by the relation:

$$\hat{s} = x_1 x_2 s \tag{1.10}$$

At the Tevatron ($\sqrt{s}$ = 1.8 TeV), the hardest is the scattering (that is the highest is $\hat{s}$) the highest x_i's are probed by the collisions. On the other hand, one sees that processes with a fixed value of $\hat{s}$ are intitiated at the Tevatron by partons with lower x_i's than at previous lower energy colliders.

As described by Table 1, strong interations can produce heavy quarks, like charm, bottom (and hopefully top) with a detectable rate at the Fermilab Collider. Heavy quark flavours can either fragment into jets or undergo semileptonic decays like

$$C \rightarrow \mu^{+} + \nu_{\mu} + S \tag{1.11}$$

$$B \rightarrow e^{-} + \bar{\nu}_{e} + C. \tag{1.12}$$

The leptonic channel is considered to be the best suited to study heavy flavours, because tagging leptons in the final state is more selective than looking at jets.

In summary, the dynamics of $p\bar{p}$ collisions can be ideally conceived as three subsequent steps (see fig. [8]).

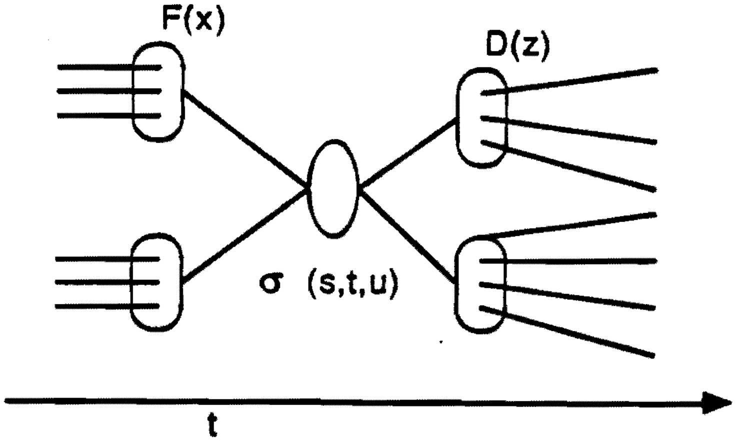

Figure 8: The collision process is decribed by the structure functions, $F(x)$, the elementary scattering cross section, $\hat{\sigma}(\hat{s},\hat{t},\hat{u})$, and the fragmentation function $D(z)$.

The incoming parton flux is characterized by the structure function expressed in terms of x. A scattering process takes place, described by the elementary cross-sections $\hat{\sigma}$ which are known at the first order as analytic functions of the Mandelstam variables (s,t,u); finally the outgoing partons fragment according to probability distributions $D(z)$ which depend primarily on the fractional longitudinal momentum z. Since fragmentation is a soft (small Q^2) process, it cannot be predicted in perturbative QCD and must be determined empirically. One expects, however, a slow dependence of $D(z)$ on Q^2.

Together with standard QCD processes new physics can be probed with jet physics at CDF, because the high CMS energy allows the exploration of new energy regions. Parton compositness (ref [4]), for exemple, would be signalled by an increased rate over QCD expectations at the highest jet-jet masses.

2 The Experiment

2.1 The Fermilab $P\bar{P}$ Collider

The main features of colliders is that high values of $\sqrt{s}$ are reached: two beams of energy E_b provide $\sqrt{s} = 2\ E_b$, which compares to $\sqrt{s} = \sqrt{2m_t E_b}$ for the scattering of the same beam on a fixed target of mass m_t. The Fermilab Tevatron $p\ \bar{p}$ collider is operated with 900 GeV beams, and thus at a center of mass energies of 1800 GeV (to be compared to 40 GeV for collisions of a 900 GeV beam on a fixed proton target).

Existing colliders exploit $p\bar{p}$, e^+e^-, and soon ep beams. In the traditional circular e^+e^- colliders relatively lower energies can be reached in practice because of the energy lost by the circulating beams in the machine rings due to sinchrotron radiation. This is not a limiting factor for a hadron collider because for the same momentum and orbit radius protons radiate about 10^{13} times less than electrons (sinchrotron radiation is in proportion of $\frac{1}{M^4}$). This very practical but extremely important fact makes the hadron colliders a very competitive, first class tool in the exploration of proton structure and interaction.

On the other hand, e^+e^- collisions produce a much cleaner environment than $p\ \bar{p}$. For example, at existing machines $e^+e^- \rightarrow q\bar{q}$ contains only two jets (and on occasions a third one) in the final state, and nothing else. The equivalent reaction $p\bar{p} \rightarrow jjX$ contains in the final state also the (in general numerous) fragments X of the spectator partons. This makes the reconstruction of the event more difficult in our case. A good deal of the higher CMS energy of the proton collider is lost in generating this state X, which to a first approximation just causes confusion and problems.

Because of the above mentioned compositness of the primary protons there is another feature of $p\bar{p}$ interaction which shows up as a disadvantage. The center of mass energy for the elementary collisions is appreciably smaller than the accelerator energy. Parton interactions are therefore probed at much lower Q^2 then nominally possible. Even so, the largest available Q^2's are reached only in hadron collisions. Now and in the future their energy is made so high that the small ratio $\frac{\hat{s}}{S}$ will be largely compensated. A schematic drowing of the Fermilab collider is shown in figure [9].

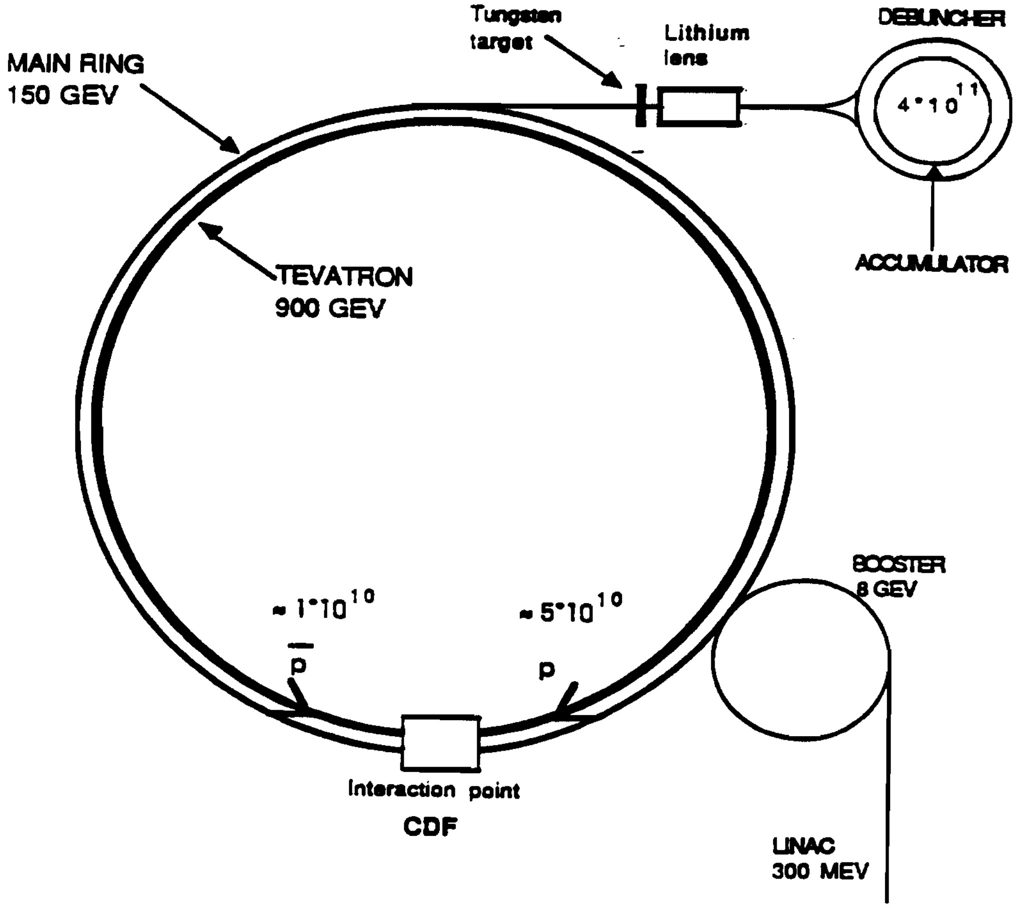

Figure 9: The Fermilab synchroton. The Tevatron is located 60 cm above the Main Ring.

By means of a Cockroft-Walton electrostatic accelerator protons are preaccelerated to about 2 MeV and led to a 200 MeV 150 m long linear accelerator (LINAC). They are then injected in a 70 m radius circular accelerator (booster), where they reach 8 GeV. Next, they enter a conventional synchrotron, the Main Ring . This, since the installation of the Tevatron, is used as a 150 GeV injector for the Tevatron. This 26 km long synchrotron which is the last step of the chain, uses superconducting magnets which provide high enough magnetic field to allow the beam to reach energies of 900 GeV in a ring of the same radius as the Main Ring. In the collider mode of oparation of the Tevatron, about 5 10^{10} protons per bunch and several bunches (3 in 1987, 6 in 1988) are accelerated for collisions with an equal number of antiproton bunches.

Antiprotons are produced by protons extracted from the Main Ring at 120 GeV on a tungsten target. About 7 10^7 pbar's per bunch are collected at 8 GeV through a lithium lense, and enter the Antiproton Debuncher-Accumulator complex. Each shot enters first the Debuncher, where its multi-bunch time structure is much reduced and their momentum spread correspondingly monochromatized, and is subsequently transferred to the Accumulator. Stochastic cooling is intensively applied to reduce the phases space volume required by each bunch. Successive bunches can then be accumulated with (at present) a stacking rate 1-2 10^{10} $\bar{p}$/hour.

The total number of antiprotons per bunch was about 10^{10} in the 87 run. The time preparation for a "*shot*" (the injection of the antiprotons into the Main Ring) was about three hours in 1987 and six hours in 1988/1989. After injection, antiprotons are accelerated to 150 GeV in the Main Ring, nad then transferred to the Tevatron to join the previously stored proton bunches. Finally protons and antiprotons are accelerated together in opposite direction. Figure [10] summarizes all these steps.

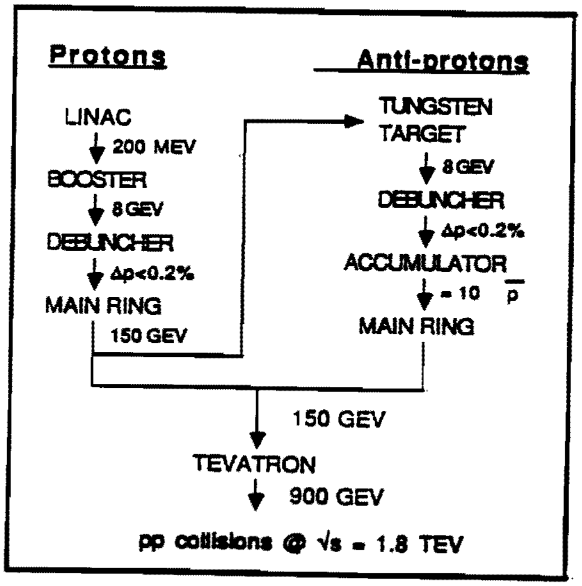

Figure 10: $p\bar{p}$ path to the collision

The original design goal of the Tevatron collider was to have six bunches of protons and antiprotons (a beam crossing every 3.5 microseconds), and a luminosity at injection of $10^{30} cm^{-2} sec^{-1}$. This was achieved during the first week of September 88 and largely surpassed during the run. Present Tevatron Collider plans anticipate a luminosity of 6 10^{30} in 1991 and 5 10^{31} (with 22 or 44 bunches) in 1995. During the 1987 run the collider was operated in a three bunches mode and the peak luminosity was 4 $10^{29} cm^{-2} sec^{-1}$.

2.2 The CDF Detector

The Collider Detector at Fermilab is a full coverage 5K tons magnetic detector built to study hard interactions at the energy of $\sqrt{s} \simeq 2$ TeV. Addition of small angle detectors made diffractive and elastic studies also possible. A general view is given in figures [11] and [12].

The basic goal of CDF is to identify leptons and jets and measure their energy and momentum over as large a fraction of the solid angle as possible. To accomplish this, the intaraction region is surrounded with tracking chambers, samplings calorimeters and, in some regions, muon detectors.

The CDF electromagnetic and hadron calorimetry consists of four different detector components: the central and wall hadron calorimeters, where scintillators are used as active elements, and the end-plugs and forwards calorimeters, using proportional chambers. These calorimeters are left-right and azimuthally symmetric and provide full azimuthal coverage. The scintillators calorimetry covers the polar angle $30° \leq \theta \leq 150°$, while gas calorimetry covers $2° \leq \theta \leq 30°$, $150° \leq \theta \leq 178°$.

An important feature of the CDF calorimetry is its fine-grained structure. Overall, the calorimeters are segmented into about five thousand projective "*towers*" or solid angle elements pointing to the nominal vertex of interactions. Since the properties of average hadron collisions are approximately uniform in rapidity as well as azimuthal angle, the whole system has been organized in an approximately cilindrically symmetric layout of towers, with roughly constant pseudorapidity ($\eta = -ln(tg\frac{\theta}{2})$) and azimuthal ($\phi$) dimensions throughout the detectors. Each tower consists of a front (elctromagnetic) compartment and of a rear (hadronic) compartment. At $|\theta| < 30°$ there are up to four e.m. towers per hadron tower.

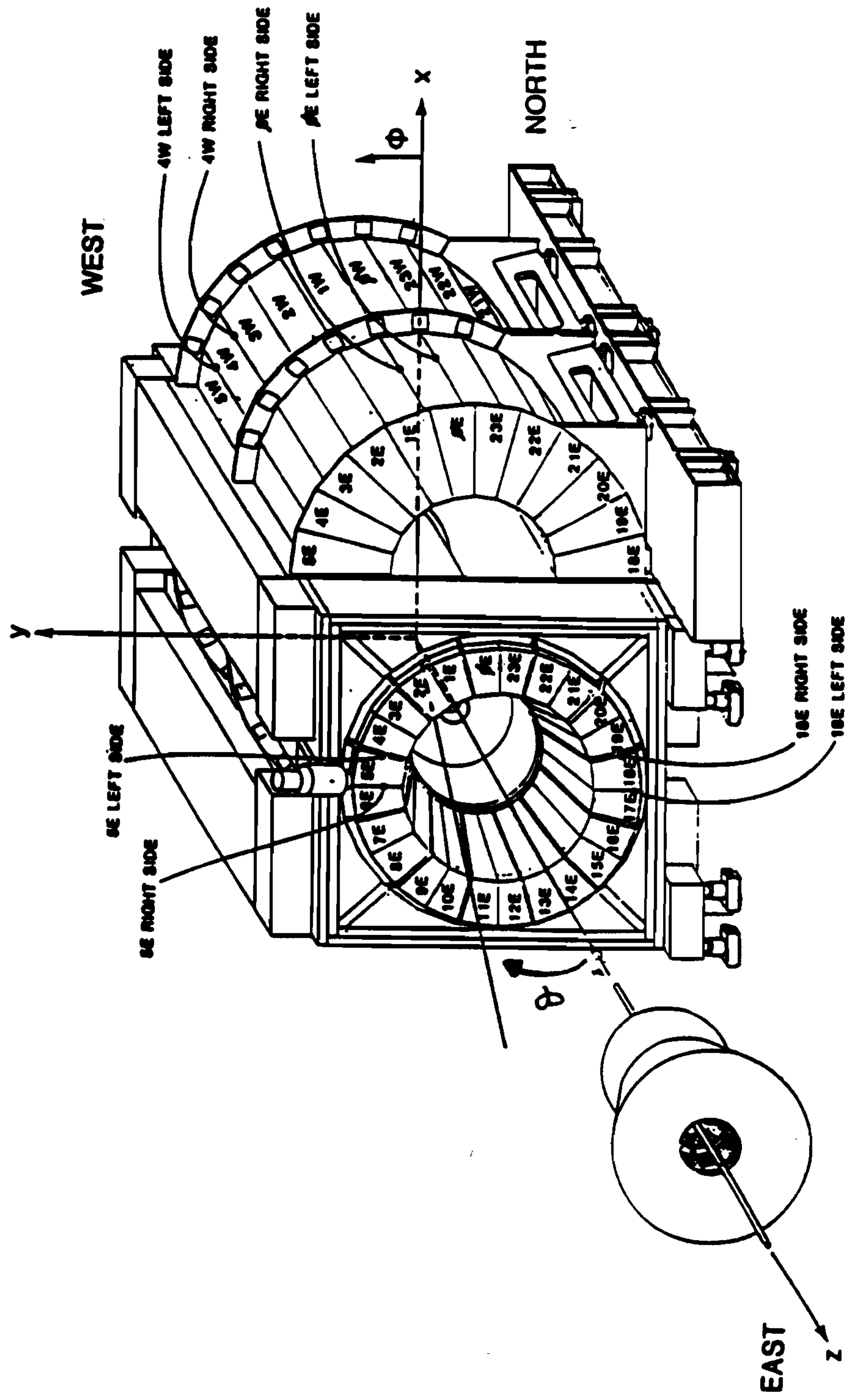

Figure 11: Perspective view of CDF detector.

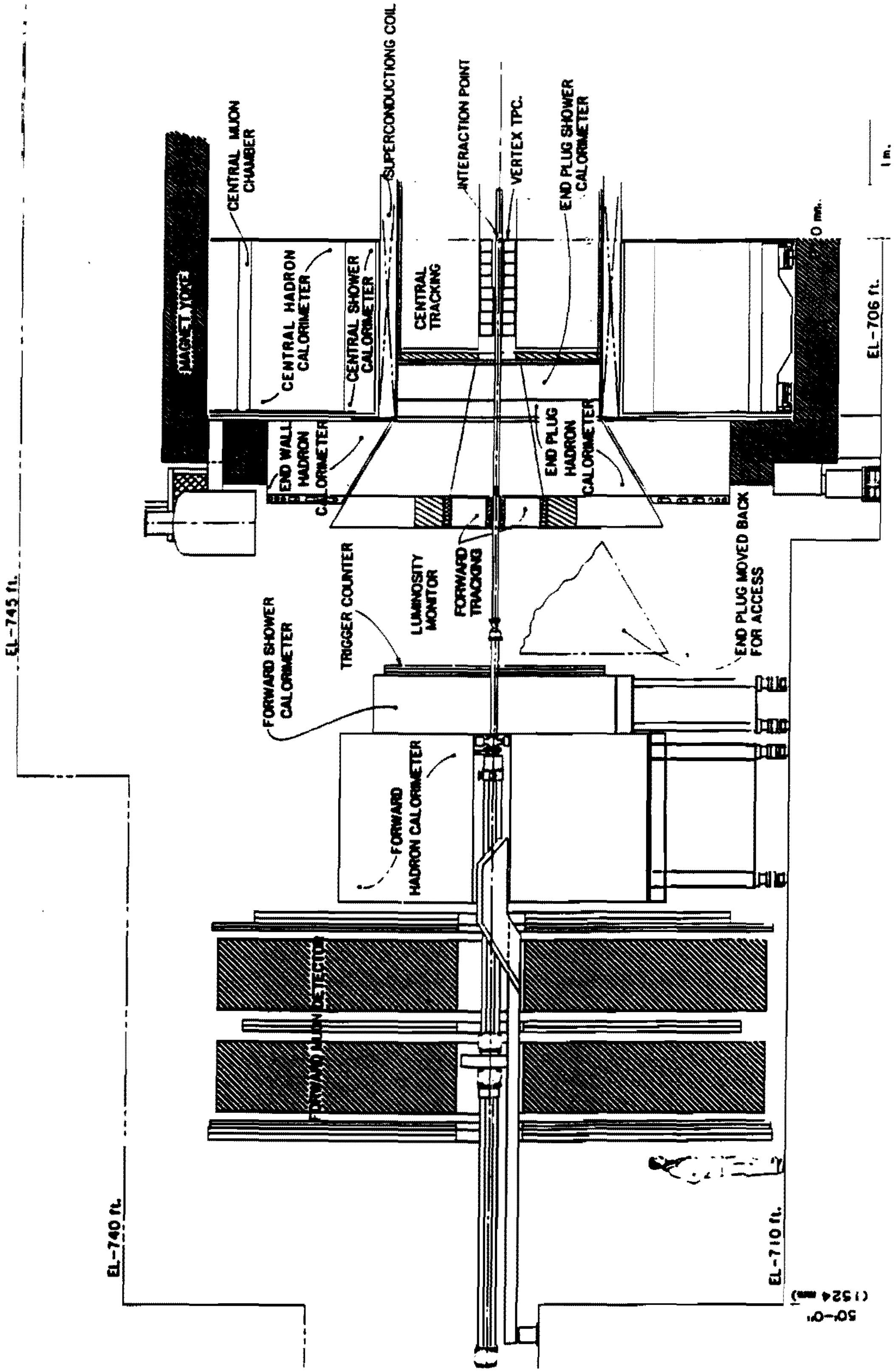

Figure 12: Cross section through a vertical plane of one half of CDF detector. The detector is symmetric about the midplane and around the beam axis.

Charged particle momenta are analized by their bending in a 1.5 Tesla solenoidal magnetic field generated by a superconducting coil, which is 3 m in diameter, 5 m in length and is located around the intersection with its axis parallel to the beams.

In *CDF* there are four separate tracking systems. Immediately outside the beam pipe, eight small vertex time projection chambers (the VTPC system) track charged particles in the range $-3.5 < \eta < 3.5$ (at angles grater than 3.5° from the beam line) and give good pointing in the theta direction. This measure is used to reconstruct an accurate (± 3 cm) vertex position of the event. Multiple interactions in the same crossing are in general easily distinguished.

The central tracking chamber (CTC) is a large cylindrical drift chamber filling most of the solenoid magnet volume and providing excellent spatial and momentum resolution (bending in r-ϕ). A three-layer cylindrical array of drift tubes (CDT) with high resolution charge division surrounding the CTC just inside the solenoid gives a correlated r-ϕ-z measurement. Both the CTC and CDT have full coverage in the pseudorapidity range $|\eta| > 1.0$.

The forward tracking system (FTC) was designed to allow reconstruction of tracks exiting the 10° holes of the end plugs and striking the forward calorimetry ($|\eta| > 2.2$). Tracking in this area of large particle density is difficult, and the system is still under development.

Muon detection is performed with drift chambers in the range $50° < \theta < 140°$ (Central Muon System, CMU) and $4° < \theta < 16°$, $16° < \theta < 176°$ (Forward Muon System, FMU) .

VTPC, CTC, CDT and CMU are arranged concentric to the beam pipe with outer radii going from 30 cm (VTPC) to 135 cm (CTC), 140 cm (CDT) and 350 cm (CMU).

The part of *CDF* that is more relevant for the purpose of this thesis is the combined system of the central tracking chamber and the scintillator calorimetry. This component of *CDF* calorimetry is split into the Central Electromagnetic (CEM), Central Hadron (CHA) and the Wall Hadron (WHA) Calorimeters.

The hadronic compartments (CHA and WHA) cover the polar angle range $30° < \theta < 150°$ or, equivalently, the pseudorapidity range $-1.3° < \eta < 1.3°$, while the CEM efficently covers only $|\eta| < 1.1$. In the remaining 0.2 pseudorapidity units the electromagnetic coverage is provided by the two outer η-rings of the neighbouring gas calorimeter (the end plug or PEM). The side view of the detector, given in fig. [13], shows the relative positions of the various detector components.

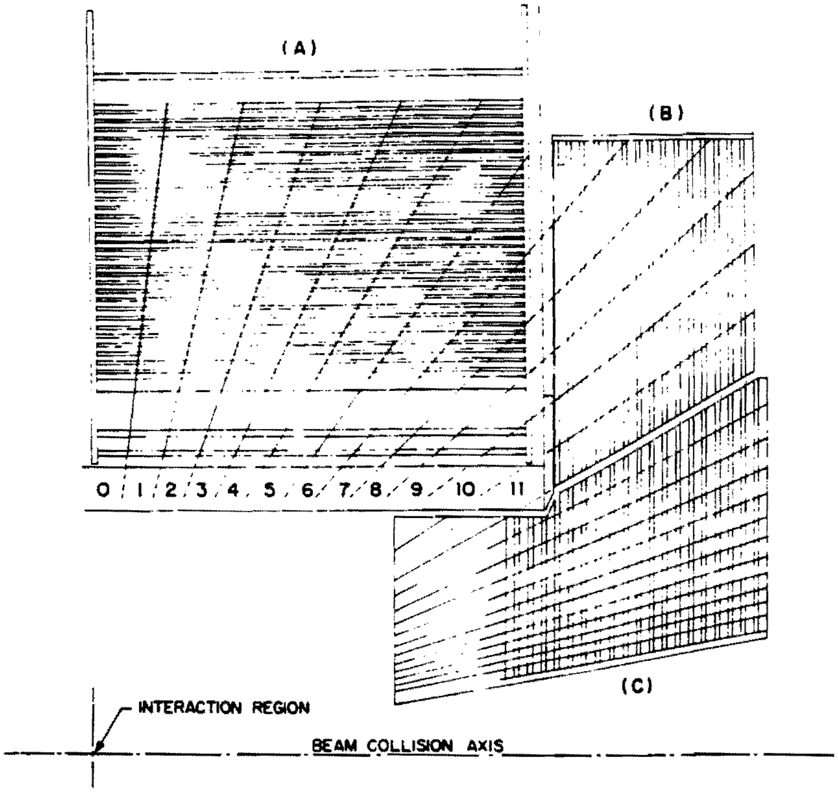

Figure 13: Quadrant of the calorimeter. A, B, C show the central, endwall and plug calorimeter respectivelly

The overlap in the outer central towers of two kinds of electromagnetic calorimeters with different performances causes some complications in the analysis of the jet data. This will be addressed in the Chapter on tracking corrections. From now on we will refer to the scintillator calorimeters (CHA + WHA) with the generic name of "*central calorimeter*".

We shall now illustrate a number of details of the central detector that are relevant for a better understanding of the informations that they provide, of which use can be made in the data analysis.

2.3 The Central Calorimeter

The large angle calorimeter is divided into two halves at the plane Z=0. Each of them is split into 24 central modules, called Wedges, (CEM and CHA) and in 24 wall hadron modules (WHA), each of them subtending approximately 15 degrees of azimuthal angle ϕ. Each calorimeter module is divided into towers projecting to the nominal point of beam-beam crossing. Each tower covers approximately 0.11 unit in η and 15° in ϕ. This segmentation is a compromise between the request of a high granularity and the necessity of limiting the number of splittings ("*cracks*"), that introduce dead regions between the towers. In particular, the average segmentation was designed fine enough that jets would spread over several towers.

For each 15° wide azimuthal slice there are 15 hadronic towers in total, six of which are totally in the central calorimeter (CHA), three totally in the endwall (WHA) and three are shared, i.e. cover the same intervals of polar angles. The η range subtended by the hadron towers is $-1.32 < \eta < 1.32$. At $\eta = 0$ there is a separation between the wedges (the so called 90° crack). The effect of this crack on the jet data will be object of further analysis in the Chapter on calorimeter resolution.

The hadronic compartment consists of steel plates 2.5 cm thick in the central and 5.0 cm thick in the endwall, interleaved with 1 cm thick scintillator planes (32 in the CHA and 15 in the WHA). The total depth in the central is 4.7 interaction lengths at $\eta = 0$ (plus 1 interacton length due to the front CEM). The calorimeter depth in WHA is 4.5 λ in the direction parallel to the beams. In each tower the light emitted in the scintillator plates is collected by wavelength shifter rods on the two θ-sides, and then read by the photomultipliers by means of multilayer light pipes on the azimuthal sides. There are two light pipe fingers reading out each plate, one on the left and one on the right. The same side fingers from different layers are joint together to the photomultiplier to integrate half (in average) of the signal from an entire tower. This system allows the measurement of the ϕ centroid of the hadronic shower by compairing the pulse hight in the left and right p.m.'s (because of the light attenuation in the WLS, fig. [14]). A TDC on the last dynode of the photomultipliers provides a prompt information on the arrival time of signals which is used to reject events not correlated with bunch crossing.

In the offline analysis the information from towers with $\frac{L}{R}$ either too high or too small is rejected because (as test beam calibrations have shown) it is usually due to Cherenkov light emission by particles hitting the light guides ("*hot spots*").

For incident $e^{\pm}$, test beam studies have shown that this background is completely removed when the space between two adjacent modules (the so called ϕ-cracks) is covered by a bar of some radiator material. 10 radiation lengths of U^{238} were used in the 1987 run.

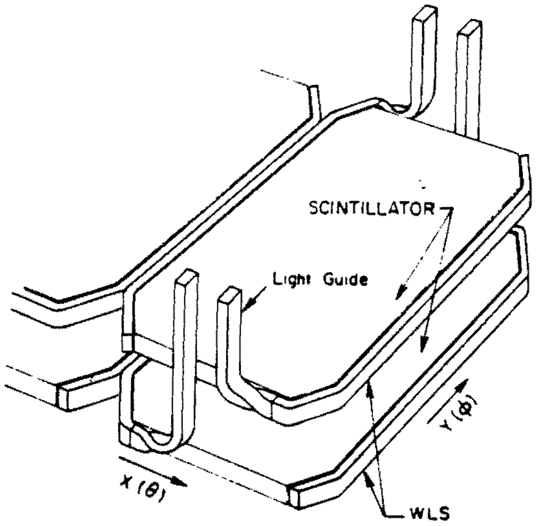

Figure 14: Scintillator and WLS.

Behind these "crack fillers" there are proportional chambers (Crack Chambers, CCR), whose energy resolution for 50 GeV electrons is known from the test beam to be 25 %. At variance with respect to electrons, test beam studies have shown that the charged hadrons many times do not interact and that in general a widely fluctuating fraction of their energy remains undetected.

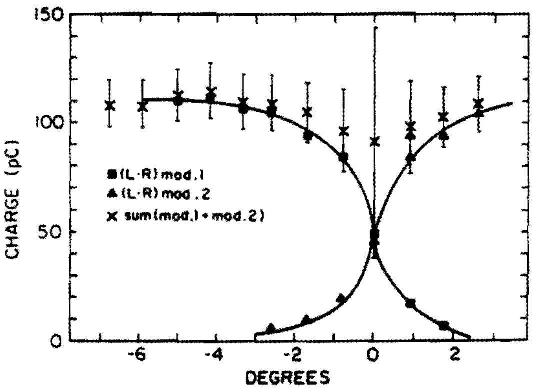

Figure 15: ϕ response to a 50 GeV pion beam sweeping the facing towers of two stacked modules.

Fig. [15] shows the response, averaged over the test beam size (radius $\simeq$ 2 cm), to a ϕ scan at tower center with 50 GeV pions. The response is flat when the beam is well inside the modules. This is the result of a careful equalization of the left-right p.m. gains. On the other hand, the interface region shows a dip and significant degradation of the energy resolution, indicating the presence of dead areas and of large pulse height tails. Most of the non uniformity in the response map of *CDF* large angle hadron calorimeter is due to the presence of the ϕ cracks. An appreciable effect is brought in also by the dead area in the calorimeter split at $\simeq 90^\circ$ polar angle.

Fig. [16] shows the energy dependence of the energy resolution for pions hitting towers 1 and 5 of the central calorimeter (2.5 cm sampling) and tower 10 of the endwall (5 cm sampling), as measured on a test beam. These pions were selected to be M.I.P. in the electromagnetic calorimeter. This figure shows that at 10 GeV $\leq E \leq$ 100 GeV the resolutions are approximate straight lines of increasing slopes according to increasing sampling thickness. As energy increases the fluctuations from leakage from the back of the calorimeter become important: for instance above 50 GeV the resolution of tower 5, which, because of the projective angle, has a coarser sampling by 1.5 but is thicker by the same factor, is better than tower 1. In average we find

$$\frac{\sigma_E}{E} \simeq \frac{0.7}{\sqrt{E}} \tag{2.1}$$

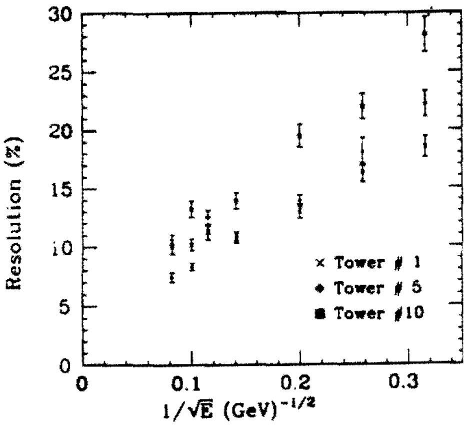

Figure 16: Energy resolution as a function of pion energy for towers 1,5,10.

For energies lower than 10 GeV no test beam data are available. The calorimeter response has been monitored using isolated tracks in minimum bias events. In average over angles of incidence and over all calorimeter area, the response is found to be appreciabily less then linear. The impact of this non linearity on jet energy resolution is very strong. This will be discussed in the Chapter on tracking corrections to jet energies.

The central electromagnetic calorimeter (CEM) is located in front of CHA and is split into towers with the same projective geometry as CHA. It consists of 32 planes of scintillators alternated with about 4 mm thick lead layers, giving a total of 20 radiation lenghts. This ensures a good containement (> .99) for electromagnetic showers of energy up to $\simeq$ 100 GeV.

In the CEM compartment, the light is collected by WLS plates on the two sides of the scintillator sheets which are opposite in azimuth. The ratio of light transmitted to the left-right p.m.'s viewing a CEM tower is related to the ϕ centroid of the shower like in the hadron calorimeter, due to the attuation of the light in the scintillator.

The energy resolution as measured at the test beam is

$$\frac{\sigma_E}{E} = \frac{.14}{\sqrt{E}} \tag{2.2}$$

Additional information on the shower development is given by strip chamber (CES) inserted in the CEM parallel to the scintillators at the depth of shower maximum. These chambers determine the position of the shower centroid by measuring the charge deposited on a net of orthogonal stripes and wires. The resolution is momentum dependent, varying from 3 mm at $P_t = 10$ GeV to 2 mm at $P_t = 50$ GeV.

2.4 The Central Tracking Chamber

The CTC is a 3.2 m long cilindrical drift chamber with 1.35 m outer and 0.3 m inner radius. The function of this tracking system is complementary to the central calorimetry. While calorimetry integrates over particle energies, the CTC efficently measures trasverse momentum and trajectory of charged particles in the region $40^\circ < \theta < 140^\circ$ ($|\eta| < 1$) and having $P_t > 400$ MeV. Particles of $P_t \leq 400$ MeV perform complete spirals in the CTC and their reconstruction in the offline analysis is virtually impossible. In this polar angle range the momentum resolution is :

$$\frac{\delta P_t}{P_t^2} \leq 2\ 10^{-3} (GeV/c) \tag{2.3}$$

In the two adjacent intervals $20^\circ < \theta < 40^\circ$ and $140^\circ < \theta < 160^\circ$ CTC reconstruction efficiency and momentum resolution drop. One finds approximately

$$\frac{\delta P_t}{P_t^2} \geq 4\ 10^{-3}(GeV/c) \tag{2.4}$$

The CTC is divided into 84 layers of sense wires, arranged into 9 concentric superlayers, as shown in figure [17]. The five axial superlayers contain 12 layers of wires parallel to the beam providing the reconstruction of the track in the r-ϕ plane (perpendicular to the beam) with a space resolution of typically 200 μm. Four stereo superlayers are interleaved with the axial superlayers and comprise six layers of sense wires slanted at ± 3° with respect to the beam axis. A z resolution of 4 mm is obtained by means of this stereo system in the $r-z$ plane. Approximately the same resolution is expected from the CES chamber in the central calorimeter. The three additional layers of streamer drift tubes just outside the chamber provide a 3-dimensional space point with z-resolution of about 3 mm in the range $45° < \theta < 135°$.

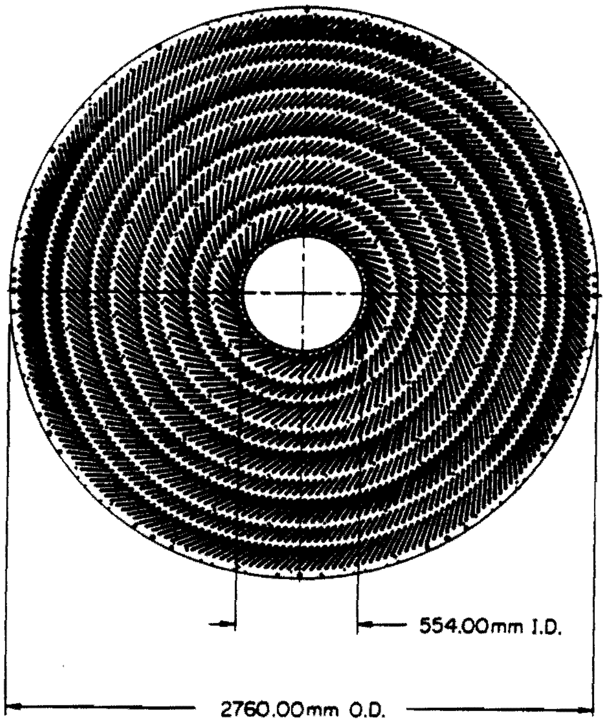

Figure 17: End view of the Central Tracking Chamber showing the location of the slots in the alluminum endplates.

An important feature of the chamber design is that the drift celles are tilted to form a 45° angle with a radial line, so that in presence of a 1.5 Tesla B field the electron drift trajectories are approximately azimuthal. An advantage in making the tilt angle so large is that cells as seen from the interaction center along the radial direction overlap with each other in azimuth. This in particular guarantees that every radial (high P_t) track must pass close to at least one sense wire in every superlayer. This property is used to generate a prompt trigger signal for high P_t muon candidates. It also helps in the offline analysis to resolve closely spaced tracks. This is of the greatest importance when measuring high P_t particles in jet cores. This design of the drift cells also helps resolving the left-right ambiguity in pattern recognition, because the ghost track is rotated in $r - \phi$ with respect to the true track by approximately 70°.

The main and most important task performed by the CTC is the identification and momentum measurement of isolated electrons and muons. The excellent job done by the CTC allows a very efficient tagging of W and Z leptonic decays in the region of coverage. As far as muons are concerned, the CTC provides the only measurement of the track P_t, because the muons, differently from the electrons, are minimum ionizing particles in the Central Calorimeter.

A further remark should be done on track finding efficiency and momentum resolution. The reconstruction of the track in the transverse plane is more efficient than in the $r - z$ plane. This is because the bulk of pattern recognition is done using the axial layers which are many more than the stereo layers (60 vs 24) and measure directly $r - \phi$ to within $\simeq 200\mu m$ (to be compared to the corresponding 3° stereo resolution of $\simeq 4$ mm in the z-direction). For tracks exiting the chamber from the front and rear end plates and crossing a number of layers less than maximum (84), the offline track finding program may fail in reconstructing the trajectory in the $r - z$ plane but still find the track in $r - \phi$ and give the correct P_t although with worse resolution. Another case of difficult (inefficient) reconstruction is the jet environment: in jet cores the presence of close tracks may cause misassigments of wire hits which affect more heavily the measurement of the z coordinate than $r - \phi$. In jet cores, there is a small but not negligible fraction of cases in which the θ direction of the track is not reconstructed (two-dimensional tracks).

The excellent space and momentum resolution of the CTC has allowed the identification and measurement of secondary vertices in the decay of long lived K°'s and Λ's. By matching of isolated tracks to shower centroids measured in the calorimetry the response of the central calorimeter as a function of momentum and has been extended to particles of momentum below 10 GeV/c . A task performed by the central tracking chamber which has been exploited in the present work is the identification of the amount of charged energy directed at cracks or holes in the calorimetry (correcting for this effect is especially important when studying events with apparent large missing E_t).

Accounting for calorimeter response to low P_t particles and for energy directed towards cracks are issues of the greatest importance when dealing with tracking corrections to jet energy and momentum, as it will be made clear in the following Chapters.

2.5 The 1987 Run and Trigger

The total cross section expected for p pbar interaction at $\sqrt{s} = 1.8$ TeV is $\sigma_{tot} \simeq 80$ mb. With a luminosity of $L = 10^{-30}$ $(cm^{-2}sec^{-1}) = 1$ $\mu b^{-1}sec^{-1}$ the rate of events is of the order of 80 KHz. Technical constraints coming from the *CDF* data acquisition structure forces the trigger to reduce the rate of accepted events of a factor 8000, down to 1-2 hertz, which is the rate at which data can be logged to tape.

The rate of physically interesting events is a small fraction of the total rate. For instance, the cross section for W production is 18 nb, roughly 2.5 10^{-7} of σ_{tot}. The trigger must be capable of rejecting in a very short time the large majority of the events and still be highly efficient in accepting these very rare interesting events. It also must have enough flexibility to be changed during the run depending of the results of the experiment. This is the reason why the *CDF* trigger is organized into different levels of decision, higher levels operating at lower rates and requiring longer decision times. The highest level (Level III) is a software trigger.

In the 1987 run only Level 0 and Level 1 were operating, with a decision time less than 7 μsec, the time interval between two subsequent bunch crossings. The *CDF* calorimetry is divided into a matrix of 24 x 42 "*trigger towers*" in the $\phi - \eta$ plane, each one of them covering 15° in ϕ and 0.2 units in η. A trigger tower corresponds to two physical towers in the central region and to six in the gas calorimeter.

A coincidence from the *beam − beam counters* (BBC) at the proper crossing time made up the Level 0 trigger. The BBC are a set of scintillator hodoscopes placed in front of the forward and backward calorimeters. These hodoscopes were also used as a luminosity monitor. The Level 1 trigger allowed for a mix of triggers corresponding to various physics streams. The sum of E_t of all trigger towers was built in hardware both for the E.M. compartment and for the complete Central Calorimeter, and signals were compared to adjustable thresholds.

The trigger channels used during normal running were :

1. MINIMUM BIAS - a prescaled trigger using only Level 0,

2. HIGH E_t trigger, requesting $\Sigma E_t > 20$ to 45 GeV depending on luminosity, in the central calorimeter ($|\eta| < 1.1$),

3. ELECTRON trigger, with $\Sigma E_t > 15$ GeV and the sum was over the EM calorimeter towers only,

4.a CENTRAL MUON trigger, provided by a fast signal indicating a track in the CTC with $P_t > 3$ GeV in coincidence with a track in the central muon chambers,

4.b FORWARD MUON trigger indicating penetrating particles within azimuthal bins in the forward muon toroids. During the 1987 run this trigger had to be prescaled because of excessive background rate, and collected data were used primarily for debugging.

This "buffet" trigger was adjusted by prescaling the minimun bias and forward muon triggers and by varying the thresholds on the ΣE_t and electron triggers so that the total rate written on tape was about 1 Hz, indipendent of the instantantaneous luminosity.

The jet sample used for this work is found in the events which passed the large E_t trigger. The efficiency of the trigger selection can be estimated by comparing data with different trigger thresholds. Typically at energies of 10 GeV above the nominal trigger threshold, the trigger is found to be fully efficient. The total integrated luminosity was 26 nb^{-1}. This absolute luminosity is uncertain by approximately 15 %. This limitation was due to a number of internal inconsistencies among accelerator and *CDF* trigger monitors during the 1987 run. Also, the calibration constants of the *CDF* monitor depends on the partial cross-section accepted by the BBC. This was computed by Monte Carlo, using the expected total cross-section as an input.

3 Offline Processing

3.1 Jet Algorithm

The first step of the offline processing of the events that fired the total transverse Et triggers is the isolation of jet structures from the raw calorimetric information. For this purpose, *CDF* has developed three basic algorithms and has carried out a number of tests to determine the best one. They consist of a nearest neighbour algorithm, a cone algorithm with a transverse energy dependent cone size and a fixed cone algorithm. The one which is indicated by the Montecarlo to allow a better jet energy/momentum resolution is the fixed cone algorithm ("*jetclu*", ref. [6]). This algorithm also has the advantage of being most readily applicable to *QCD* comparisons.

Jets are identified by jetclu as local clusters of energy in the calorimeter, with a procedure which passes through two stages. In the pre-clustering stage, a list of towers with $E_t > 1.0$ Gev (seed towers) is formed and preclusters are defined as an unbroken chain of adjacent towers with continuously decreasing E_t.

In the next stage, if the total energy of a precluster is greater than 2 GeV, it is used as a starting point for clustering. The E_t weighted centroid of the precluster is calculated, a cone of fixed radius R in $\eta - \phi$ space is formed around it and all the towers inside the cone whose E_t is greater than some threshold (E_{tmin}) are included. A new centroid is then calculated with this new set of towers and this process is repeated until the list of towers which fall inside the cone remains unchanged. The ambiguous case in which two clusters overlap is resolved by merging them if either cluster shares more than 0.5 of its energy with the other. Otherwise they are kept separate and the towers which are in common are associated to the nearest of the two.

R and E_{tmin} are two important parameters of the algorithm. In the data used in this work:

$$R = 1.0 \qquad\qquad E_{tmin} = 0.1\,GeV. \tag{3.1}$$

The jet 4-vector is formed using all the clustered towers : jet energy (momentum) is defined as the scalar (vector) sum of the tower energies (momenta). In the definition of jet momentum, calorimeter signals are considered as being generated by massless particles with momentum pointing along the direction that projects the tower back to the vertex of the interaction as measured by the VTPC. It's clear that this is only an approximation to reality, in particular in the case of several particles entering the same tower (this however is not likely given the fine tower segmentation of the calorimeter). The bending of charged particles in the 1.5 T magnetic field represents another source of deviation from the true jet momentum. Actually, using the tracking information jet 4-vectors can be corrected for this effect. The remaining limitation is due to very low momentum particles which are bent by the field away from the main cluster. This small effect must be accounted for in average in a Montecarlo calculation. Finally, the shift of the measured interaction vertex from the the nominal $z=0$ position also introduces an error in the measurement of jet direction. To reduce this effect and take more advantage of the projective geometry of the calorimeter, only events with an interaction vertex within 60 cm from the center of the detector are processed in the analysis.

The conclusion is that the *CDF* calorimeter, beacause of its fine granularity, measures quite well the jet full 4 - vector. The momentum resolution is sligthly worse than energy resolution. The ultimate energy and momentum resolutions that can be achieved after applying a number of corrections are discussed at lenght in the following.

3.2 Jet Background Cuts

The second important step of the offline processing of the jet sample is the removal of spurious events like background deposits of large energy roughly in coincidence with a minimum bias event,causing a large E_t calorimeter trigger. These events can be caused for exemple by cosmic ray bremsstrahlung and by radiation splashes from the Main Ring. The E_t dependence of these events is much flatter than the *QCD* spectrum that we are trying to measure. Unless they are removed they would dominate the signal at large M_{jj}. An obvious source of background is single phototube discharges. The so-called hot spots, that were mentioned in Chapter II, also fall in this cathegory. This kind of background is efficiently removed from the sample by looking at the ratio of the signals from the two phototubes in each tower.

The two most significant sources of large E_t background are beam-losses from the Main ring and cosmic rays which bremsstrahlung in the calorimeter. The Tevatron injector runs in the same tunnel as the main accelerator and although it is bent over at the *CDF* intersection (B0 hall), it still runs at only about 6 m above the central calorimeter. Most of background events of this kind can be suppressed using the hadron calorimeter TDC information: a cut demanding < 8 GeV of transverse energy outside a 35 nsec window and within a $\simeq 100 nsec$ wide gate around the beam crossing time eliminates .99 of them. The remaining background consists of in-time cosmic rays depositing energy only in the CEM calorimeter, which is not instrumented with TDC's. Additional cuts (on EM fraction, charged energy fraction and missing E_t) are applied for events with one or more central jets above 70 GeV to indicate that jets do not show any extremely anomanolous deviation from standard QCD predictions. For this particular purpose, the missing E_t is idefined as the vector sum of jet P_t's greater than 5 GeV. These cuts are seen to eliminate most of background events and leave less than .01 background contamination at any jet E_t.

3.3 Selection of an Inclusive two Jet Central Sample

The aim of the present work is to study events in which the hard scattering of two partons gives rise to two partons in the final states, that CDF detects as jets. In order to ensure uniform detector and trigger response a set of fiducial restrictions are applied to the jet sample. First of all, in order not to loose the advantage of the fine granularity and projective geometry of CDF, only events with a vertex located within ± 60 cm of the center of the detector are accepted. Then, after ordering all jets with decreasing E_t, the pseudorapidity of the two leading clusters is restricted to be $-0.8 < \eta < 0.8$. This value is chosen on the basis of several experimental reasons :

1) This ensures that most of the total E_t in the event has been measured in the calorimeter region that was used in the trigger ($|\eta| < 1.1$).

2) This is the region where the CEM, CHA and CTC have full and uniform acceptance. These detectors are known to have the best performance among all calorimeters and tracking systems of CDF.

3) As it will be shown in great detail in the following (Chapter IV), this choice allows important corrections to be made to the jet 4-vectors, by means of the precise information that the CTC provides the charged component of the jets.

At this stage of the analisys, no condition is put on the presence of additional jets. Figure [18] shows the distribution of the number of reconstructed jets per event. The event sample selected in this way from the entire large E_t data will be called from now on the "*inclusive two jet central sample*". The cuts that are described here are only meant to select the events that can reasonably be considered as good candidates for the measurement of the two jet cross section. In Chapter V the final selection of the events will be done with physics-oriented cuts of calculable efficiency.

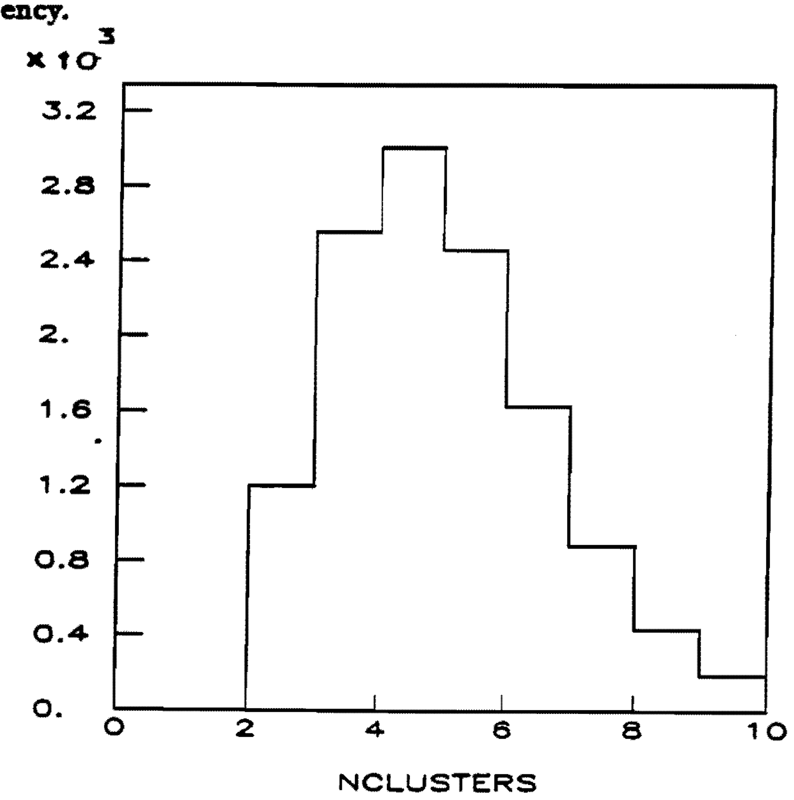

Figure 18: Number of reconstructed jets per event.

In the following paragraph we introduce a method that looks suitable to study how well these candidate events are measured by the central calorimeter. Then, the bulk of Chapter IV is devoted to the description of the possible corrections that can be applied to the jet 4-vectors in order to improve the resolution of the calorimeter measurement. Finally, at the end of Chapter IV it is shown how the same technique developed to study jet energy resolution provides a handle to show the improvement in the the jet energy/momentum resolution after corrections.

3.4 Energy/Momentum Resolution Studies

3.4.1) Guidelines for gauging the resolution

Central calorimeter response to single particles is known from the test beam for energies greater than 10 GeV. Any information concerning the resolution for jets, instead, has to came from the analysis of data collected during the run or from Montecarlo simulation. Our study has been largely based on data, while detector simulation has been used for comparison and to estimate physical quantities which could not be extracted from the data. Studying central calorimeter resolution using simulated instead of real data would be much easier because we deal with effects due to known sources. On the other hand, there is always an open question about the simulation reliability which leads us to conclude that parameters extracted from the real data are safer and should be used whenever possible.

In order to measure and then optimize the jet energy resolution, since the jet energy before hitting the detector is unknown, we need to find a tool which is as sensitive as possible to the absolute value of the resolution. It should be pointed out that we are talking about the resolution of two different observables: jet energy and jet momentum. In fact, in a previous section of this Chapter (jet algorithm) it has been shown that $theCDF$ calorimetry can measure the full jet 4-vector because of its fine tower segmentation. It's clear, however, that momentum is measured with a relative error larger than energy. Given the definition of momentum, one finds $P_{jet} = E_{jet}\ f$, where f is some factor < 1 depending on the energy distribution within the jet cone. This factor can also fluctuate and this fact introduces an additional error. Since we are interested in the invariant mass of a system of two (or more) jets calculated using the full 4-vectors, we would like to know the resolution of energy and momentum separately. In events with two jets whose momenta in the transverse plane are approximately equal and back to back, the ratio between the contributions to the error on the mass squared of momentun and energy is $\frac{(1+\cos\phi)^2}{4}$, where ϕ is the angle between the transverse momenta. If momenta are exactly balanced, then $M_{jj} = E_1 + E_2$ and the effect of momentum resolution is null. In general, in our sample the error made in estimating the invariant mass is mainly determined by the energy resolution. Momentum resolution becomes important when systems with three or more jets are included.

At the hadron colliders there is no direct way of measuring jet energy resolution from real data, by comparing the energies at production and after measurement. This can only be done using Montecarlo generated events and computing the expected signal after a detector simulation. One reasonable assumption can be that the colliding partons have zero momentum in the plane transverse to the beams. Any non-zero value of the total P_t measured in the final state would therefore be attributed to experimental errors or final state effects. If final state effects are also small, the overall transverse unbalancing in a jet system could be a meter for jet energy measurement errors.

The magnitude of the total $\vec{P}_t$ of the event (whose opposite is called missing transverse energy), is influenced by the resolution of CDF as a whole. $\vec{P}_t^{total}$ is defined as the vector sum of the transverse energies of all calorimeter towers. Also, any true missing E_t is a property of the event as a whole (e.g. jets associated to W production and leptonic decay). It contains a contribution from the hard 2 $\rightarrow$2 scattering (the jets), and another from the underlying event. All in all, it looks difficult to disentangle just the effect of resolution in jet energy, in a study of the total missing E_t that is equally affected by the finite resolution of calorimeters other than the central ones and by physical processes other than production of jets. We are interested only in the jet-component of the event and we would rather need a quantity which tells us only about the hard subprocess of the collision. As a possible solution of the problem, we choose to use the sum of the transverse momenta of all jets recostructed in the event. From now on we will refer to it as the "*transverse kick*" of the system of the jets (K_t), or "P_t *unbalance*". The width of the K_t distribution is largely influenced by the resolution in jet energy/momentum measurement. However, some contribution can also be contributed by the underlying event. Also, some partons produced in the hard interactions in addition to the two leading ones may fail being reconstructed as jets. This "*physical*" component will have to be subtracted from the experimentally measured K_t, in order to unfold the contributions due to errors in jet energy measurement.

When the contributions to K_t of jet energy resolution and of underlying event become comparable, the size of the subtraction is large and the distinction between the two components is uncertain. For example, at $E_{jet} < 20$ GeV, jet reconstruction suffers from known inefficiencies (as monitored by failures in reconstructing recoil jets in direct photon events). When jet recognition is problematic, K_t might be due to lost jets by the clustering algorithm and it would be wrong to assign all of it to either errors in measuring the detected jets or to the underlying event or to the primary P_t of the parton-parton interaction. At high energies the situation looks more favourable. Our study has been done for jets of energy $E_{jet} >30$ GeV.

In the next paragraph, the technique will be fully developed. It will be shown that a proper selection of events from the previously defined inclusive two jet sample allows the momentum resolution of the central calorimeter to be measured. It will also be shown that momentum resolution represents a good estimate of the upper bound of the energy resolution.

3.4.2) Definition of K_t for two or more jets

The K_t vector for a system of n jets is defined as the total transverse momentum of the n jets :

$$\vec{K}_t = \sum_i^N \vec{P}_{t_i} \tag{3.2}$$

where $\vec{P}_{t_i}$ is the transverse momentum of the i-th jet. With reference to two orthogonal axes in the transverse plane (ξ, η), consider the components of $\vec{K}_t$ along them $(K_{t,\xi}, K_{t,\eta})$,and their standard deviations $(\sigma_\xi, \sigma_\eta)$. As described below, these two directions are chosen in such a way as to enhance the impact of calorimeter resolution on $K_{t,\xi}$.

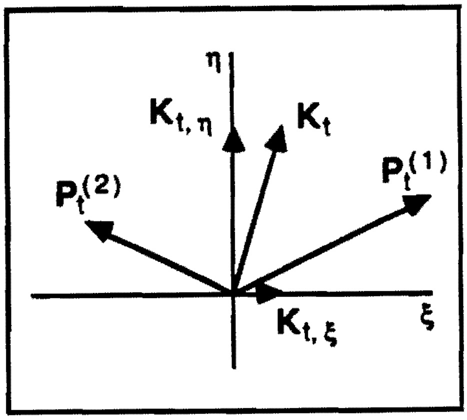

Figure 19: K_t definition in two jet events.

In the simple case of two jets, the η axis is the bisector of the angle between P_{t_1} and P_{t_2}, ξ is its conjugate direction. ξ is oriented positive towards P_{t_1} (fig. [19]). However, we randomly select which jet is 1 and which is 2. This definition follows the convention used by $UA2$, with the only difference that the K_t components can equally be positive and negative. When there are more than two jets in the event a new definition of the ξ and η axes must be given. We adopt an iterative procedure:

1) jets are ordered in decreasing E_t, and as in the dijet case the two highest E_t jets are randomly labeled 1 and 2;

2) the transverse momentum of the i-th jet of the list ($i > 2$) is used to form the scalar products $< P_{t_i}, P_{t_1} >$ and $< P_{t_i}, P_{t_2} >$;

3) the jet (1 or 2) which has the greater scalar product with the i-th jet is redefined by adding P_{t_i} to its transverse momentum;

4) points 2) and 3) are repeated until there are no jets left or the chosen maximum number of jets is reached.

This procedure allows to define two "*equivalent*" jets that are then used to define the ξ and η axes as in the two jet case. Figure [20] shows the case of three jets. Since the labels of the two leading jets been randomized, the mean of the $K_{t,\xi}$ and $K_{t,\eta}$ distributions is zero. The useful paramenters for our study are the standard deviations σ_ξ and σ_η.

From now on, when talking about the n jet K_t as opposed to the 2 jet K_t, we will use the terms "*Multijet* K_t" while using "*Dijet*" K_t for the second.

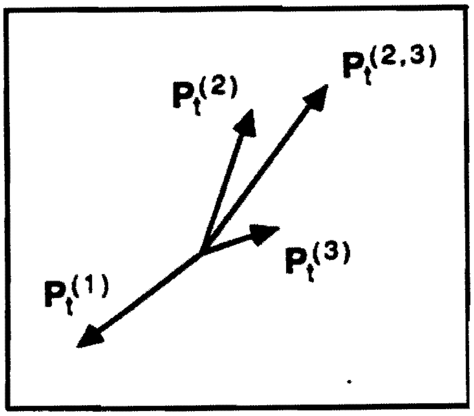

Figure 20: K_t definition in three jet events.

3.4.3) K_t and resolution in jet momentum

The spread σ_ξ is first determined by the momentum resolution, and next by any other final state contribution to the total P_t of the jet system. The initial state P_t can also give a contribution in principle. Errors in the measurement of the jets azimuth are expected to have a negligible effect on σ_ξ because of the way the ξ axis is choosen. This is surely true in the dijet case because jets in this sample are very narrowly back-to-back collimated. This empirical fact also shows that the original P_t cannot be very large.

σ_η is affected by angular resolution errors, as well as by the primary transverse momentum and by final state kick that also influence σ_ξ. We can assume that both these underlying "transverse kicks" are uncorrelated to the ξ and σ directions. Under this assumption, σ_η can be useful to "*subtract*" the effect of these physical sources of P_t-unbalance that add to finite calorimeter resolution to determine the σ_ξ.

The calorimeter measures P, ϕ, and θ of each jet with finite errors σ_P, σ_ϕ, σ_θ. In analogy with the single particle case we assume that momentum calorimeter resolution behaves for jets like :

$$\sigma_{P_i} \; = \; \alpha\sqrt{P_i} \tag{3.3}$$

Since :

$$K_{t,\xi} = \sum_i P_{t_i} \cos\phi_{\xi_i} \; = \; \sum_i P_i \sin\theta_i \cos\phi_{\xi_i} \tag{3.4}$$

(where for each jet θ and ϕ are, respectivally, the polar angle and the angle between the $\vec{P}_t$ and the ξ axis) the experimental resolution propagates into σ_ξ^2, giving the following three terms :

$$\delta_\xi^2 = \sum_i (\sigma_{P_i}^2 \sin^2\theta_i \cos^2\phi_{\xi_i} + \sigma_\theta^2 P_i^2 \cos^2\theta_i \cos^2\phi_{\xi_i} + \sigma_\phi^2 P_i^2 \sin^2\theta_i \sin^2\phi_{\xi_i}). \tag{3.5}$$

The effect of the θ term can be neglected because in our sample is suppressed by the requirement that the two E_t leading jets be very central. Similarly, the ϕ-term is made negligible by the way the ξ axis is defined (ϕ_ξ about zero for the highest P_t jets). Thus, using eq.(3.3) to express $\sigma_{P_i}^2$ as a function of P_i, the total ξ width can be expressed in the following way :

$$\sigma_\xi^2 = \alpha^2 P_\xi + (soft)^2 \tag{3.6}$$

where P_ξ is defined as

$$P_\xi \; = \; \sum_i P_i \sin^2\theta_i \cos^2\phi_{\xi_i} \tag{3.7}$$

$(soft)$ is the contribution of the recoil of the underlying event and of the initial state transverse kick, which adds in quadrature with momentum resolution.

As far as the eta component of K_t is concerned, we have :

$$K_{t,\eta} = \sum_i P_{t_i} \cos\phi_{\eta_i} \; = \; \sum_i P_i \sin\theta_i \cos\phi_{\eta_i} \tag{3.8}$$

$$\delta_\eta^2 = \sum_i (\sigma_{P_i}^2 \sin^2\theta_i \cos^2\phi_{\eta_i} + \sigma_\theta^2 P_i^2 \cos^2\theta_i \cos^2\phi_{\eta_i} + \sigma_\phi^2 P_i^2 \sin^2\theta_i \sin^2\phi_{\eta_i}) \tag{3.9}$$

The contribution of the error on θ is negligible, like for σ_ξ, since all our jets are approximately at 90° while the contribution of the ϕ-error is now important. Therefore :

$$\sigma_\eta^2 = \alpha^2 P_\eta + \sum_i \sigma_\phi^2 P_i^2 \sin^2\theta_i \sin^2\phi_{\eta_i} + (soft)^2 = \alpha^2 P_\eta + \sigma_\phi^2 \sum_i P_i^2 \sin^2\theta_i \cos^2\phi_{\xi_i} + (soft)^2 \tag{3.10}$$

where P_η is defined, similarly as for P_ξ,

$$P_\eta \; = \; \sum_i P_i \sin^2\theta_i \cos^2\phi_{\eta_i} \; = \; \sum_i P_i \sin^2\theta_i \sin^2\phi_{\xi_i} \tag{3.11}$$

The quantity P_ξ can be considered as a sort of "*equivalent*" momentum of the system of jets of which we are probing the resolution. The constant it is multiplied by in the eq. (3.6) is the parameter expressing the resolution for a *single* jet. This will be an average of the resolution over the various *CDF* calorimeters detecting the multijet system. In the multijet central sample, since the two E_t leading jets are very central, α is strongly influenced by resolution of the scintillator calorimeters. In the two central jet sample, α will depend only on the resolution of the central calorimeter.

In the conjugate direction, the equivalent momentum P_η is a small quantity whose width is strongly influenced by errors other than the calorimeter energy resolution. Therefore, a useful parameter when studing the resolution of a system of jets in the equivalent two-jet representation is in practice only P_ξ.

An important hypothesis was done in writing equations (3.6), (3.10). The contribution $(soft)^2$ of the underlying recoil to σ_ξ and σ_η is assumed to be the same, i.e. the transverse kick is assumed to be uniformly distributed on the transverse plane. This is a natural assumption for a possible transverse kick of the primary partons, but is a dynamical assumption as far as the final state kick is concerned.

3.4.4) Multijet K_t versus Dijet K_t

Is it necessary to introduce a multijet K_t instead of balancing just the two leading central jets? The transverse unbalance of two jets may be sensitive to measurement errors only if a tight cut is applied on the third jet. Indeed, the presence of a third, fourth,.... jet would increase considerably the σ_ξ of the leading dijet and reduce its sensitivity to experimental errors. Figure [21] shows $|\vec{K}_t|$ when, for a sample of three jet events, K_t is computed using the two leading jets (Dijet K_t) or with all jets (Multijet K_t).

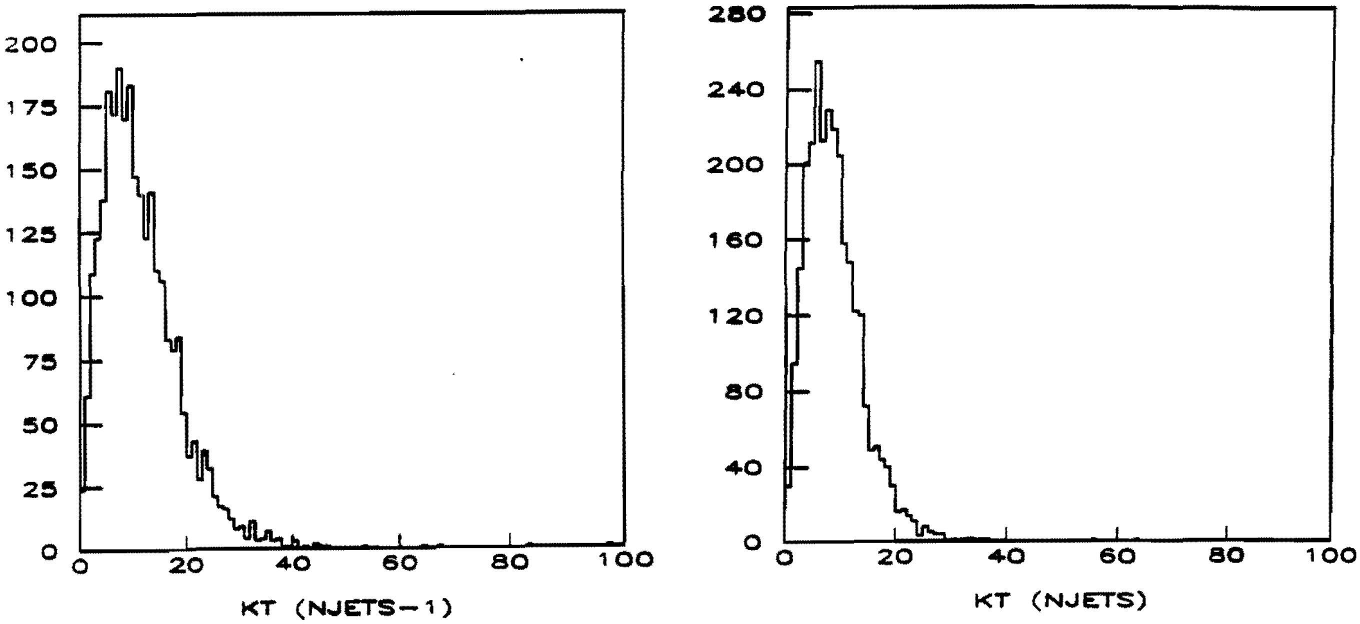

Figure 21: Dijet $|\vec{K}_t|$ (a) and Multijet $|\vec{K}_t|$ (b) in three jet events.

It is clear that overall transverse momentum conservation has a key role. Figure [22] shows, in three jet events, the correlation between the azimuth of the Dijet K_t and the azimuth of the third jet. One sees that the presence of a sizeable energy emission in the direction of the third jet distorts the Dijet K_t vector along that direction. For this reason, the Dijet K_t is a useful quantity to monitor the central calorimeter resolution only if a tight cut against additional clusters is applied. Otherwise the Multijet K_t must be used.

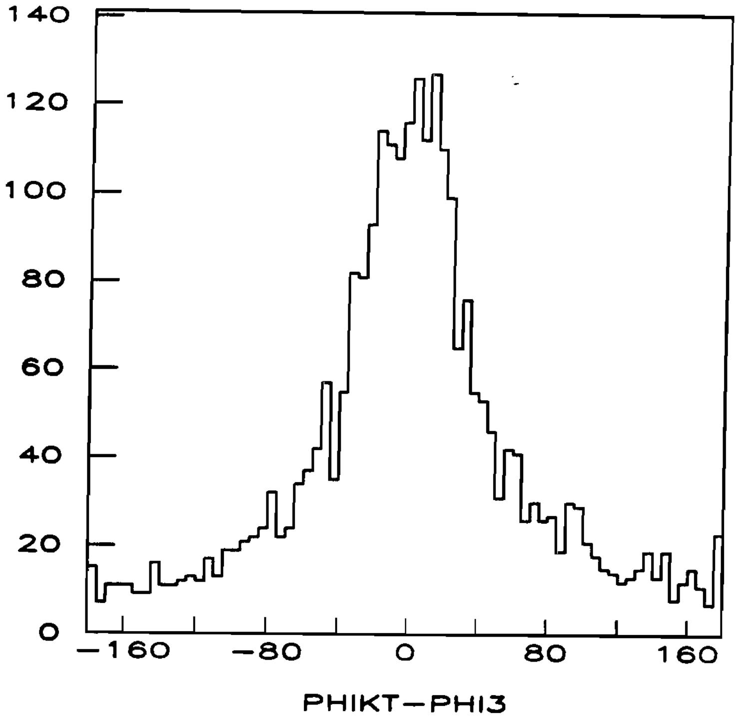

Figure 22: $\phi_{\vec{K}_t} - \phi_{\vec{P}_{t_3}}$ in three jet events.

Since a 5 GeV cut on third jet E_t produces a severe drop in statistics, the multijet K_t represents a good choice in order to save statistics. This may be needed when σ_ξ is used as a relative monitor of the effectiveness of various tracking corrections in improving energy resolution. If, instead, the purpose is to get an estimate of the absolute value of the resolution, the cleanest way is to study the central Dijet K_t under the requirement E_{t_3} <5 GeV. Figures [23] and [24] show, respectively, σ_ξ and σ_η as a function of $\sqrt{P_\xi}$ in the Dijet case (with the above-mentioned cut on the third jet), while figures [25] and [26] show the same quantities in the Multijet case.

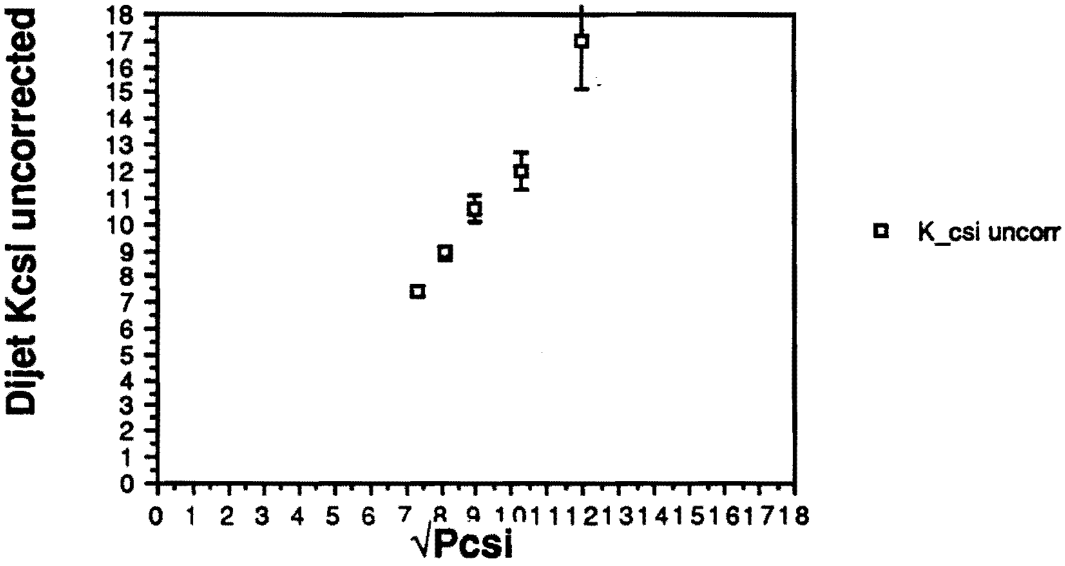

Figure 23: Dijet σ_ξ as a function of $\sqrt{P_\xi}$.

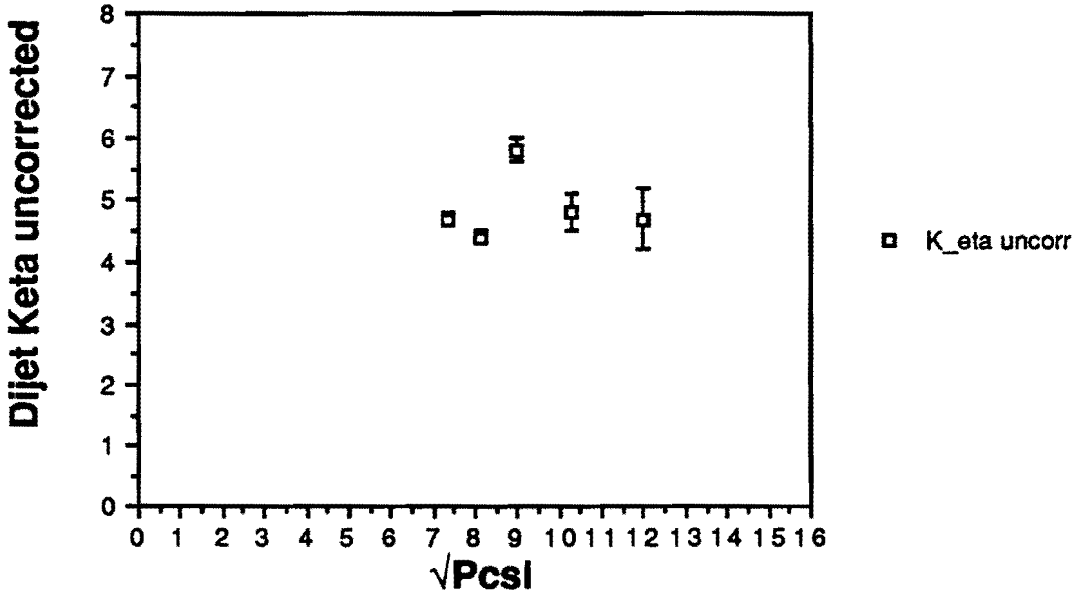

Figure 24: Dijet σ_η as a function of $\sqrt{P_\xi}$.

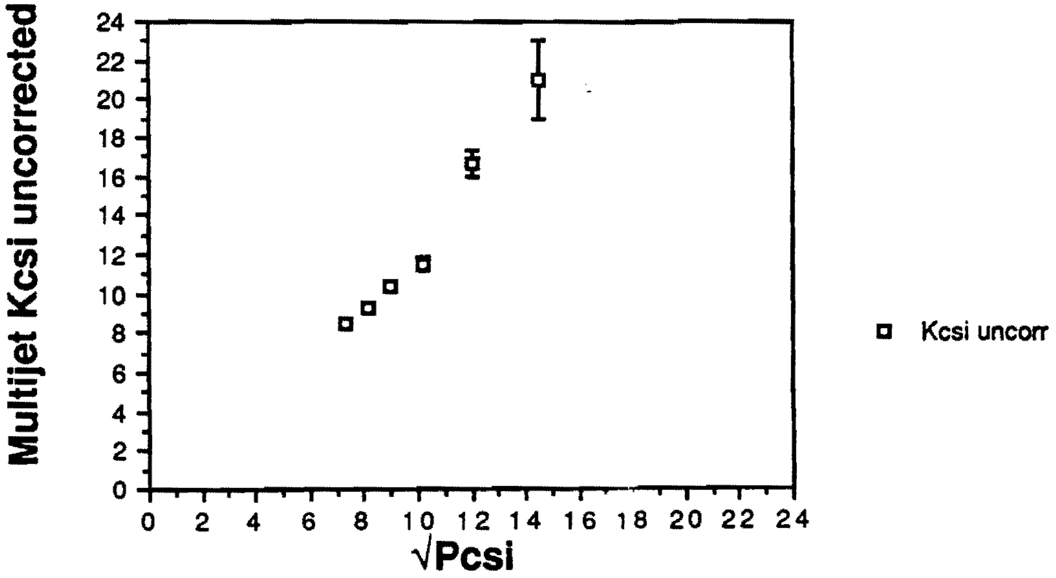

Figure 25: Multijet σ_ξ as a function of $\sqrt{P_\xi}$.

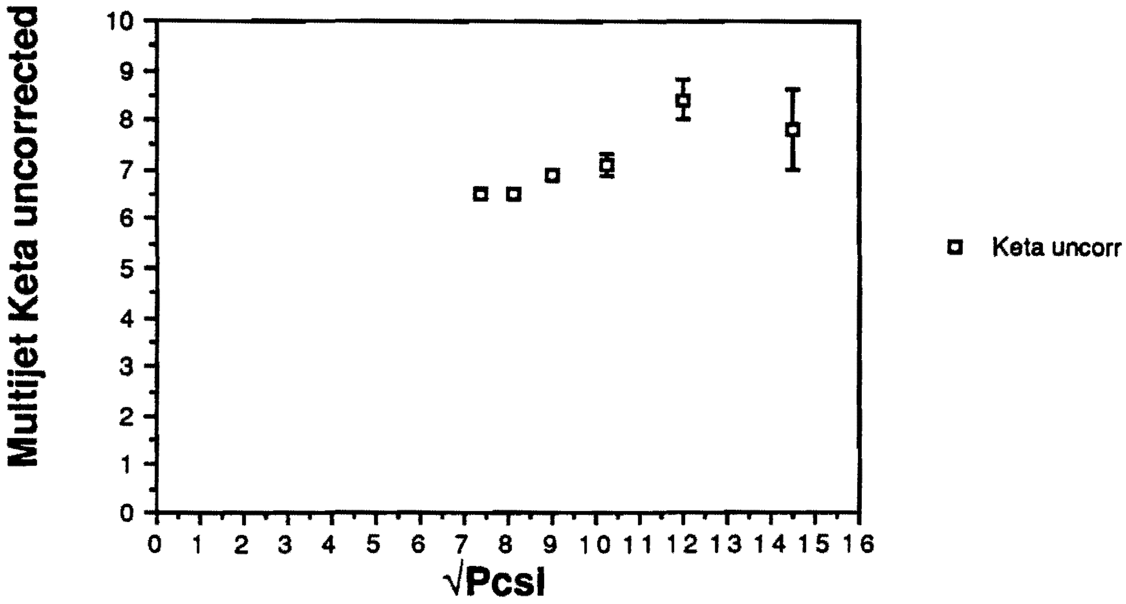

Figure 26: Multijet σ_η as a function of $\sqrt{P_\xi}$.

There are two additional reasons for cutting so tightly on the third jet :

1) only the central calorimeter contributes to the Dijet K_t, whose resolution (and not an average one among different calorimeters) is directly monitored,

2) P_η is very small and its contribution σ_η (eq. (3.10) can be neglected relative to the other terms.

When the cut $E_{t_3} < 5$ GeV is applied,the two central jets are very accurately back-to-back, i.e. $\sin\theta_i \simeq 1$,$\sin\phi_{\xi_i} \simeq 0$, $\cos\phi_{\xi_i} \simeq 1$. This means that P_η is negligible, and the angular term of σ_η can be written approximately as $\sigma_\phi^2(P_1^2 + P_1^2)$. Since $P_\xi \simeq P_1 + P_2$, eqs. 3.6, 3.10 become :

$$\sigma_\xi^2 = \alpha^2 P_\xi + (soft)^2 \tag{3.12}$$

$$\sigma_\eta^2 = \sigma_\phi^2 P_\xi^2/2 + (soft)^2 \tag{3.13}$$

The only quantity that is now needed in order to derive α^2, i.e. the jet energy resolution is σ_ϕ, the error in the calorimeter measurement of jet azimuth. We have computed σ_ϕ with ISAJET as event generator + QFL (an accurate detector simulation). Events were selected using the same cuts that define the inclusive two jet central sample. Figure [27] shows the dependence of σ_ϕ with P_ξ.

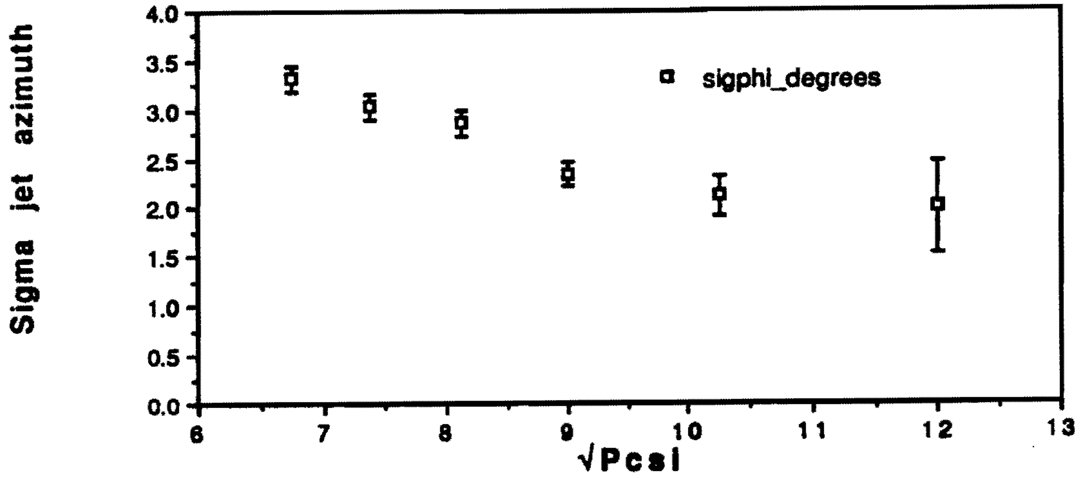

Figure 27: Error on the jet azimuth as a function of P_ξ.

This behaviour goes along with all expectations, because high P_t central jets (that is jets in events with a high value of P_ξ) are usually so collimated that the weight of the angular errors is smaller than for wide, low energy jets. By means of this result, for each bin of P_ξ, we finally perform the subtraction and call σ_ξ' the new quantity :

$$\sigma_\xi'^2 = \sigma_\xi^2 - (soft)^2 = \sigma_\xi^2 - (\sigma_\eta^2 - \sigma_\phi^2 P_\xi^2/2) \simeq \alpha^2 P_\xi \tag{3.14}$$

The slope of the plot σ_ξ' vs $\sqrt{P}_\xi$ (Fig. [28]) gives the central calorimeter momentum resolution as measured from jet balancing.

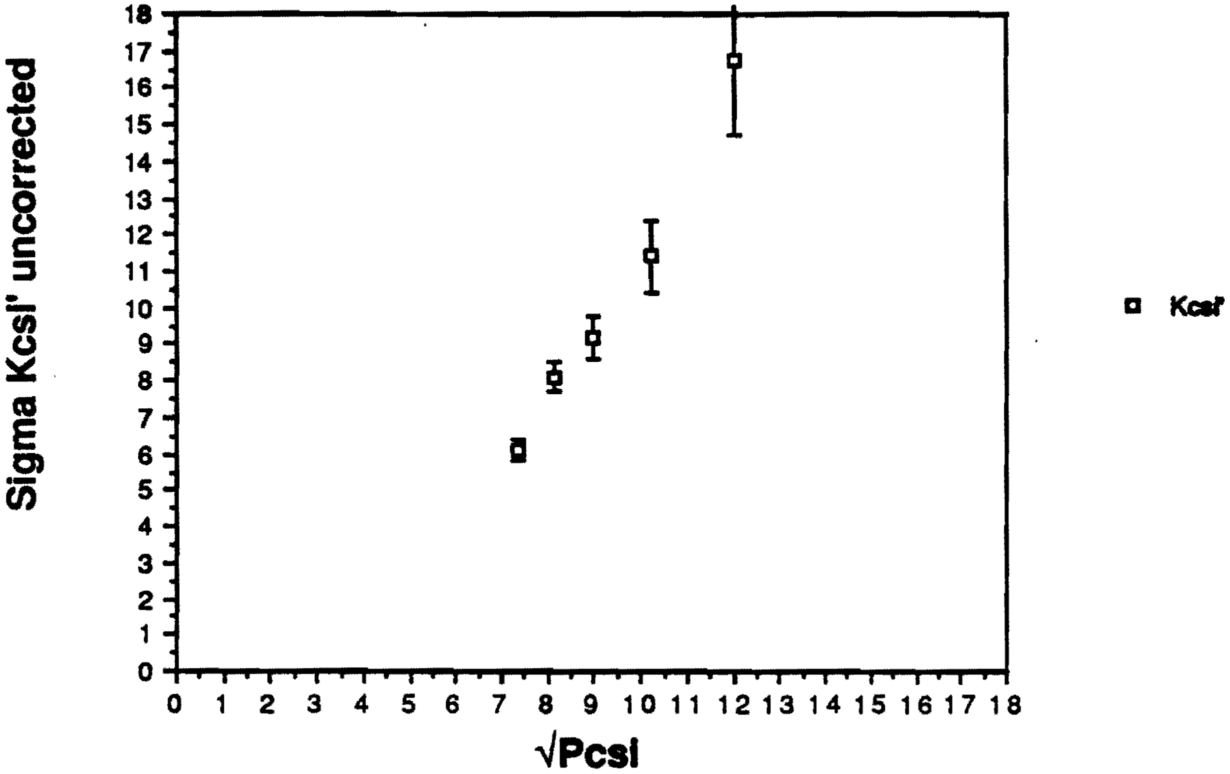

Figure 28: σ_ξ' as a function of $\sqrt{P_\xi}$.

In the next Chapter IV, the charged component is used to derive corrections to the jet 4-vectors as measured by the calorimeters. The residual P_t unbalance is used to test the effect of those corrections on jet energy resolution.

4 Corrections to Jet Energies

4.1 Correcting Calorimeter Nonlinearity and the Perturbation of the Magnetic Field

At CDF, measurement of jet energy/momentum is important for most high P_t processes. The response of the calorimetry to jets has previously been investigated via Monte-Carlo generation of jet events passed through detector simulation (ref.[1]) In this study, the Monte-Carlo generator (Isajet) has been tuned to produce jets with fragmentation properties (charged multiplicity, longitudinal and transverse momentum spectra) similar to those of jets observed in the CTC. Additionally, the detector simulation programs has been adjusted to reproduce the single particle response of the calorimetry. All detector effects were included as well as possible in the simulation Montecarlo CDFSIM. The jet energy scale was determined in average and in average accounted for calorimeter non-linearity, magnetic field effects, cracks, leakage and energy outside clusters. We refer to this correction (ref.[1]) as R_{686}, the inclusive correction of central jets.

In the central calorimetry the response non-linearity is the largest contribution to the correction. The response to high energy ($E > 10$ GeV) pions and electrons was measured in the test beam, where the absolute calibration of the calorimeter was made. The EM compartment response is determined with electrons (ignoring leakage), and the HAD response is measured using minimum ionizing pions in the EM compartment. Using this calibration prescription, and taking as energy in a cell the sum EM + HAD, the response to lower energy isolated tracks (mainly pions) has been studied in minimum bias events (ref [2]). The average response versus charged particle energy (shown in figure [29]) is clearly nonlinear with energy. Also shown are the charged pion responses from the QFL and CDFSIM programs, which reproduce the data reasonably well.

In jets, there are large fluctuations in both the neutral/charged components and in the energy sharing among hadrons. Thus the nonlinear calorimeter response causes not only a sizable energy underestimate but also a degradation of energy resolution and a clear bias towards

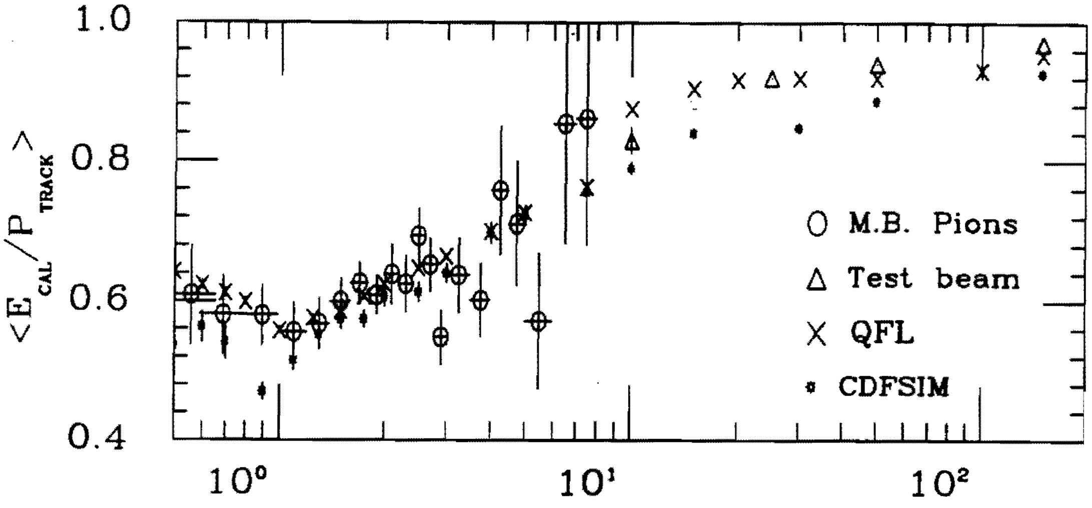

Figure 29: Central calorimeter relative response to charged pions, compared to the QFL and CDFSIM programs.

undermeasuring more the energy for jets with high charged multiplicity. In some other experiments, different weight factors are used for the two compartments in an attempt to improve the resolution. This was also tried in CDF on test beam data, with only a minor progress. Montecarlo calculations predict that no progress at all would be obtained for jets, after accounting for fragmentation fluctuations. On the other hand, in the central region of CDF, the non-linearity and magnetic field effects can be corrected for event by event, since the central tracking chamber measures the momenta of the charged fragments with high efficiency and good resolution.

In this paragraph , we describe the method adopted for making these corrections, while in the following section the remaining corrections for the underlying event and other effects are described. Results of using these correction on energy resolution are described in section 4.3. These corrections are described in detail in ref. [9].

The method to correct for non-linearity is conceptually simple : for each jet consider its associated charged tracks, obtain the contribution of each track to the jet energy and momentum using the known response, derive the amount of lost signal and correct the jet energy and momentum appropriately. We have chosen to apply the correction at the cluster level (as opposed to correcting tower by tower) for ease in analysis, and there is some arbitrariness in the criteria for which tracks to associate with which jet. The sensitivity to these choices for jets of moderate to high energies is seen to be small. More work will need to be done to understand these corrections for low energy jets ($E_t \sim 10$ GeV), for which this correction is extremely important.

For each event, we use jets whose detector eta is within $|\eta| < 2.0$. This cut is chosen so that the correction turns itself off gradually as jets get away from the CTC full acceptance region. This avoids introducing an abrupt nonuniformity. Tracks are associated with a jet if :

- the track passes some minimal selection criteria :
  (found in 3-d, impact parameter $|d| < 1.0$ cm, $|z - z_{vert}| < 5.0$ cm, ≥ 4 superlayers with data),
- the track has enough P_t to reach the central calorimeter (at $R_{CAL} = 172.7$ cm),
- the track total momentum is less than 100 GeV/c (protection against false or badly measured high momentum tracks),
- the track propagated to the central calorimeter radius does not hit the PEM face (at $|z_{PEM}| = 172.7$ cm). This acts as a cut in detector η of the track, well within the CTC acceptance,
- the track can be associated with the jet at the event vertex, or at the calorimeter, or both.
- the track is associated at the vertex if it is inside the clustering cone at the vertex : ($\Delta R = \sqrt{(\eta_{track} - \eta_{jet})^2 + (\phi_{track} - \phi_{jet})^2} < R_{cluster}$),
- likewise, the track is associated at the calorimeter if it is within the clustering cone when propagated to the calorimetry. This propagation is a helical extrapolation to the center of the solenoid coil followed by a straight line extrapolation to the strip chamber radius,
- if the track can be associated with more than one jet at either the vertex or the calorimeter via these criteria, select the jet with the minimum ΔR to the track.

The track association is shown in figure [30].

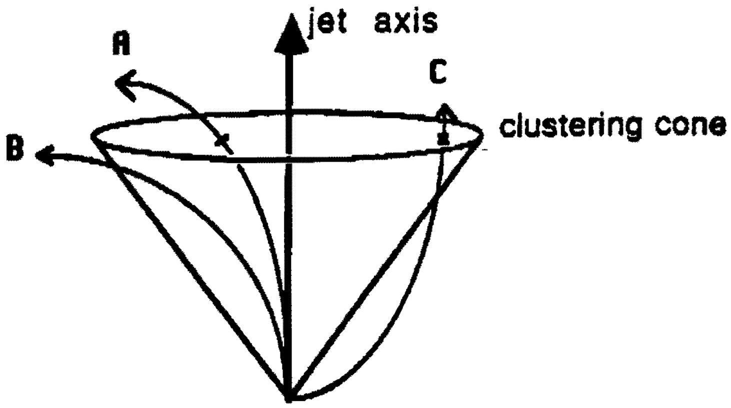

Figure 30: Association of tracks to jets. Track A is within the clustering cone in η-ϕ both at the vertex and the calorimeter. Track B is associated only at the vertex, and track C is associated only at the calorimeter.

If a track is associated to a jet only at the vertex, we assume that it is part of the jet so its contribution to the jet's 4-momentum should be the full track's 4-momentum after correction. On the other hand, if a track enters the cluster at the calorimeter via the magnetic field, we say it does not really belong to the jet and subtract its energy. The average measured response for a given track energy is obtained using a look-up table based on the measured relation shown in figure [29].

As mentioned above, the correction to jet energy can be split into two parts - the nonlinearity correction which compensates for undermeasured energy for tracks associated both at the vertex and at the calorimeter :

$$E_{nonlin} = \sum_{i=1}^{n_{both}} (|P_i| - < E_{meas} >_i)$$

and the B-field correction for tracks which exit or enter the jet from the magnetic field:

$$E_{Bfield} = E_{out} - E_{in} = \sum_{i=1}^{n_{out}} |P_i| - \sum_{j=1}^{n_{in}} < E_{meas} >_j$$

$$E'_{jet} = E_{jet} + E_{nonlin} + E_{Bfield}$$

The jet momentum is corrected by scaling the individual momentum components along the jet axis so as to preserve the jet direction. This method is implemented as:

$$|P'_{jet}| = |P_{jet}| + |P_{nonlin}| + |P_{Bfield}|$$

$$|P_{nonlin}| = \sum_{i=1}^{n_{both}} (|P_i| \cos\zeta_v - < E_{meas} >_i \cos\zeta_c)$$

$$|P_{Bfield}| = \sum_{j=1}^{n_{out}} |P_j| \cos \zeta_v - \sum_{k=1}^{n_{in}} < E_{meas} >_k \cos \zeta_c$$

where the angles ζ_v and ζ_c are those between the track and the jet at the vertex and calorimeter. It should be noted that although the pion response was measured only for $|\eta| < 0.6$, we apply the correction for tracks out to $|\eta| = 0.8$ and assume uniformity through that range.

We now show some results of applying the above correction to jet data from the 1987 run, using a clustering cone of size 1.0. Only jets above 10 GeV cluster E_t were corrected. The number of tracks used per jet is shown in Figure [31], with an average of 7 to 8 for the range of jet energies in the sample. Charged particles in jets at a large $|\eta|$ are not efficiently reconstructed by the CTC and the number of associated tracks decreases at the η boundaries. Figure [32] shows the size of the correction factor to jet energy (corrected/uncorrected) for the sample as a whole. The mean is ~1.2. In both the figures [31] and [32], the curves are normalized to arbitrary scales. The relative correction decreases slowly with increasing energy as shown in figure [33]. Figure [34] shows the mean correction as a function of detector eta for jets with $E_t > 10$ GeV, fairly uniform for $|\eta| < 0.6$ and then falling off due to the limited CTC acceptance. The amount of energy entering or exiting clusters due to the magnetic field is histogrammed in figure [35]. As expected, more energy tends to exit the jet cone than to enter the jet from the underlying event. Both E_{out} and E_{in} are fairly constant as a function of jet energy, as shown in figure [36].

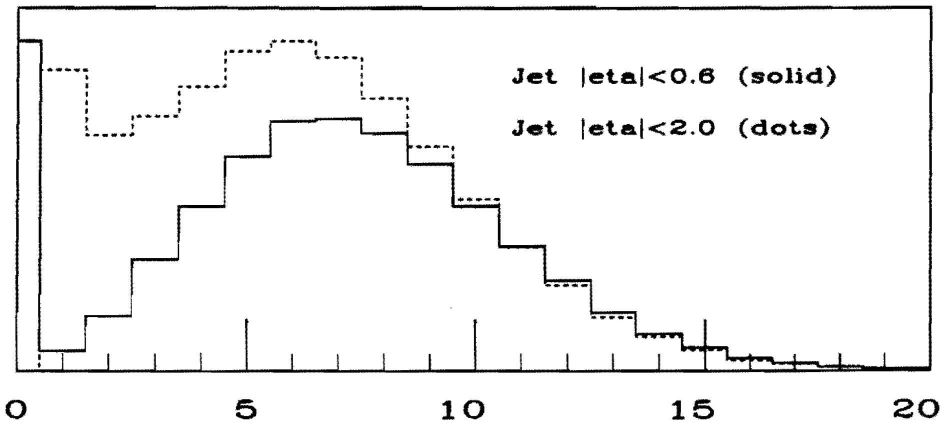

Figure 31: Number of tracks per jet which were associated at the event vertex.

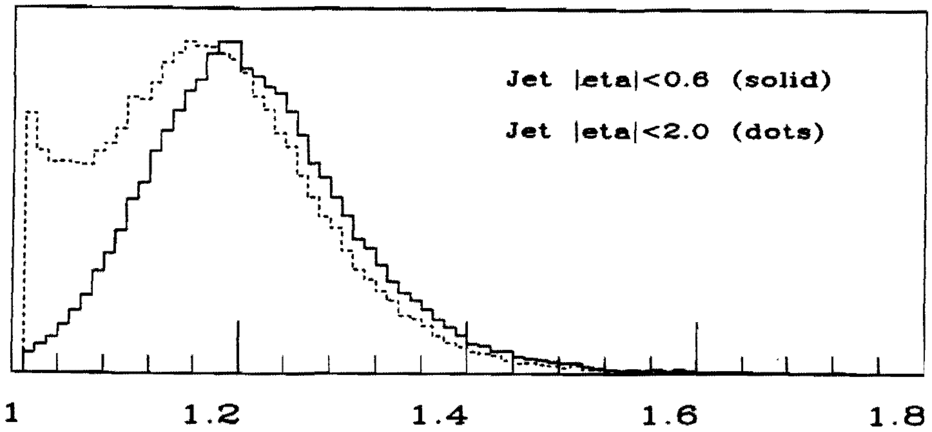

Figure 32: Correction factor to jet energy per jet.

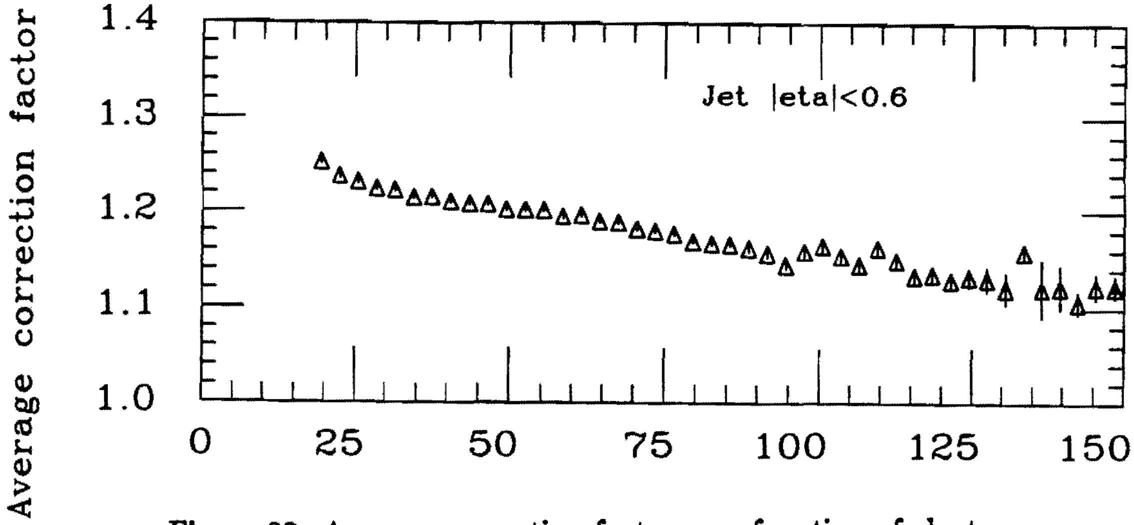

Figure 33: Average correction factor as a function of cluster energy.

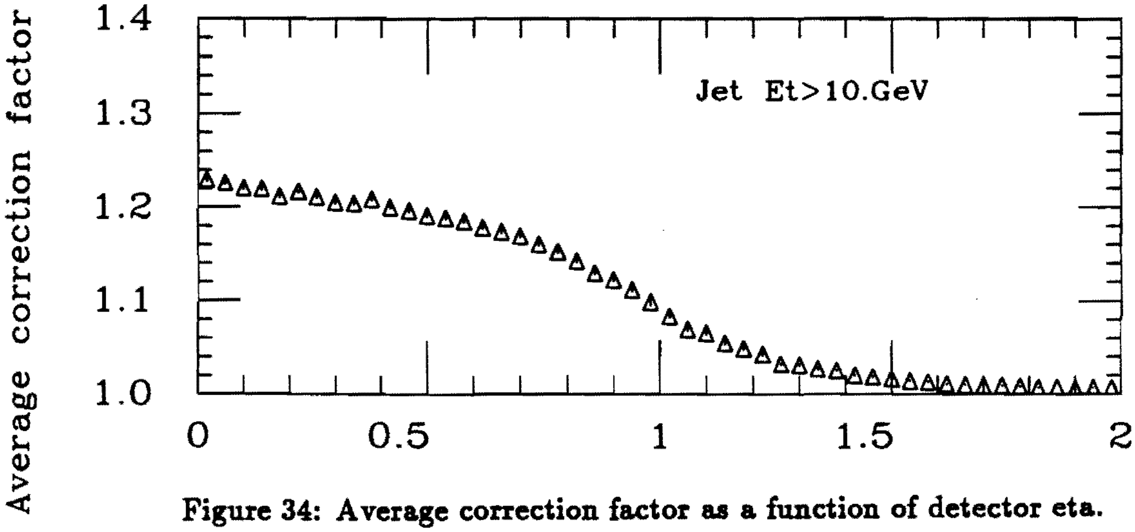

Figure 34: Average correction factor as a function of detector eta.

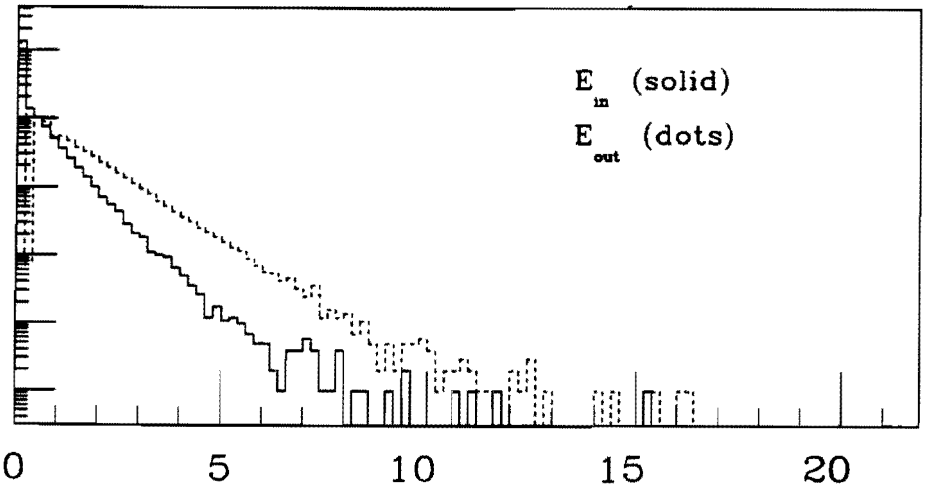

Figure 35: Energy entering clusters (E_{in}) or exiting clusters (E_{out}) due to the magnetic field.

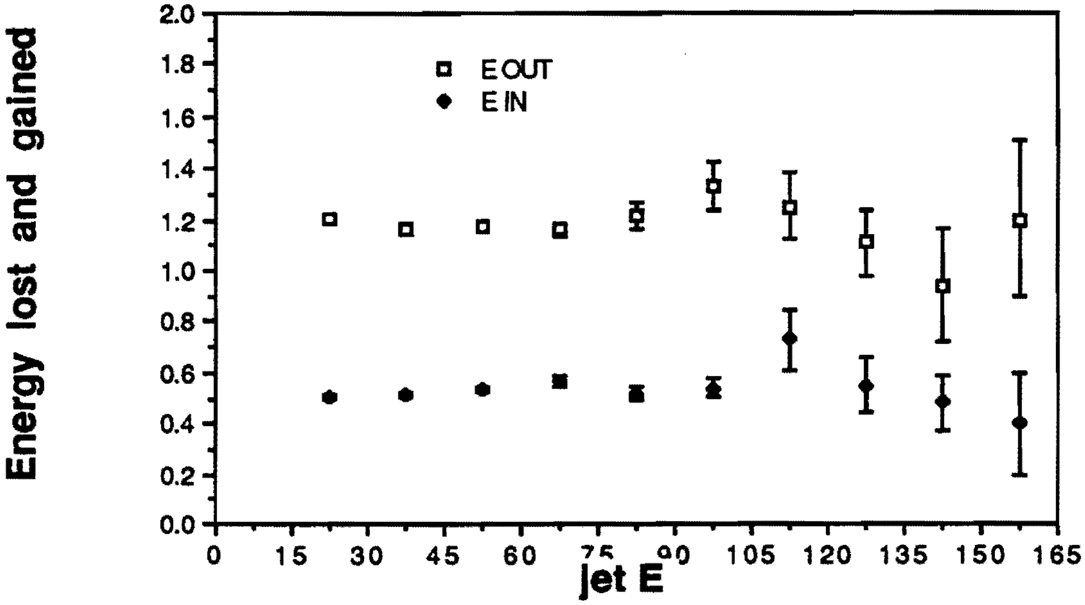

Figure 36: Average of energy entering clusters (E_{in}) or exiting clusters (E_{out}) as a function of jet energy.

4.2 Restoring the correct energy scale

In our standard analysis, for any uncorrected cluster energy $E_{cluster}$, the jet energy at production E_j is obtained by means of an inclusive scale factor which account for all possible systematic effects that we (R_{686}) have been able to think of :

$$E_j^{inclusive}(E_{cluster}) \;=\; R_{686}(E_{cluster})\, E_{cluster} \tag{4.1}$$

After correcting jets as described above in 4.1, this inclusive factor is not good any more. However, some factor still needs to be applied because R_{686} accounts for several effects in addition to non linearity of calorimeter response. As a function of $E_{cluster}$, we derive the average tracking-corrected energy $< E_{j,tracking}(E_{cluster}) >$. This allows us to restore the correct energy scale by scaling the tracking-corrected energy of each jet :

$$E_j(E_{cluster}) \;=\; \frac{R_{686}\, E_{cluster}}{< E_{j,tracking}(E_{cluster}) >}\, E_{j,tracking}(E_{cluster}) \tag{4.2}$$

4.3 The Improvement in Energy/Momentum Resolution

For these P_t balancing studies we used the CTC reconstructed sample of the 1987 data. The event selection is made with the following cuts :

- $|Z_{vert}| < 60$ cm,
- the detector $|\eta|$ of the two highest E_t jets < 0.8,
- to avoid bias require $P_{t_1} + P_{t_2} >$ trigger threshold.

To show the effect of the tracking correction, we plot σ_ξ as a function of $\sqrt{P}_\xi$, in two cases :

- jet energies as in eq. (4.1),
- jet energies as in eq. (4.2).

The multijet and dijet case are plotted in figures [37] and [38] respectively.

The plots show a clear, systematic decrease of the unbalance after the charged track correction has been applied. This translates to a substantial improvement of the central calorimeter resolution, which is visible both in the dijet and the multijet case.

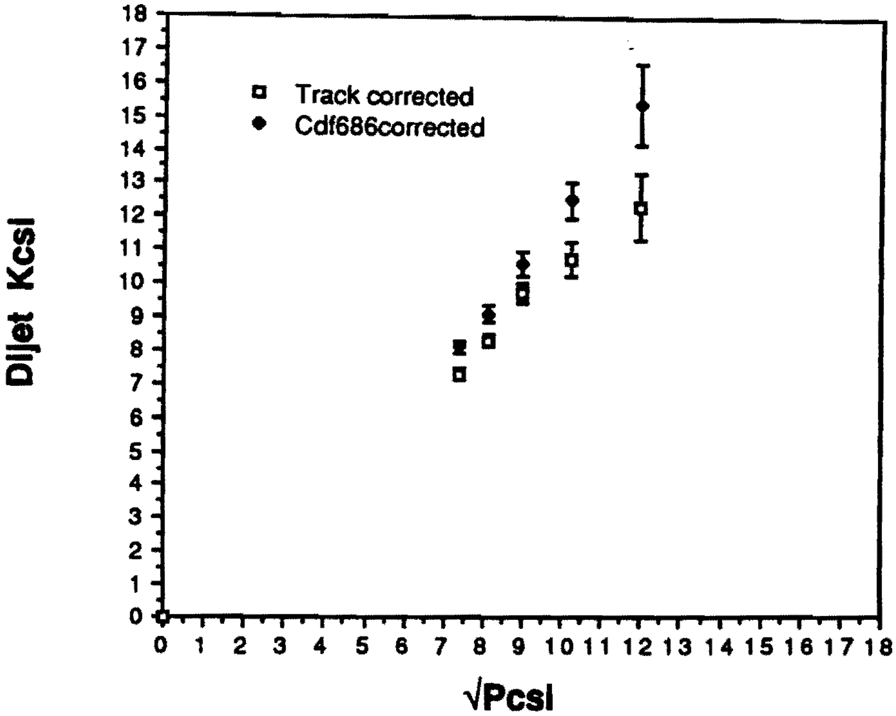

Figure 37: Multijet $K_{t,\xi}$ resolution. σ_ξ versus $\sqrt{P_\xi}$.

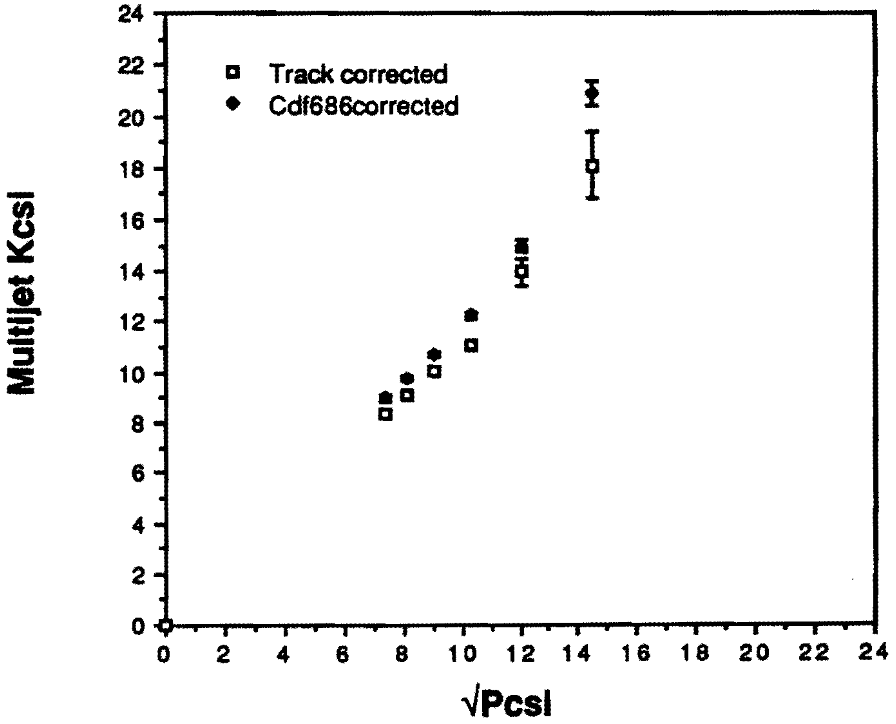

Figure 38: Dijet $K_{t,\xi}$ resolution. σ_ξ versus $\sqrt{P_\xi}$.

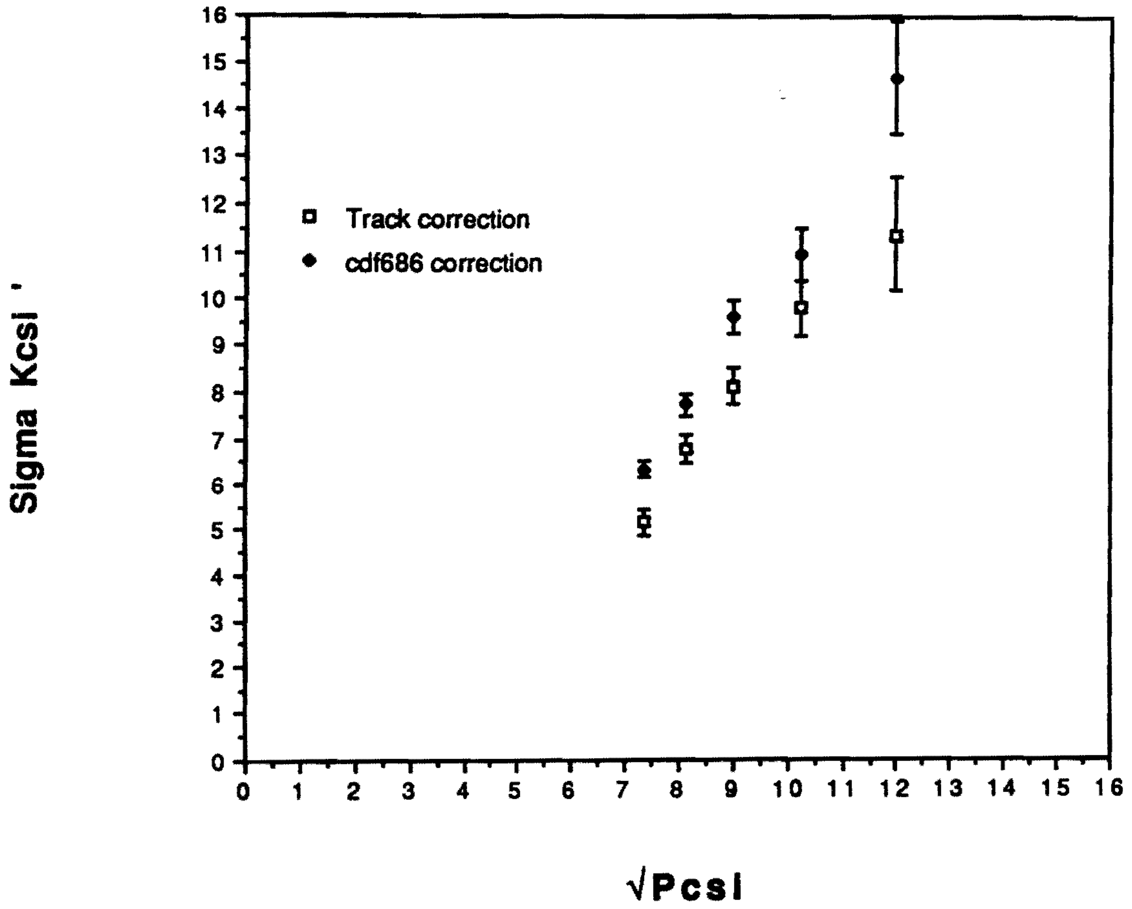

Figure 39: Jet momentum resolution, σ'_ξ versus $\sqrt{P_\xi}$.

The absolute value the resolution as obtained by means of σ_η subtraction is shown in figure [39]. The slopes of the two sets of points are indicative of the resolutions, a steeper dependence corresponding to a worse resolution. However, the two curves do not point to zero and a fit to a straight line going through the origin is not possible. A weighed average of the slopes of straight lines through the single points gives :

$$\alpha_{corr} = 0.83 \pm 0.02, \quad \alpha_{686} = 0.96 \pm 0.02 \quad GeV^{\frac{1}{2}} \tag{4.3}$$

corresponding to an improvement by about 15 % in the resolution.

Table 2 shows the values of Dijet σ_ξ,σ'_ξ and of multijet σ_ξ when the jet energies are corrected as in (4.1) and (4.2).

Table 2: Effect of tracking correction on Dijet and Multijet K_t resolution.

	Tracking correction			CDF-686 correction		
$\sqrt{P_\xi}$	σ_ξ (dijet)	σ_ξ (multi)	σ'_ξ (dijet)	σ_ξ (dijet)	σ_ξ (multi)	σ'_ξ (dijet)
7.4	7.3 ±0.2	8.4±0.1	5.2±0.3	8.1±0.2	9.0±0.1	6.3±0.2
8.1	8.3 ±0.2	9.1±0.1	6.8±0.3	9.1±0.2	9.8±0.1	7.7±0.2
9.0	9.7 ±0.3	10.1±0.1	8.1±0.4	10.6±0.3	10.7±0.1	9.6±0.4
10.25	10.7 ±0.5	11.1±0.2	9.8±0.6	12.5±0.6	12.3±0.2	10.9±0.6
12.0	12.3 ±1.0	14.0±0.5	11.3±1.2	15.4±1.2	15.0±0.5	14.7±1.2
14.5		18.11.3			20.9 1.5	

4.4 Remark about Low Energy Jets

Most of our efforts have been directed to the study of high energy jets ($P > 30$ GeV). In lower energy jets, fluctuations due to finite energy resolution and to external perturbations (underlying event, unreconstructed partons) become comparable, the size of the subtraction $\sigma_\xi - \sigma_\eta$ is large and consequently the method is less sensitive. On the other hand, the charged track correction should be more and more important for jets in the range 5-20 GeV. We expect that the subtraction would have to be different at different η, in order to obtain a real effect on the jet K_t. For these jets, correcting the single towers of the calorimeter as opposed to correcting the cluster energy may be a better strategy. If all towers were separately corrected, one could also look at the variation of the event missing E_t as a way to test the effect.

4.5 Studies of Possible Further Corrections

The major sources of non-uniformity in the central calorimeter are the ϕ-cracks and the 90° θ-crack. In the following paragraphs, the possibility of correcting for these non uniformities is investigated in the two cases separately. The first approach to the problem is to find a criterion to tag the events that are badly measured because of a large flux of energy in the cracks and reject them. The second, more difficult approach is to correct these events in order to save statistics rather then rejecting them.

4.5.1) The ϕ Cracks

The ϕ-cracks are located at angles ϕ =15° N, where N is the address number of the central wedges ($N = 1, 2, ...23$). Test beam studies with electrons and pions have shown that single particles on the cracks generate a lower response with a considerably degraded resolution. The angular width over which the crack is felt is $\pm 1°$ around the nominal position, and the average response is $\simeq 0.70$ of the nominal one. Also jets hitting the towers near their ϕ-edge will suffer from this low response and degraded resolution. In the following three methods to measure the size of this effect are described. The basic idea is to look for correlations between the jet energy flowing in the crack and σ_ξ. The three methods use three different quantities in order to measure the energy flow in the crack.

The azimuthal cracks of the central wedges are not really uninstrumented. Radiator bars (Uranium) with proportional chambers behind, placed in front of the cracks give a rough estimate of the amount of energy flowing in that region. A first attempt of detecting the effect of the ϕ-crack on the jet energy measurement was done by looking at the energy deposition in these crack chambers (CCR). Figure [40] shows σ_ξ as a function of the scalar sum $E_{t,crack}$ of the transverse energies measured in the CCR. As $E_{t,crack}$ increases the undetected and mismeasured energy should also increase and produce an increase of σ_ξ. The plot, however, does not show any correlation between the two variables. This analysis has been repeated changing the sample selection criteria and using the vector instead of the scalar sum of the transverse energies measured in the CCR, but no visible effect has been found. We now attribure this to the excessive noise due to radiation from the Uranium bars in front of the CCR. In the new run of *CDF* (88/89) the Uranium has been replaced with tungsten.

The other two methods were developed by *CDF* collaborators working on the same problem (ref. [3]) The first one uses the reconstructed jet azimuth ϕ_j to select jets that have possibly been mismeasured due to the presence of the crack. It turned out, however, that even ϕ_j is not a useful parameter to monitor the effect of the ϕ-cracks. Because of the spread of particles inside the jet cone, for a given ϕ_j there are large fluctuations of impact points of jet particles flowing around the jet axis and consequently of their energy loss in the crack.

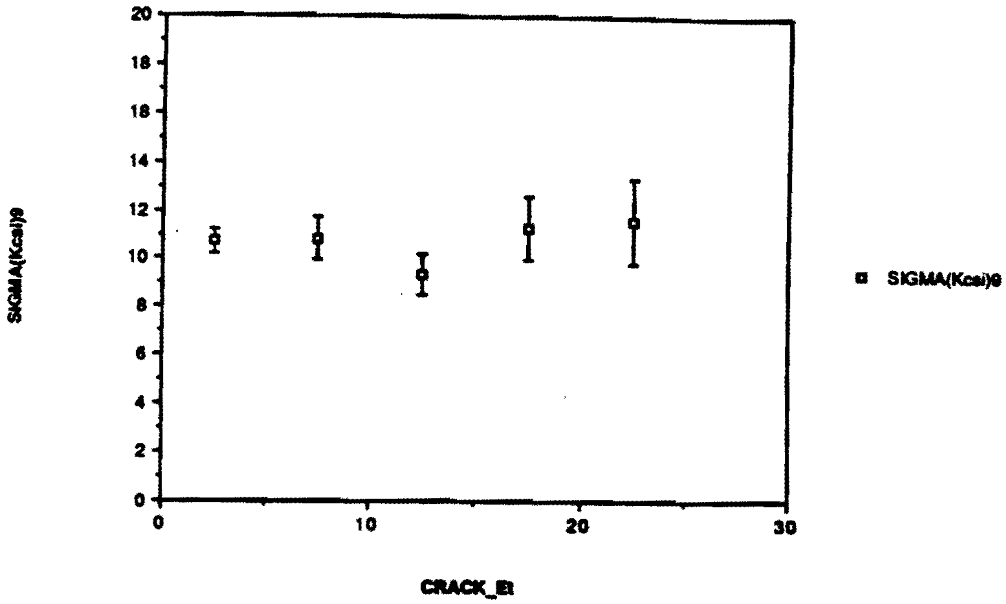

Figure 40: σ_ξ as a function of the E_t measured in the CCR.

The third method uses the single particle information to work out the amount of jet charged energy flowing into the ϕ-cracks. This method can be adopted only after complete tracking reconstruction in the CTC. Each CTC 3-dimensional track extrapolated to the calorimeter is defined as going into a ϕ-crack if the difference between the azimuth of its impact point and that of the crack is less than 1°, $|\phi^{impact} - \phi^{crack} < 1^\circ$.

Tracks must have $P_t > 1$ GeV and their distance from the jet axis must be less than 0.5 in $\eta - \phi$. Low P_t tracks are not included in the sum because due to the magnetic bending they enter the calorimeter wuth a large glancing angle and are not expected to be mismeasured.

For this analisys events were selected in which the two leading jets have pseudorapidity $|\eta| < 1.0$. For each jet the charged energy pointing to the crack, $E_{t,crack}$, is defined as the scalar sum of the transverse momenta of the tracks going into cracks $E_{t,crack} = \sum |P_{t,i}|$. $E_{t,crack}$ shows a direct correlation with K_t : σ_ξ increases with increasing charged energy going into the crack. One finds that in average about 20-25 percent of the energy of the tracks pointing to the ϕ-crack is undetected by the calorimeter. This information can be therefore used for an event by event correction.

Again, this can be done with two purposes: to filter events with mismeasured jets out of the analysis path or to correct the 4-vector of the mismeasured jets and retain them in the sample. To avoid a possible bias in the average correction due to a different sample selection relative to what done in ref. [3], the cut on $|\eta| < 0.8$ that defines the inclusive two jet sample was released to be $|\eta| < 1.0$ as in reference [3], even though a loss in tracking reconstruction efficiency and a less effective correction is expected for tracks belonging to the jets and having $|\eta| > 1.0$.

In a first analysis, events are tossed from the sample if one of the two Et leading jets has an $E_{t,crack}$ greater than some threshold. This threshold is varied from 5 to 15 GeV in 2.5 GeV steps and for each of these values the calorimeter resolution is studied by plotting $sigma_{\xi}$ vs $\sqrt{P_{\xi}}$). The result is that the resolution improves, that is of σ_{ξ} decreases, with increasing energy threshold. The best resolution is attained with the tightest cut, $E_{t,crack} < 5$ GeV. Aa a further check, the charged energy into cracks is computed by "cheating" the correction routine with indicating that the cracks are at the tower centers. Jets that deposit a large energy in these fictitious cracks would now be rejected. However, since in reality these are the best measured jets, throwing them away should now produce an increase of σ_{ξ}. Figure [41] shows σ_{ξ} as a function of $\sqrt{P}_{\xi}$ when no cut is applied to the sample (curve labeled as "uncorrected"), when a cut is applied to the charged energy going into the real crack (curve labeled "5 GeV cut"), and when the same cut is applied to the charged energy going into the fictitious crack (points labeled as "check"). The conclusion is straightforward: by rejecting the events with large energy into the ϕ-cracks the resolution is improved. $E_{t,crack}$ is a useful variable to indicate the mismeasured jets. The price of the 5 GeV cut on $E_{t,crack}$ is a severe loss of statistics. Figure [42] shows the fraction of events of the sample that pass the cut : by requiring $E_{t,crack} < 5$ GeV only 30 percent of the events are left. An attempt of saving statistics is done by correcting the 4-vectors of the jets that fail the cut. The charged 4-momentum pointing to cracks is computed and 25 percent of that it is added to the jet four momentum. The result is shown in figure [43]: no improvement in resolution is obtained with this algorithm. A naturale explanation of this failure is that the 25 percent loss is subject to wild fluctuations that wash out the effect of the correction. For a given flux in a crack, the response can fluctuate very high and very low independent of the average fractional loss. We conclude that the only possible cure of the error introduced. by the phi-cracks is to reject suspicious events. In the analysis of the 1988-89 data, however, this point will be revised by checking wether the crack chambers can now be of some use.

In figure [44] the uncorrected σ_ξ curve is compared with the corrected one for nonlinearity + B-field effects and with the one in which the ϕ-crack filter has been applied in addition. It is clear that the corrections and the cut applied in cascade give an improvement in resolution greater than the one they produce separately. However, in the sample selection that will be used for the measurement of the cross section, the ϕ-crack filter is not applied. One of the main reasons for that is the severe drop in statistics that such a cut produces.

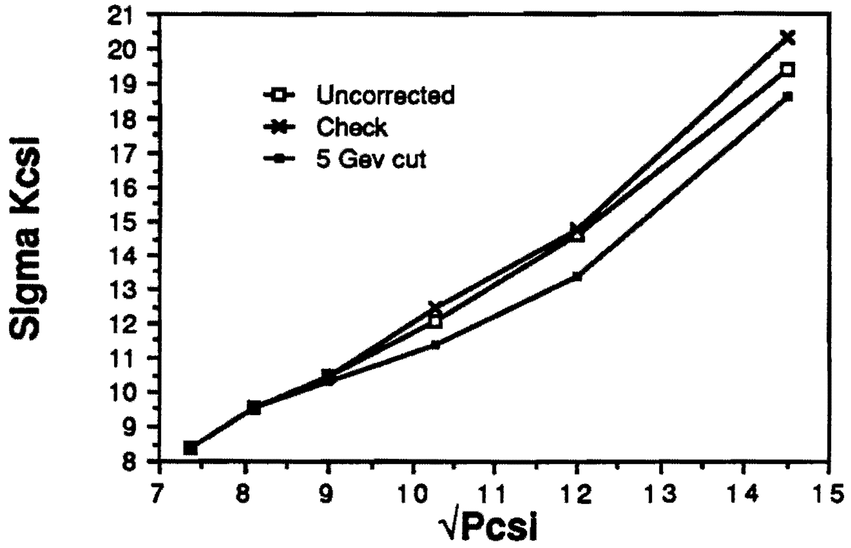

Figure 41: σ_ξ versus $\sqrt{P_\xi}$. Effect of the ϕ-crack filters ("5 GeV cut" and "check") on jet momentum resolution.

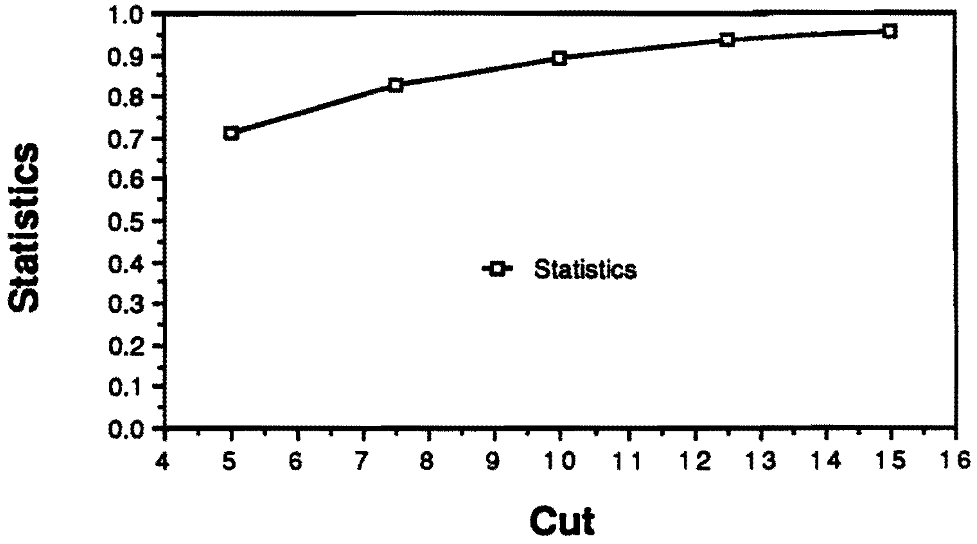

Figure 42: Statistics of the sample as a function of the cut applied on $E_{t,crack}$.

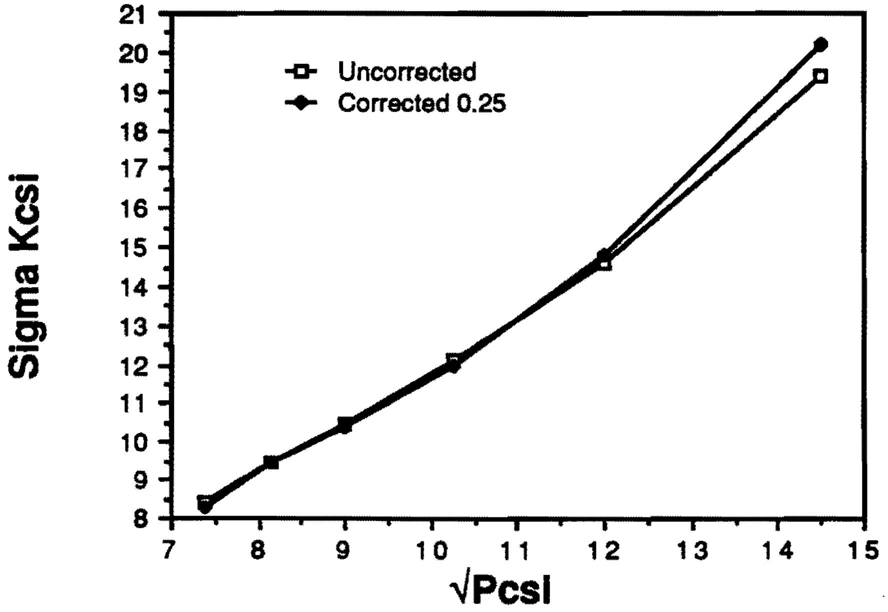

Figure 43: σ_ξ versus $\sqrt{P_\xi}$ with and without the ϕ-crack correction.

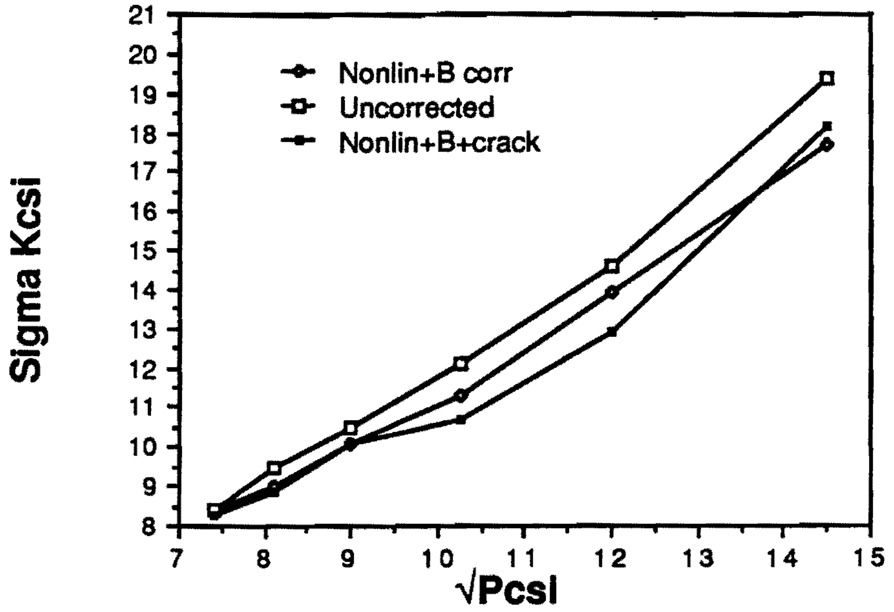

Figure 44: σ_ξ versus $\sqrt{P_\xi}$. Effect of combined tracking corrections and ϕ-crack filter on jet momentum resolution.

4.5.2) The 90° Crack

The 90° crack is the 10 centimeter inactive separation between the two towers n. 0 of the symmetric halves in which the central calorimeter is divided by the plane $z=0$. Differently from the ϕ-cracks, this region is really uninstrumented (no 90° crack chambers) and no test beam study has been done with single particles. The 90° crack is a zone of reduced of calorimeter response to jets. This is seen clearly in the distribution in $\eta_{detector}$ of the first and second leading clusters, that are shown in figures [45] and [46]. For a jet $\eta_{detector}$ is defined as the pseudorapidity associated to the angle between the beams and the direction that from the center of the detector ($z=0$) points to the impact of the jet axis on the calorimeter. $\eta_{detector}$ equals the true η of the jet when the vertex of the interaction sits at the center of the detector. The true η of the jet is the only relevant quantity from a physical point of view, however $\eta_{detector}$ is useful to indicate where in z the jet hits the calorimeter. Jets hitting the 90° crack region have $\eta_{detector} \simeq 0$ and $\theta_{detector} \simeq 90°$.

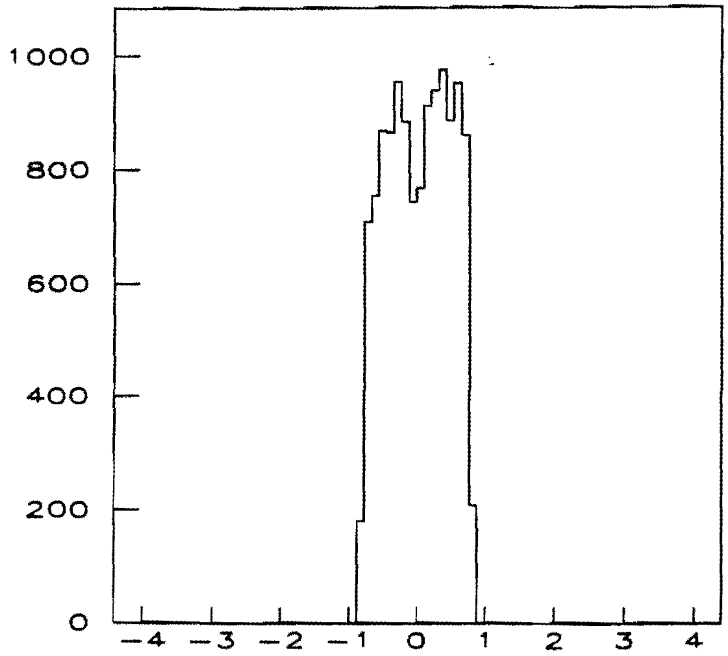

Figure 45: Detector η distribution of leading jet.

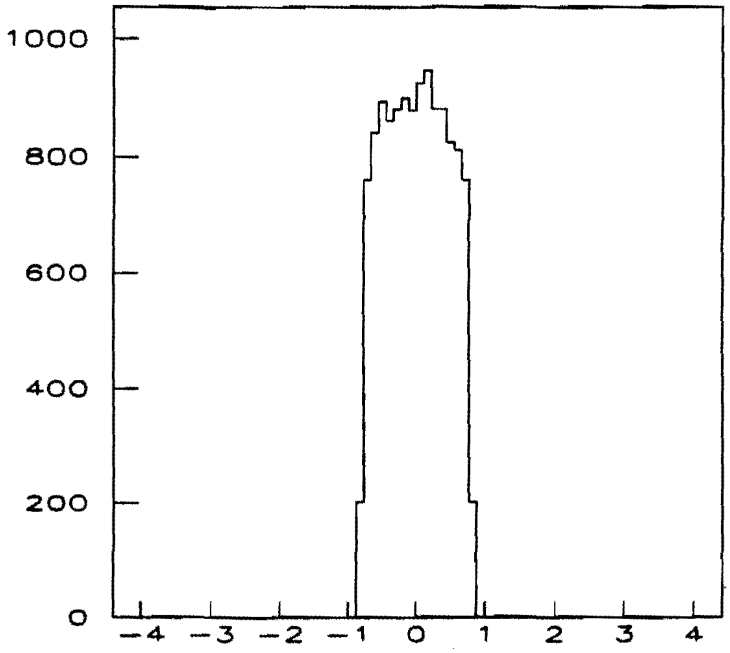

Figure 46: Detector η distribution of second E_t jet.

Figures [45] and [46] show that the leading jet distribution has a dip around $\eta_{detector}= 0$ while the second leading jet does not. When a jet goes into the crack, some of its energy remains undetected and the sum $E_{t_1} + E_{t_2}$ may fluctuate below the 50 GeV trigger threshold. This is particularly true when also the second jet underfluctuates, which must be the case since the jet heading to the crack still appears to be the leading one. This effect creates a dip at $\eta_{detector}$ in the distribution of the jet that appears to be leading one. The distributions in true η behaviour, but the dip is smeared by the vertex shift. Jets hitting the 90° crack of the central calorimeter are bound to have a lower response and a degraded resolution. However, this is expected to be less true when the vertex of the interaction is far from the center of the detector. In this case the angle of incidence of jet particles on the calorimeter is always less than 90°, and the jet prongs are not able to go through the crack without interacting (a similar effect is present in the energy loss of jet particles in the ϕ cracks. There the bending of particle trajectories due to the magnetic field causes the incident angle onto the cracks to be less than 90°, the more so the lower the particle momenta. To allow for this effect we assumed that only tracks with $P_t > 1$ GeV would show a reduced response). As far as the 90° θ-crack is concerned, a possible choice in order to get around the problem is to consider only events whose interaction vertex is close to zero.

Our study of the 90° crack was limited to an attempt to improve the calorimeter resolution by filtering out events where at least one jet was mismeasured. This is done in a way similar to the one used for the $\phi-$cracks. A track is defined as going into the crack if the absolute value of the z coordinate of its impact point is less than 5 cm. Then, like for the ϕ cracks, for each jet, the charged energy pointing to the crack, $E_{t,crack}$ is defined as the scalar sum of of the transverse momenta of the particles going into it. Figure [47] shows $\sigma_{\not{E}}$ vs $\sqrt{P_{\not{t}}}$ before and after the filter. In both these plots the vertex of the interaction is in the interval ±60 cm. The finding is that $\sigma_{\not{E}}$ does not decrease when the "90° crack events" are filtered. The same analysis is repeated with the additional constraint that the event vertex be in the z interval ±5 cm. Figure [48] shows the $\sigma_{\not{E}}$ vs $\sqrt{P_{\not{t}}}$ with and without the filter. Even in this case no improvement is observed.

This negative result is deceaving and totally against expectation. The study will be continued with much more statistics for the 1988-89 run. At present the knowledge of the way the 90°

crack affects the jet measurement is not detailed enough to allow an event by event correction.

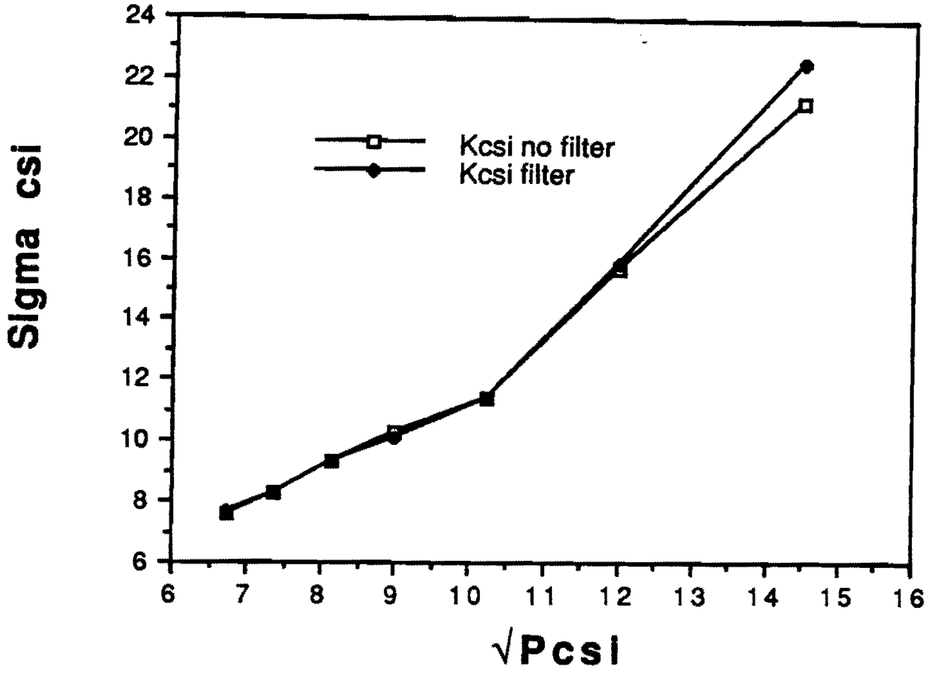

Figure 47: σ_ξ versus P_ξ. Effect of the 90°-crack filter when $|z| <60$ cm.

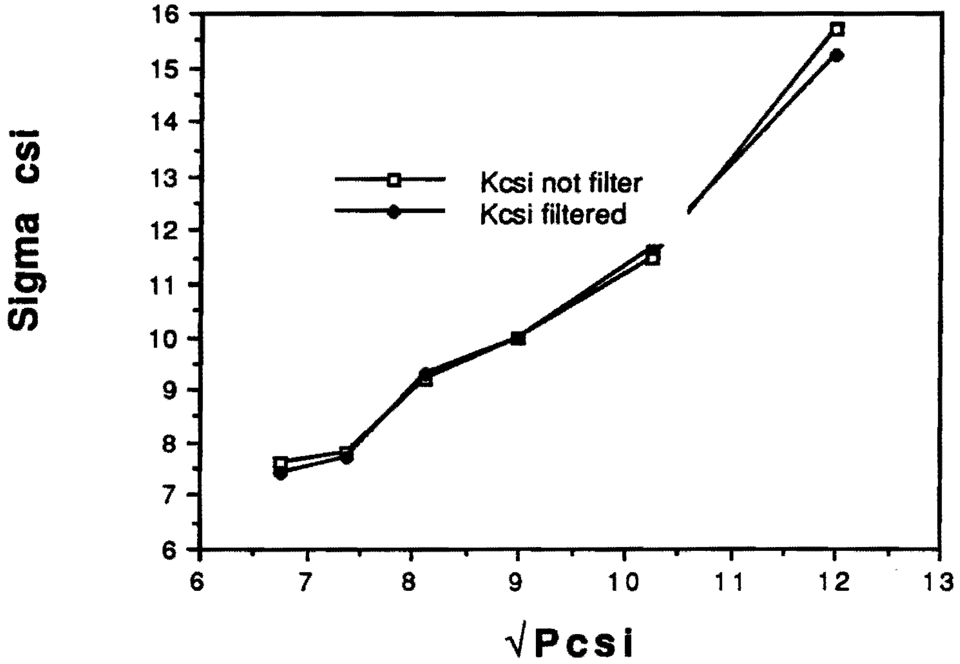

Figure 48: σ_ξ versus P_ξ. Effect of the 90°-crack filter when $|z| <5$ cm.

5 The Cross Section

The selection of the inclusive two jet central sample, the energy/momentum resolution studies and the corrections to jet 4-vectors that was described in Chapters III and IV are intended to prepare the way for the measurement that is described in the next Sections. The experimental constraints of uniform detector and trigger response indicate that the inclusive central sample represents the dataset to use for the cross section. On the other hand, the cuts that define that sample are not physics-oriented, because they allow, for instance, multijet topologies. In the next Section the "third jet problem" is discussed and the physically relevant subsample of events is selected .

5.1 Two versus Three Jets

As explained in the introduction, the original purpose of the work was the measure the differential cross section as a function of the jet pair invariant mass. A stand point in the search was to select two jet events by strongly suppressing the presence of additional clusters, in order to be sensitive to possible decays of massive particles into two-jets. However, we also wanted to perform a measurement that could be compared with QCD. This goal requires a different attitude towards the sample selection. In fact, as shown below, the status of available QCD predictions does not allow to cut on third jet as done in the "bump hunting" approach.

Only a first order calculation of the elementary parton-parton scattering is complete at the present time. The corresponding elementary cross section contains the contributions of all possible two-to-two processes (or Feynmann graphs). A next to leading order calculation is underway but not available yet. The corresponding elementary amplitude would be the interference sum of the two-to-two and two-to-three graphs. The $2 \rightarrow 2$ cross section is only an approximate description of the jets observed at CDF, but is the only one on which it is possible to rely in order to get comparisons with QCD. Out of the inclusive two jet central sample, we should therefore select the events that are most likely to be well described by the $2 \rightarrow 2$ QCD calculation. While waiting for a more complete theoretical prediction, a measure of this cross section is of interest in its own.

Which are the physical observables that can give useful indications on how to filter from the inclusive two jet central sample the events to be compared with 2 → 2 ? Possible filters are the number of reconstructed clusters, the minimum E_t of a possible third cluster and the angle ϕ_{12} formed in the transverse plane between the two leading jets. In order to understand if any of these variables is the answer to the problem, it's mandatory to understand the possible sources that can produce more than two jets in the final state. Additional clusters can come from the hard scattering itself, from spectator parton interactions and from calorimeter noise.

In 2 → 2 QCD, jet production is the convolution of a hard 2 → 2 parton-level scattering with the fragmentation of the initial and final state partons. The evolution of initial- and final-state radiation is governed by the infrared and collinear singularities which dominate the branching process. As a consequence of these singularities most of the emission will be confined within a small angle around the leading hard partons, thus giving rise to typical jet-like configurations. The factorization of the full process into hard 2 → 2 scattering plus branching evolution, however, relies on the assumption that the partons participating in the hard scattering are almost on-shell (as compared to the scale of the hard scattering itself). This is equivalent to saying that the final state jets are almost massless. Sometimes, however, the branching evolution gives rise to the emission of a hard parton (say a gluon) at large angle from the initiator of the shower. When this happens a third jet can develop. If the hard gluon is emitted from the initial state, the third jet will tend to be in the forward region, while if it is emitted from the final state it will tend to be at a large angle with respect to the beam. When a third hard parton is emitted, energy-momentum conservation forces the initiator of the shower to be significantly off-shell and the previous approximation scheme is not appropriate anymore. In particular, for example, since we are dealing with large angle emission, diagrams in which the radiated gluon is emitted from different partons may have significant interference, and it is not possible anymore to claim unambiguously (even within a given approximation) from which parton the gluon is coming from. Thus the calculation of the exact 2 → 3 hard process becomes necessary for a precise determination of the invariant mass spectrum. This calculation is very complex, because for it to be fully consistent at the O(α^3) in P_t, the virtual corrections to the 2 → 2 process must be calculated as well. This is necessary for a smooth matching of the 2 → 3 differential cross section with the 2 → 2 one when the third parton becomes either soft or collinear to one of the others. Unfortunately this full calculation is not available yet, and we can only use the 2 → 2 prediction, which we will try to verify by constraining the presence of a third jet in our sample. The experimental definition of 'jet' as a cluster of energy contained within a given cone will account for the evolution of the final state partons via soft and collinear radiation, consistently with the factorization into a hard 2 → 2 scattering followed by fragmentation.

Another physical source of third jets is the fragmentation of the "spectator" partons that are not involved in the hard scattering. The fragments of the colliding hadrons undergo an interaction which can be tentatively described as a minimum-bias process. As a result we would obtain a distribution of particles which is similar to the minimum bias. Studies of particle correlations in hard events are not very detailed yet and results are qualitatively consistent with this picture. The single particle rapidity distribution is approximately flat (out to about 4 units of rapidity), which implies that most of the energy will escape in the very forward direction. The particles from this so-called *underlying event* are uniformly distributed around the beam, and even though they carry a substancial amount of energy (in fact, all of the energy that is left from the hard process), their p_t spectrum is very soft and they usually do not contribute to the jet spectrum. However, it does happen occasionally that components of the tail of the p_t spectrum or fluctuations in the rapidity density distribution will give rise to clusters of transverse energy that will be reconstructed as a jet by the algorithm. These jets are completely unrelated to the hard process, and it would be incorrect to include them into the computation of the jet mass. Since it is impossible to distinguish these jets from the jets due to initial state bremsstrahlung on an event-by-event basis, we will just have to exclude them all in order to perform a consistent comparison with the results of perturbative QCD. This is a small possible bias that cannot be avoided.

In dealing with "two versus three jet" issues an important physical parameter to consider is, as mentioned above, the angle ϕ_{12}, formed in the transverse plane between the momenta of the two leading jets. If the perturbation due to higher order processes or hard fragmentation of the spectator partons is negligible then the two final states partons are expected to be produced with transverse momenta that are back to back. Strictly speaking, for this to be true, the system of the initial colliding partons must have net zero transverse momentum, which is true with good approximation. One could think of selecting from the data 2 → 2 topologies by requiring the two E_t leading jets of the event to be back-to-back in the transverse plane within some "tolerance" interval. Jet counting and any third jet cut have already turned out to be intrinsically partially inefficient to isolate a clean two jet sample. Of course, this intrinsic inefficiency will still remain in a ϕ_{12} cut so that it becomes a matter of taste which variable to use to apply the selection and where to put the cut. However, the back-to-backness is a very basic property of two particle collisions and a cut based on it is, maybe, a more physically clean way of selecting two jet events than merely counting them. The ϕ_{12} cut looks pretty related with the third jet cut. In fact, suppressing additional clusters with E_t above some threshold is not much different from filtering from the sample events in which ϕ_{12} scatters from 180° by more than the chosen tolerance interval.

The back-to-backness is chosen, as the leading feature of $2 \rightarrow 2$ processes and prominent three jet events are filtered from the sample by setting the tolerance interval equal to $\pm 20°$. Since jet azimuth is measured with a finite resolution of a few degrees, a much tighter cut would cause a loss of events and not affect the physics. Figure [49] shows the distribution of ϕ_{12} for all the events of the inclusive central sample. A 20° cut keeps a high fraction of the total number of events. Adopting the ϕ_{12} cut means to make a semi-inclusive measurement of the differential cross section as a function of the jet pair invariant mass. This choice allows a reasonable comparison with the QCD leading order calculation and, at the same time, meets the experimental wish of performing a measurement that is not totally driven by the only existing theoretical prediction.

Consistently with this, the invariant mass is always defined using the 4-vectors of the two Et leading jets. Figure [50] shows the two-jet mass distribution. One may wonder whether, when a third jet at not-too-large angles is found in the event, a more sensible choice would be to compute the three-jet invariant mass as opposed to the two-jet one. We checked the changes induced by this option by applying the following algorithm: if an event that passes the ϕ_{12} cut has a third jet that is distant from the two leaing ones by less than a fixed amount R_{cut} in the $\eta - \phi$ space, then we compute the three jet mass, otherwise the ordinary jet pair mass. In this way we hope to eliminate the effect of jets which are for example due to hard initial state radiation or fluctuations of the underlying event. Three different values of R_{cut} were chosen: 1.2, 1.5 and 2. The resulting mass distributions are shown in figures [51],[52] and [53].

As we see the effects are observable but within the uncertainties associated with the leading order 2 → 2 calculation, and uncertainties coming from possible different choices of structure functions or of the Q^2 scale for the running coupling constant. These uncertainties are directly tied to the ignorance about effects of the next order in perturbation theory. Indeed the fact that our cross-section changes with the value of R_{cut} is an effect which could in principle be described by a full next-to-leading order perturbative calculation.

Once it has been decided how to deal the third jet issue, suitable kinematic variables for describing the jet pair has to be found. The center of mass of the pair is naturally adoped. In this system the two jets are produced back to back in the 3-dimensional space, while in the laboratory this is true only in the transverse plane. Moreover, in the approximation of massless jets the two cms energies are equal, which means that the rapidities of the two jets are equal in magnitude and opposite in sign. Since the initial state is rotation-invariant around z, the angular information is all contained in Y^*, the cms pair rapidity, which is related to the jet pseudorapidities in the laboratory as :

$$Y^* = \frac{\eta_1 - \eta_2}{2}. \tag{5.1}$$

The description of the jet pair in their center of mass is completed once their invariant mass is specified. Another variable is, finally, needed to take into account the motion of the dijet in the laboratory. This is given by the Lorentz boost rapidity Y_b :

$$Y_b = \frac{\eta_1 + \eta_2}{2}. \tag{5.2}$$

In each event, all the kinematical properties of the massless jet pair can be expressed in term of (M_{jj}, Y^*, Y_b). An alternative description in terms of (M_{jj}, η_1, η_2) is not as convenient and natural as the previous one.

To measure the differential cross section for the production of central jet pairs as a function of the pair invariant mass, one should integrate over some chosen intervals of Y^* and Y_b. An appropriate region of the phase space must be selected. All the mass interval that is available to CDF trigger will be used. The selection of the inclusive two jet central sample does not remove the trigger bias, because no cut is made on the sum $E_t(1) + E_t(2)$ in order to make sure that the thresholds of the different $\sum E_t$ triggers with which the data have been collected are all passed. At this stage of the analysis a possible bias in M_{jj} is removed by filtering the events that are on the onset of the M_{jj} distribution. As far as the angular variables are concerned, the region of uniform detector and trigger acceptance is determined by the cuts :

$$|\eta_1| \leq 0.8, \qquad |\eta_2| \leq 0.8 \tag{5.3}$$

A cut on η_1, η_2 is driven by unavoidable experimental constraints. The $2 \rightarrow 2$ elementary scattering is naturally decomposed into the flux of initial partons and the cms configuration expressing the dinamics of the process. The motion of the system is described by Y_b, and the interaction by the distributions in M_{jj} and Y^*. The pseudorapidities of the jets in the lab are used to select well-measured jets. However, the final sample is selected in term of Y^* and Y_b by requiring :

$$|Y^*| \leq 0.4, \qquad |Y_b| \leq 0.4. \tag{5.4}$$

In this way, we are measuring the differential cross section as a function of the invariant mass of jet pairs produced at very large angles in the cms ([68°, 112°]) ; the boost of the system of the two jets is required to be small as compared to the range of possible values, which means that the pair is produced by the scattering of primary partons whose momenta before the collision were approximately balanced.

The integrated cross section is divided by the area of the integration domain, $(0.8)^2$, in order to get a cross section that is differential in M_{jj} and averaged in Y^* and Y_b :

$$\frac{1}{0.8\ 0.8} \int_{-0.4}^{0.4} \int_{-0.4}^{0.4} \frac{\mathrm{d}\sigma}{\mathrm{d}M_{jj}\mathrm{d}Y^*\mathrm{d}Y_b} \mathrm{d}Y^*\mathrm{d}Y_b \tag{5.5}$$

This averaged cross section is an estimate of the quantity :

$$\left. \frac{\mathrm{d}\sigma}{\mathrm{d}M_{jj}\mathrm{d}Y^*\mathrm{d}Y_b} \right|_{Y_b=Y^*=0} \tag{5.6}$$

How well our average approximates the $Y^* = 0$ and $Y_b = 0$ can be tested by checking wether the averaged cross section depends on the width of the integration domain. This is not practical within the 1987 statistics. With the higher statistics than it is expected in the 1988-89 run a better estimate would be obtained by narrowing Y^* and Y_b limits.

Since the jet 4-vectors have been corrected to correspond to the final state partons, M_{jj} is the invariant mass of the elementary process. However, two corrections still need to be done before comparing with QCD. A correction must be applied for the effect of the finite resolution in M_{jj}. Secondly, a correction has to be made for the inefficiencies of the analysis cuts. This is described in the following paragraphs.

5.2 Resolution Smearing

The finite mass resolution of the measurement, convoluted with the steeply falling M_{jj} spectrum, produces a shift of the entries of the distribution that would be measured by a perfect calorimeter towards higher masses. Depending on the natural slope and on the resolution the effect ("*resolution smearing*") may produce an important change in the shape of the curve.

The M_{jj} resolution can be obtained by propagating the momentum measurement errors determined by means of the P_t-balancing method. In the approximation of massless jets the jet pair invariant mass can be written as :

$$M_{jj} = (P_{t_1} + P_{t_1})\cosh Y^* \tag{5.7}$$

where Y^* is the c.m.s. rapidity of the pair. Its variance, neglecting angular errors, can be expressed as :

$$\sigma^2_{M_{jj}} = \cosh^2 Y^*(\sigma_{P^2_{t_1}} + \sigma_{P^2_{t_2}}) \tag{5.8}$$

Since, as it is derived in Chapter III, $\sigma_P = 0.83\sqrt{P}$, we have :

$$\sigma_{P_t} = 0.83\sqrt{P_t \sin\theta} \tag{5.9}$$

$$\sigma^2_{M_{jj}} = 0.83\cosh^2 Y^*(P_{t_1}\sin\theta_1 + P_{t_2}\sin\theta_2). \tag{5.10}$$

Averaging over polar angle in the region [50°,130°] (or on Y^* over the interval [-0.4,0.4]) would not cause a large effect and would only slightly decrease the error relative to the $\theta = 90°$ case. Therefore

$$\sigma_{M_{jj}} \leq 0.83\sqrt{M}_{jj} \tag{5.11}$$

that is, the invariant mass resolution is of the order of the single jet momentum resolution. Since the momentum error has an approximate gaussian distribution, also the probability M_{jj} is expected to be gaussian.

The smeared experimental curve f_{sm} can be written as the convolution of the primary distribution f_{unsm} with the error distribution that we shall indicate with $g(t)$:

$$f_{sm}(M_{jj}) \;=\; \int_{-\infty}^{+\infty} f_{unsm}(M_{jj}+t)\, g(t)\, \mathrm{d}t \tag{5.12}$$

In order to compute the integral, since the first derivative of f_{unsm} is a slowly varying function of t, f_{unsm} can be expanded in series neglecting the terms that contain the third and higher order derivatives :

$$f_{sm}(M_{jj}) \;=\; \int_{-\infty}^{+\infty} [\, f_{unsm}(M_{jj}+t)g(t) + t f'_{unsm}(M_{jj}+t)g(t) + \frac{t^2}{2} f"_{unsm}(M_{jj}+t)g(t)\,]\mathrm{d}t \tag{5.13}$$

Since $g(t)$ is gaussian, then the integral of $tg(t)$ is zero. Therefore :

$$f_{sm}(M_{jj}) \;\simeq\; f_{unsm}(M_{jj}) + \frac{f"_{unsm}(M_{jj})}{2} \int_{-\infty}^{+\infty} t^2\, g(t)\mathrm{d}t \tag{5.14}$$

The integral that is left is, by definition, the variance of $g(t)$, that is $\sigma^2_{M_{jj}}$. The final result is :

$$f_{sm}(M_{jj}) \;=\; f_{unsm}(M_{jj}) + \frac{f"_{unsm}(M_{jj})}{2}(0.83\sqrt{M}_{jj})^2 \;=\; f_{unsm}(M_{jj}) + f"_{unsm}(M_{jj})\, 0.34\, M_{jj}. \tag{5.15}$$

We checked that this is a good approximation by applying it to the analitical function chosen by the UA2 collaboration (ref [8]) to fit their M_{jj} data :

$$f_{unsm}(M_{jj}) \;=\; (\frac{M_{jj}}{c})^{\gamma} e^{\alpha M_{jj}} \tag{5.16}$$

where c is a normalization constant and α and γ are the parameters of the fit. The fit values are $\alpha = -7.25\ 10^{-3}$, $\gamma = -4.18$ for the theoretical curve and $\alpha = -13.9\ 10^{-3} \pm 3\ 10^{-3}$, $\gamma = -3.46 \pm 0.27$ for the data. The fit to the experimental curve has a $\chi^2 = 36$ for $\nu = 38$ degrees of freedom. The analitycal expression of the second derivative is :

$$f"_{sm}(M_{jj}) \;=\; f_{unsm}(M_{jj})[\frac{\gamma(\gamma-1)}{M^2_{jj}} + 2\frac{\alpha\gamma}{M_{jj}} + \alpha^2]. \tag{5.17}$$

Given the fit values of γ and α the fourth order derivative is completely negligible over [50,350], the considered range of M_{jj}.

Using the UA2-like functional fit of the data, the relation between the unsmeared and the smeared distribution can be expressed as :

$$f_{sm}(M_{jj}) \; = \; f_{unsm}(M_{jj})\Big[1 + 0.34\, M_{jj} \, (\frac{\gamma(\gamma-1)}{M_{jj}^2} + 2\frac{\alpha\gamma}{M_{jj}})\Big] \; = \; f_{unsm}(M_{jj})\Big[\,0.34\,\frac{\gamma(\gamma-1)}{M_{jj}} + 0.69\alpha\gamma)\Big]. \tag{5.18}$$

The smearing effects is corrected for by dividing the value of each bin of the experimental distribution by the factor

$$1 \, + \, 0.34\,\frac{\gamma(\gamma-1)}{M_{jj}} \, + \, 0.69\alpha\gamma. \tag{5.19}$$

The "*smearing correction*" to the cross section as computed with the above analytical method turned out to be rather modest. We attribute this in part to the improved resolution in M_{jj} that is obtained by means of the tracking corrections that have been applied. Further work is in progress to generate an expected experimental distribution from the QCD prediction and the detector simulation.

5.3 A comment on Acceptance

Events whose vertex is well off-center ($>$ 60 cm) are not used in the analysis because they present potential problems. The central tracking chamber efficiency is in average reduced in these events, jets are entering the calorimetry at unusual angles, etc. The efficiency of this cut is calculated on a run by run basis and the integrated luminosity is properly corrected for. This is done using the Z-vertex distribution of the minimum bias runs and looking at the fraction of events that are rejected by the cut. This fraction represents the efficiency of the cut.

We already showed that in the adopted Y^* , Y_b region the detector acceptance is complete. At $M_{jj} >$ 50 GeV, when the trigger efficiency is 100 %, the measaured cross-section after the unfolding of resolution smearing can therefore be readily compared with 2 → 2 QCD.

5.4 Present Data in Comparison with QCD

Once the acceptance and smearing corrections have been applied to the experimental distribution (eq. (5.5)) can be compared with QCD. Figure [54] shows this comaparison. The proton structure functions used are EHLQI, with Λ =200 MeV. The band of uncertainty of the theoretical prediction comes from a different choice of the Q^2 scale : $Q^2 = (\frac{P_t}{2})^2$ for the upper curve, $Q^2 = P_t^2$ for the central curve and $Q^2 = (2P_t)^2$ for the lower curve. Figure [55] shows the variation of the predicted cross section as a function of the choice of the structure functions : DO1 (Λ =200 MeV, line), DO1 (Λ =400 MeV, dashed line), EHLQI (Λ =200 MeV, dash and dotted line), Gluck et al (Λ =400 MeV, dotted line).

In Figure [54], most of the experimental curve is bracketed by the band of theoretical prediction. Given the theoretical uncertainties related to the Q^2 scale, to the choice of Λ and to the choice of the nucleon structure functions, we conclude that the measured cross section is in good agreement with the QCD leading order calculation. This is even mre true if one considers that there is a normalization uncertainty of ±35% in our jet data (ref [10]). This comes about mostly because of the luminosity uncertainty (±15%) and because of the reflection on the cross-section scale of the uncertainty of the absolute energy scale. In view of this, the agreement between data and theory can be considered as satisfactory. However, there is an apparent lower slope in the data with respect to theory. This is under study, in particular with reference to the smearing correction. On the other hand, inclusion of a third jet distant by less than 1.5 in η-ϕ increases the slope, as seen in fig. [56].

5.5 Conclusions

We have carried through a complete analysis of central jet pair data, leading to a satisfactory agreement with $2 \rightarrow 2$ QCD predictions up to $M_{jj} \simeq$350 GeV. The method employed, including tracking corrections and jet quality cuts to improve the mass resolution , shall be soon applied to the much more abundant 1988-1989 data and allow a study of the cross-section up to much larger momentum transfers. With luck, new phenomena (e.g. quark compositness) might be unravelled.

References

[1] S. Kuhlmann *et al*, CDF Note # 686 (Central Jet Energy/Momentum Corrections)

[2] S. Behrends *et al*, CDF Note # 583 (Response of the Central Calorimeter to Low Energy Charged Particles)

[3] M. Dell'Orso, P. Gianetti, G. Punzi, CDF Note # 896 (The Central Calorimeter ϕ Cracks and the Jet Energy Measurement)

[4] Eichten *et al*, Rev. Mod. Phys. 56, 579,(1984); and errata Fermilab-Pub-86/75-T(1986)

[5] S.D.Drell and T.M.Yan, Phys. Rev. Lett, 25 316 (1970)

[6] D. Brown *et al*, CDF note # 605 (Clustering algorithms and their performance)

[7] J.D.Bjorken, Phys. Rev. 163, 1767 (1967)

[8] R.Ansari *et al* Phys. Lett. B, 186 452 (1987)

[9] S. Dell'Agnello *et al*, CDF Note in preparation (Charged Track Corrections to Jet Energy/Momentum) (↳ # 1015)

[10] F. Abe *et al* Phys. Rev. Lett. 62(1989)613 (Measurement of the inclusive Jet Cross Section in $p\bar{p}$ Collisions at $\sqrt{s}$ =1.8 TeV)

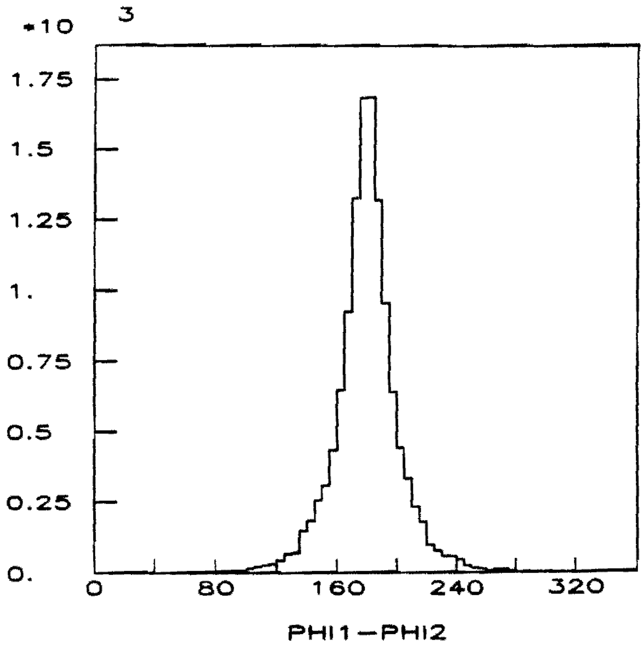

Figure 49: Distribution of ϕ_{12}.

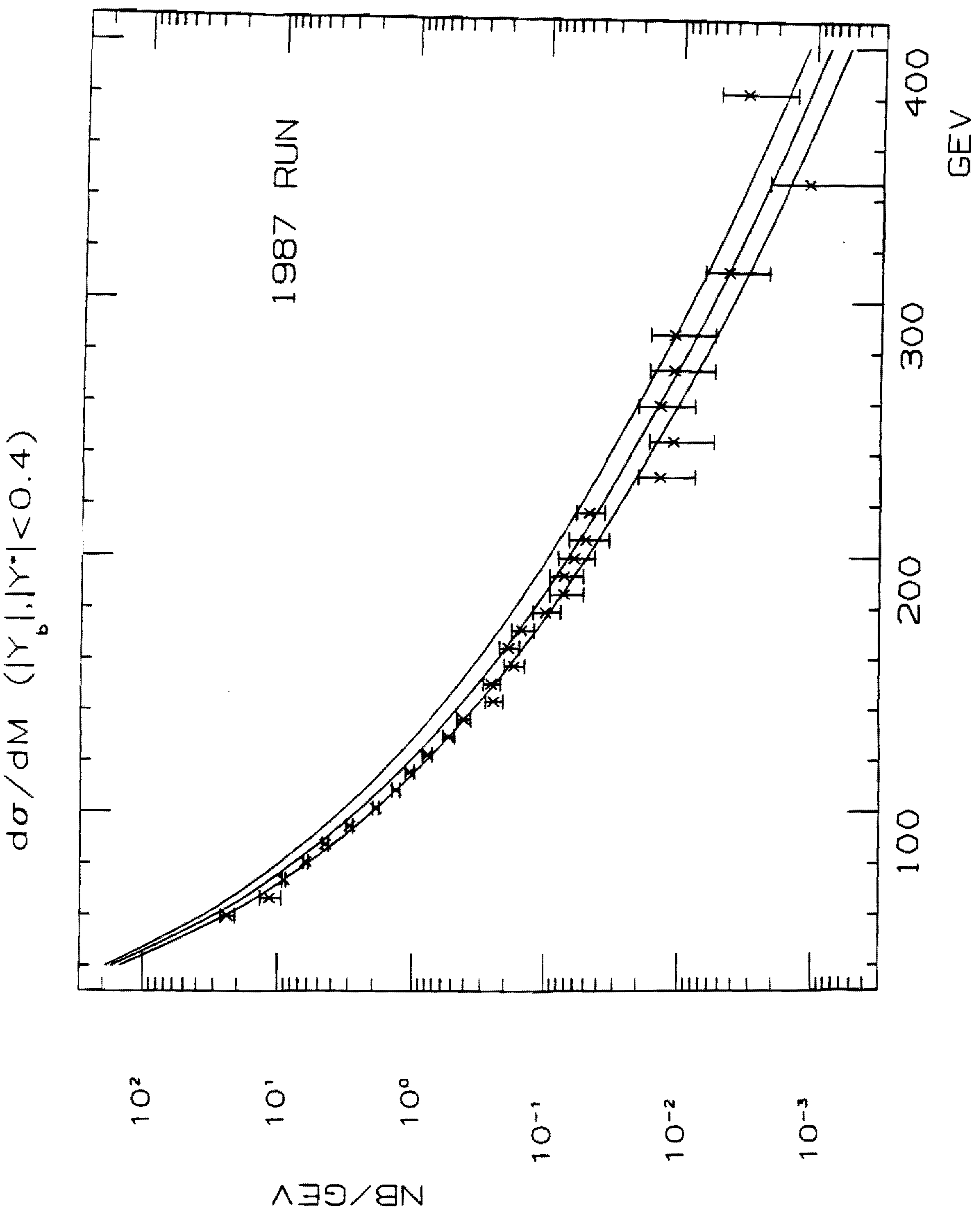

Figure 50: Two-jet distribution uncorrected for smearing and acceptance. $|Y^*|$ and $|Y_b| < 0.4$.

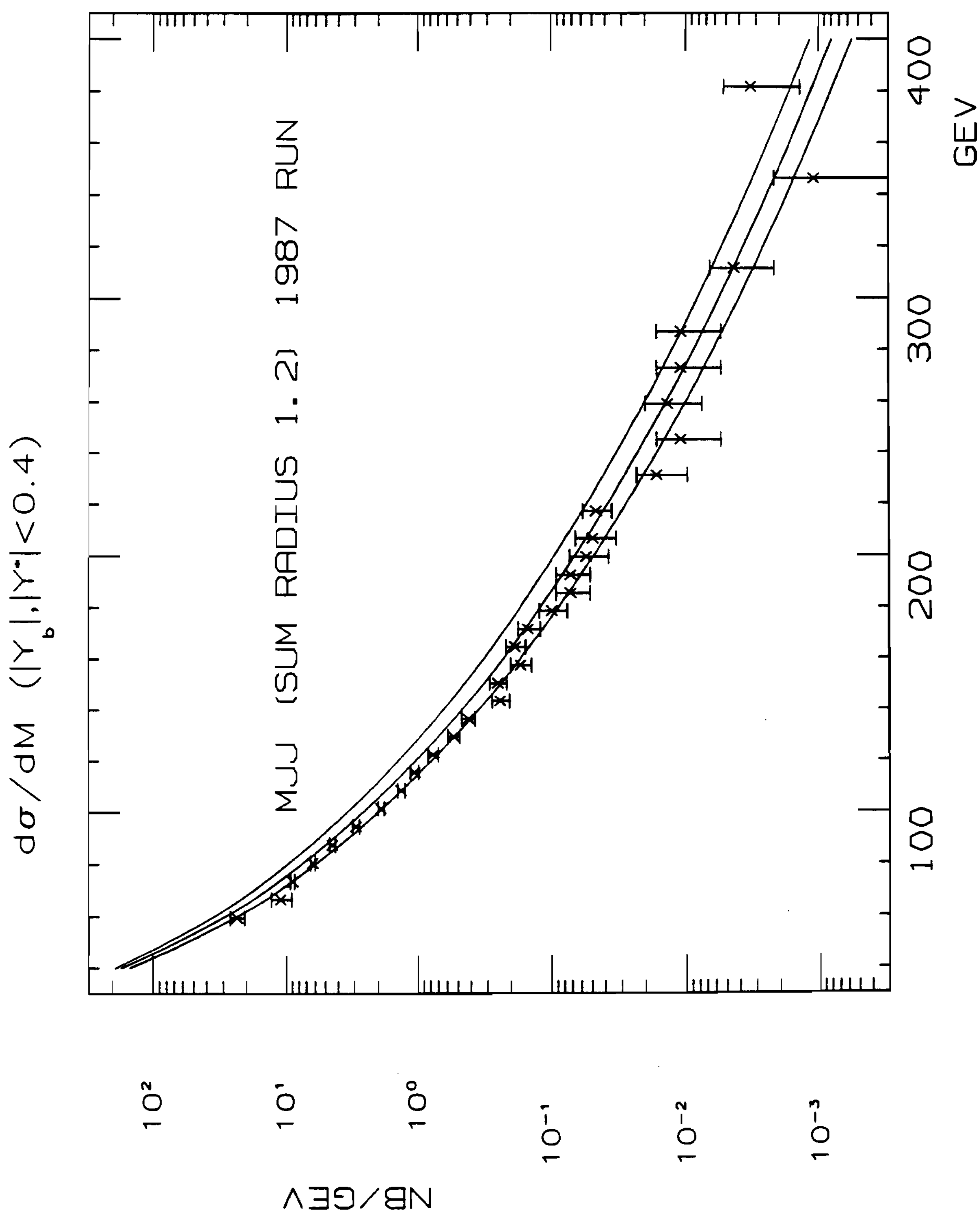

Figure 51: Two jet distribution.R_{cut} =1.2 . $|Y^{*}|$ and $|Y_b| < 0.4$.

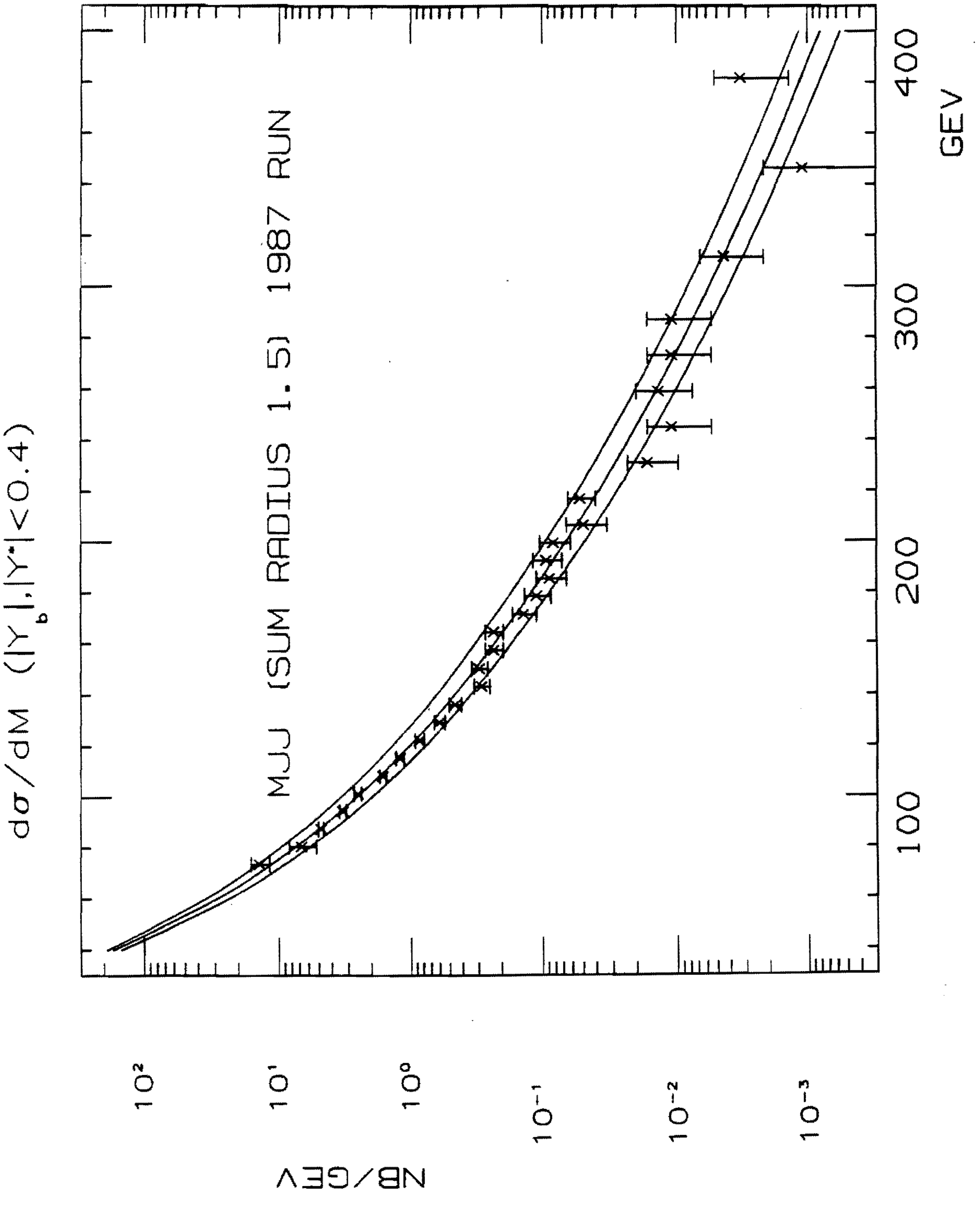

Figure 52: Two jet distribution.R_{cut} =1.5 . $|Y^*|$ and $|Y_b| < 0.4$.

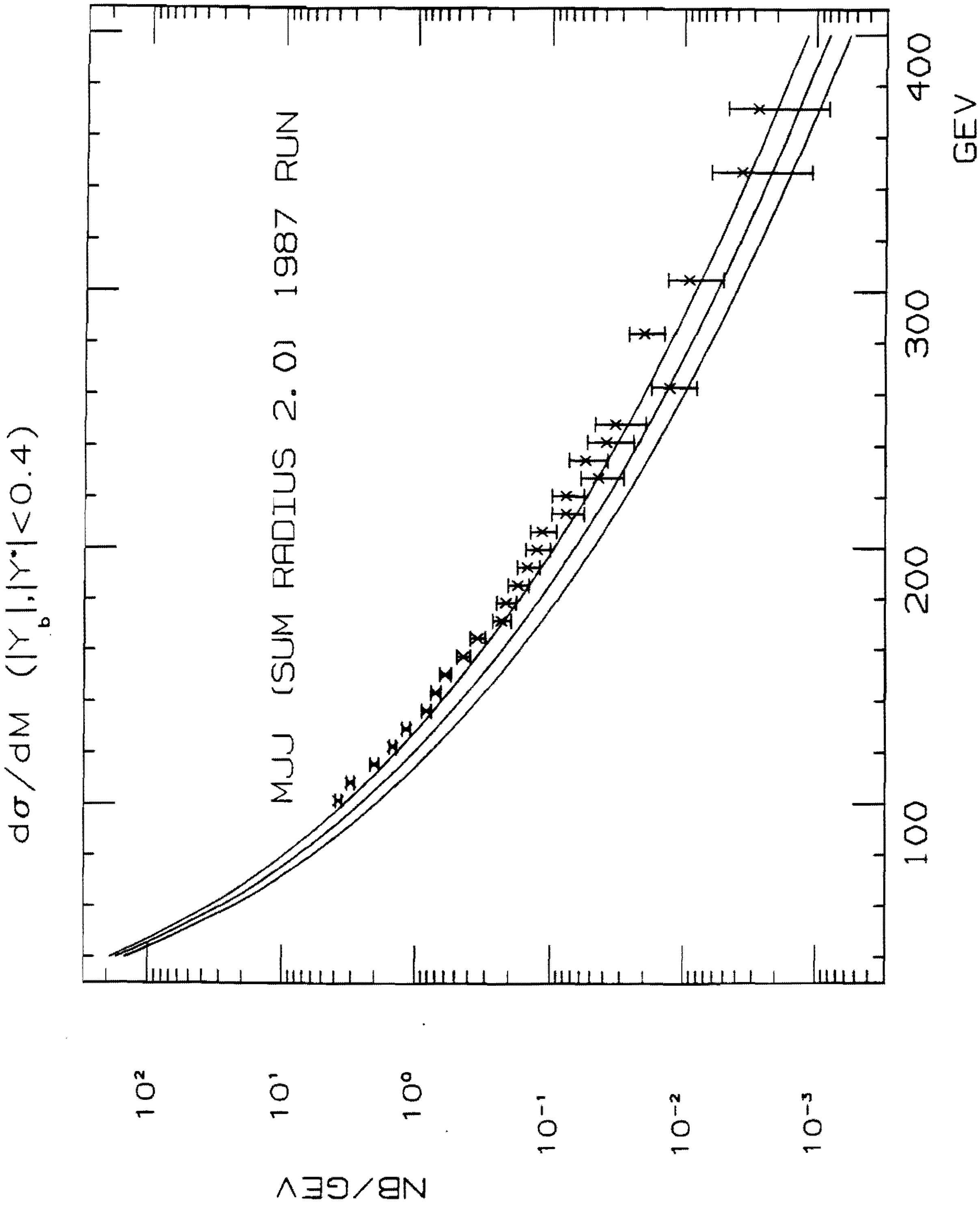

Figure 53: Two jet distribution.R_{cut} =2.0 . $|Y^*|$ and $|Y_b| < 0.4$.

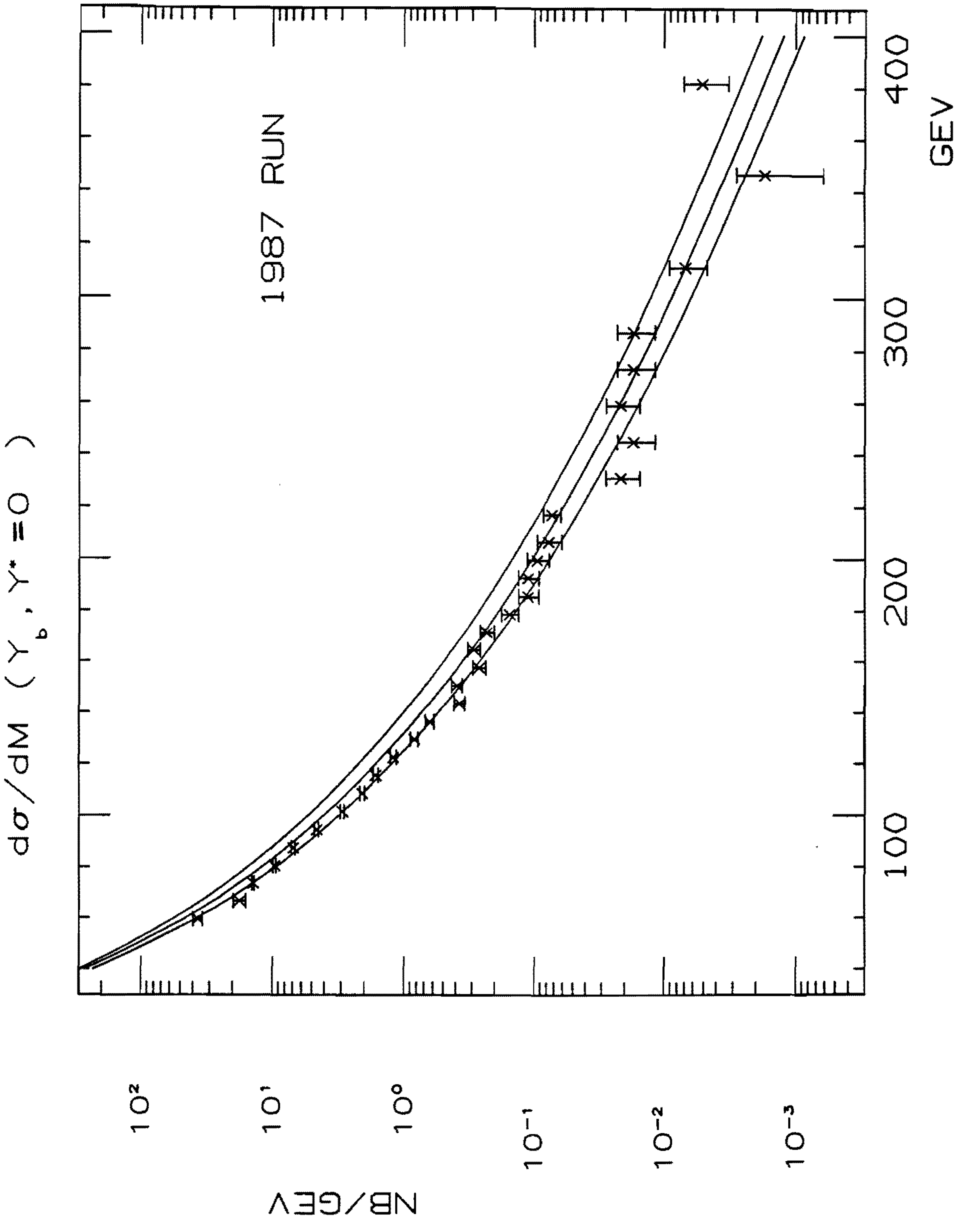

Figure 54: Two-jet cross section (corrected for resolution smearing and acceptance) in $|Y^*| = |Y_b| = 0$.

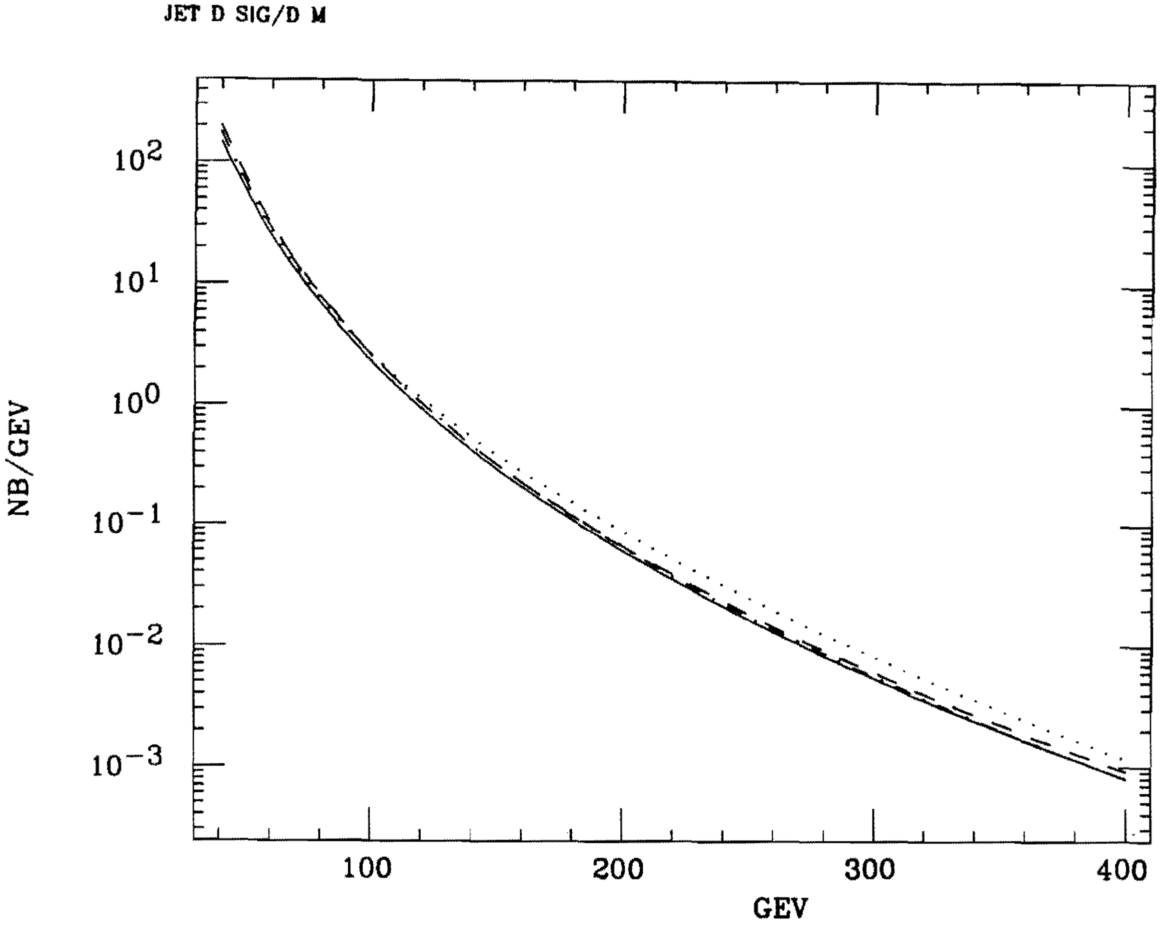

Figure 55: Predicted two-jet cross section for different choices of structure functions .

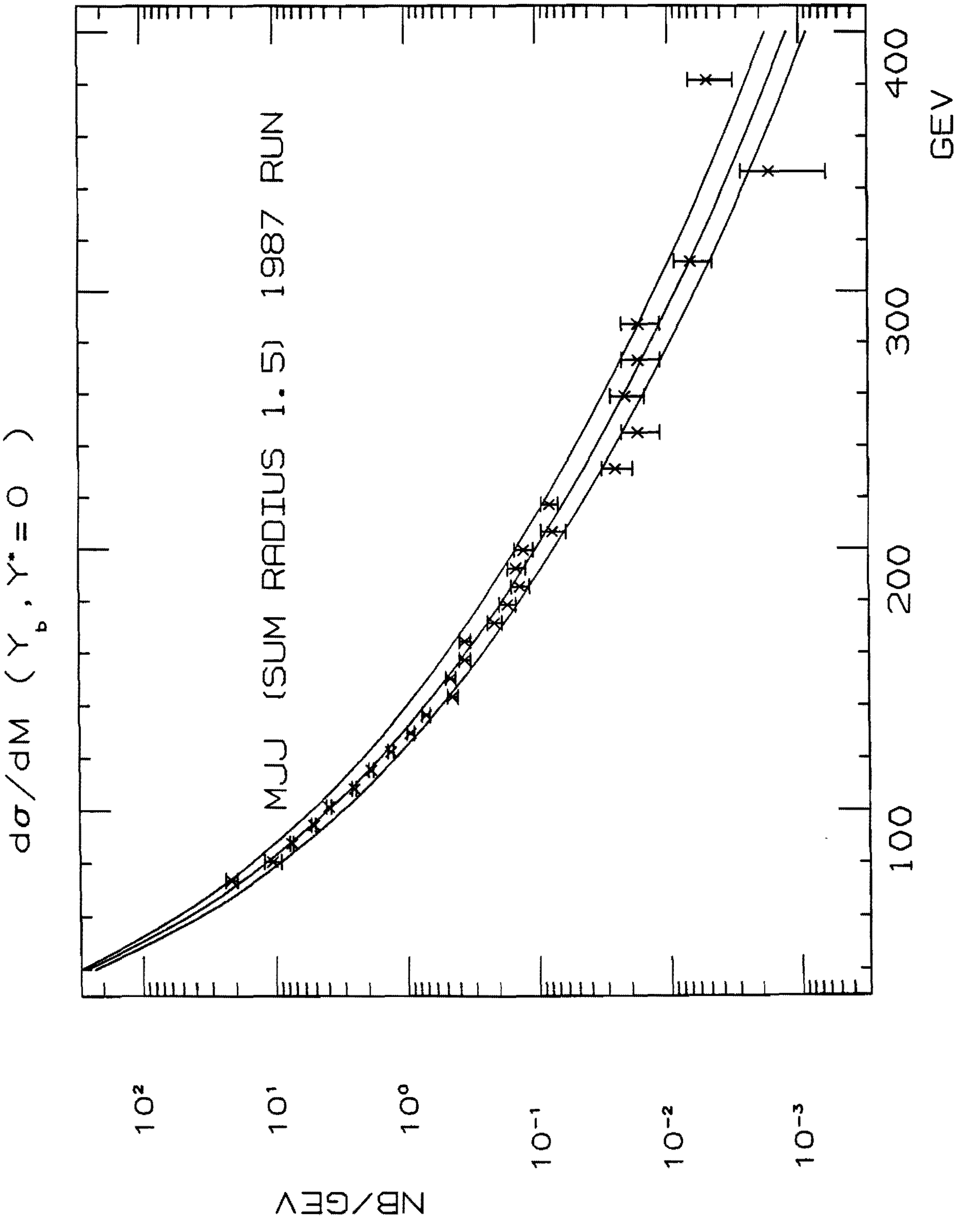

Figure 56: Two jet cross section (corrected for resolution smearing and acceptance) in $|Y^*| = |Y_b| = 0$. $R_{cut} = 1.5$.